Measurement of the $\Lambda_b^0 \to \Lambda_c^+ \pi^-$ Branching Ratio

Yi Le

A dissertation submitted to the Johns Hopkins University in conformity with the requirements for the degree of Doctor of Philosophy.

Baltimore, Maryland
2003

Copyright © 2003 by Yi Le,
All rights reserved.

Abstract

We present a measurement of the $\Lambda_b^0 \to \Lambda_c^+ \pi^-$ branching ratio in $p\bar{p}$ collisions at $\sqrt{s}$ = 1.96 TeV using 65 pb^{-1} data collected by the Collider Detector at FermiLab (CDF). The measurement starts from reconstructing two decay modes:

$$\Lambda_b^0 \to \Lambda_c^+ \pi^-, \text{ where } \Lambda_c^+ \to p \ K^- \ \pi^+$$

$$\bar{B}^0 \to D^+ \pi^-, \text{ where } D^+ \to \pi^+ \ K^- \ \pi^+.$$

We obtained 96 $\pm$ 13 Λ_b^0 and 321 $\pm$ 22 $\bar{B}^0$ candidates from the CDF Run II Two-Track Hadronic Trigger data sample. The relative branching ratio of the two decays is then measured based on the equation:

$$\frac{f_{\Lambda_b}}{f_d} \frac{BR(\Lambda_b \to \Lambda_c^+ \pi^-)}{BR(\bar{B}^0 \to D^+ \pi^-)} = \frac{BR(D^+ \to K\pi\pi)}{BR(\Lambda_c^+ \to pK\pi)} \frac{N_{\Lambda_b}}{N_{\bar{B}^0}} \frac{\epsilon_{\bar{B}^0}}{\epsilon_{\Lambda_b}}.$$

The measurement gives

$$\frac{f_{\Lambda_b}}{f_d} \frac{BR(\Lambda_b \to \Lambda_c^+ \pi^-)}{BR(\bar{B}^0 \to D^+ \pi^-)} = 0.66 \pm 0.11 \text{ (stat)} \pm 0.09 \text{ (syst)} \pm 0.18 \text{ (BR)}.$$

The $\Lambda_b^0 \to \Lambda_c^+ \pi^-$ branching ratio is then extracted, giving

$$BR(\Lambda_b^0 \to \Lambda_c^+ \pi^-) = \{6.6 \pm 1.2 \text{ (stat.)} \pm 0.9 \text{ (syst.)} \pm 2.3 \text{ (BR+FR)}\} \times 10^{-3}.$$

The Λ_b^0 sample we reconstructed in this analysis is the largest fully reconstructed Λ_b^0 sample in existence. The result we report here on the $\Lambda_b^0 \to \Lambda_c^+ \pi^-$ branching ratio is the world's first such measurement.

Acknowledgements

First and foremost, I owe the greatest debt of gratitude to my adviser and mentor, Prof. Bruce Barnett. Without you there would not have been this thesis. When I was brought to see you on the first day I came to Hopkins, I didn't know it was the beginning of five and a half years of great experiences working with you. Thanks for sending me to FermiLab in my first summer at Hopkins. In that summer I got a chance to learn about the exciting CDF experiment and decided to do my Ph.D thesis at CDF. Thanks for guiding me through both the oral qualify exam and the Graduate Board Oral exam. These two hard exams became so easy after preparing with you. Thanks for helping me to choose this analysis and always being there in the whole process of this analysis. Thanks for all the scientific insight and direction and all the advice on things outside the scientific world. You are the best adviser I could have ever asked for.

I would like to thank Prof. Petar Maksimović for his great contributions to this analysis. Without his enormous help on every detail of this analysis, this thesis would not have come out so quickly and nicely. I owe a great debt to his wife and son for those holidays, weekends and off hours that he spent on this thesis. I certainly will miss those over-nights before "blessing" that we worked through together.

I would like to thank all the other faculty members at Johns Hopkins. It was my privilege to have a chance to study under so many great professors. Special thanks go to Prof. Barry Blumenfeld, Prof. C.Y. Chien and Prof. Morris Swartz.

Many thanks to the postdoctoral fellows of the Hopkins CDF group. Matthew Martin helped a lot in this analysis, especially on the background studies. Matthew Herndon was always the one I went to when I had coding and silicon related questions. Satyajit Behari had a lot useful discussions with me. I thank you all.

It was a great pleasure to work with the other Hopkins graduate students at CDF. I specially thank Kai Yi for his great help on this analysis. Thanks for many useful discussions and suggestions all the way through this analysis. He showed me the spirit of hard work that a graduate student needed to accomplish the most. I also want to thank him for the fun I had with him and his family when we were not talking

about physics. I would like to thank Robert Napora, not only for his input on physics but also for being my roommate for one year and teaching me many things about American society. I thank Reid Mumford for all the discussions and help in the CDF control room. I also want to thank former Hopkins graduate student Chadd Smith for sharing some great experiences with me. I would like to thank all my classmates and friends during my first two years at Johns Hopkins before I moved to FermiLab. A big thanks goes to Chi Xiong, who came to Johns Hopkins the same year as me and went through many things together with me. His great help made my life much easier back then.

This thesis was made possible by the efforts of all members of the CDF collaboration and all the FermiLab staff, who spent endless hours on designing, building, operating and maintaining both the CDF detector and the FermiLab Accelerators. In particular, I thank the B physics group conveners, Marjorie Shapiro and Christopher Paus, for their great leadership and support for this analysis. I thank the B hadronic group conveners, Stefano Giagu, Marco Rescigno and Rolf Oldeman, for providing a nice place to work on interesting physics. Your continuous guidance made this analysis possible. I also thank Jeff Tseng for sharing his Run I experience with me. Thanks to Donatella Lucchesi and I. K. Furić for cross checking some of the results. Thanks to Alex Cerri, Andreas Korn and many others for valuable discussions.

At FermiLab, I would like to thank all my Chinese friends from CDF, D0 and other divisions. I can't put everyone's name here because there are so many of you. You guys made FermiLab a fun place to live and study at the same time. I certainly will miss these three and half years of my life at FermiLab.

I would also like to thank Prof. Cheng Li, Prof. Hongfang Chen and Prof. Zizong Xu at the University of Science and Technology of China (USTC). They led me into the particle physics world.

Last, but certainly not least, I would like to thank my family for their many years of love, support and encouragement. I love you all.

Contents

List of Figures viii

List of Tables xii

1 Introduction 1
- 1.1 Brief History . . . 1
- 1.2 High Energy Physics . . . 3
- 1.3 Outline of the Thesis . . . 5

2 Theory 6
- 2.1 The Standard Model . . . 6
  - 2.1.1 Particles, Interactions and Gauge Symmetries . . . 6
  - 2.1.2 Quantum Chromodynamics (QCD) . . . 8
  - 2.1.3 Electroweak Theory . . . 10
  - 2.1.4 Beyond Standard Model . . . 12
- 2.2 The Bottom Quark . . . 13
  - 2.2.1 b quark Production at $p\bar{p}$ Colliders . . . 15
  - 2.2.2 b quark Fragmentation . . . 16
- 2.3 Heavy Quark Effective Theory(HQET) . . . 19
  - 2.3.1 Heavy Quark Symmetry . . . 19
  - 2.3.2 HQET . . . 21
- 2.4 Λ_b baryon and its decay rate . . . 21

3 Experimental Apparatus 26
- 3.1 The Accelerators . . . 26
- 3.2 Collider Detector at Fermilab (CDF) . . . 35
  - 3.2.1 Detector Overview . . . 35
  - 3.2.2 Tracking Systems . . . 35
    - 3.2.2.1 Inner Tracker: L00 + SVX II + ISL . . . 36
    - 3.2.2.2 Central Outer Tracker: COT . . . 44
  - 3.2.3 Calorimeter Systems . . . 45
  - 3.2.4 Muon Systems . . . 47

3.2.5 Trigger systems . . . 49

4 Data Sample and Event Selection **57**
4.1 Hadronic Data Sample . . . 57
4.1.1 The Trigger Paths . . . 58
4.1.2 Trigger Path Selection . . . 62
4.1.3 Good Runs Selection . . . 62
4.2 Monte Carlo Data Sample . . . 64
4.2.1 B Generator . . . 64
4.2.2 Decay Packages: EvtGen and QQ . . . 65
4.2.3 Trigger and Detector Simulation . . . 65
4.3 Offline Track Reconstruction and Refitting . . . 67
4.3.1 Offline Track Reconstruction . . . 67
4.3.2 Track Refitting . . . 68
4.4 Event PreSelection . . . 69
4.4.1 Track Quality Cuts . . . 69
4.4.2 Trigger Confirmation . . . 69
4.5 Event Reconstruction . . . 70

5 Physics Analysis **73**
5.1 Analysis Overview . . . 73
5.2 Event Reconstruction . . . 74
5.2.1 Cut Selection and Optimization . . . 74
5.2.2 B^0 reconstruction . . . 75
5.2.3 Λ_b^0 reconstruction . . . 78
5.3 Background Study . . . 82
5.3.1 Background from "Four prong" B meson decay . . . 82
5.3.2 Background from all other B meson decays . . . 83
5.3.3 Background from all other Λ_b decays . . . 84
5.3.4 Reflection from $\Lambda_b^0 \to \Lambda_c^+ K^-$ decays . . . 85
5.3.5 Combinatorial Background . . . 86
5.4 Fitting for the $\Lambda_b^0 \to \Lambda_c^+ \pi^-$ yield . . . 89
5.4.1 Components of the Λ_b^0 mass fit . . . 89
5.4.2 Constraints in the Λ_b^0 mass fit . . . 90
5.4.3 The Fit Result . . . 91
5.4.4 Studies of the fit quality using the Toy Monte Carlo approach 93
5.4.5 The Λ_b fit Studies . . . 99
5.5 Determination of the efficiency ratio $\epsilon_{\bar{B}^0}/\epsilon_{\Lambda_b}$ . . . 106

6 Systematic Uncertainty **110**
6.1 Uncertainties From Monte Carlo . . . 110
6.1.1 Uncertainties due to Λ_b and $\bar{B}^0$ lifetimes . . . 111

6.1.2 Dalitz structure of Λ_c . . . 111
6.1.3 Polarization of Λ_b^0, Λ_c^+ . . . 113
6.1.4 XFT configuration . . . 116
6.1.5 ϕ efficiency . . . 116
6.1.6 p_T spectrum of $\bar{B}^0$ . . . 116
6.2 Uncertainties From Fit Models . . . 119
6.3 Uncertainties From Errors in Branching Ratios $D^+ \to K^-\pi^+\pi^+$ and $\Lambda_c^+ \to p^-K^+\pi^-$ . . . 119
6.4 Summary . . . 119

7 Results and Conclusions **121**
7.1 Experimental Result . . . 121
7.2 Discussion and Conclusion . . . 122

A The cut optimization **124**

B The effect of the Λ_b^0 selection cuts **129**

C The constraints in the Λ_b fit **133**
C.1 Constraint on the number of the four-prong reflections . . . 133
C.2 Constraint on $N_{\rm ref}/N_{\rm otherB}$ . . . 133
C.3 Constraint on $N_{\rm other\Lambda_b}/N_{\rm Bmesons}$ . . . 135

Bibliography **137**

List of Figures

2.1 Leading order $b\bar{b}$ production Feynman diagrams in $p\bar{p}$ environments . 15
2.2 Some examples of Next-to-leading order $b\bar{b}$ production Feynman diagrams in $p\bar{p}$ environments 16
2.3 The b quark production cross section at CDF 17
2.4 The b quark fragmentation process, the left is cluster model, the right is string model. (The figure is from reference [15]) 18
2.5 Lower order Λ_b^0 decay diagrams, all three channels are via b $\rightarrow$c transition. 23

3.1 An aerial view of FermiLab Accelerator chain. 27
3.2 A diagram of FermiLab Accelerator chain. 31
3.3 The Tevatron's integrated Luminosity from the beginning of Run II to Sept. 2003. The luminosity is plotted weekly. The vertical blue bar shows the weekly total luminosity in nb^{-1}. The diamond connected line displays the total integrated luminosity in pb^{-1}. 33
3.4 The Tevatron's peak Luminosity. The blue triangle shows the peak luminosity at beginning of each store. The red diamond displays the average of the last 20 peak values. 34
3.5 An elevation view of CDF II detector. 36
3.6 A Longitudinal View of the CDF II Tracking System. 37
3.7 Both r-ϕ view and r-z view of the silicon tracking systems. Note in the r-z view, the z direction is compressed. 38
3.8 An end view of L00 and the inner sensors and outer sensors of L00. . 39
3.9 Three barrels of SVXII. 40
3.10 Schematic of the SVX II data acquisition system. 43
3.11 A section of the COT end-plate. The radius of each layer and number of cells in each layers are shown. The slots for the sense plane and field plane are also shown. 45
3.12 A $r-\phi$ view of three super cells in the COT. 46
3.13 A 3-D View of the CDF II detector with the muon chambers and their coverage in pseudorapidity indicated. 48

3.14 The CDF II readout functional block diagram. 54
3.15 The block diagram of CDF II data flow 55
3.16 Architecture and data flow of the SVT trigger. 56

4.1 The decay diagrams of $\Lambda_b^0 \to Lambda_c^+\pi^-$ and $\bar{B}^0 \to D^+\pi^-$ 71

5.1 Invariant mass distribution of $\bar{B}^0 \to D^+\pi^-$ candidates. The histogram is fit with two Gaussians on top of a second order polynomial background. 76
5.2 Invariant mass distribution of $\bar{B}^0 \to D^+\pi^-$ candidates with an alternative fit. The histogram is fit with two Gaussians on top of a broad Gaussian background. 77
5.3 Invariant mass distribution of $\bar{B}^0 \to D^+\pi^-$ candidates. The histogram is fit with two Gaussians on top of an Exponential background shape. 79
5.4 Invariant mass distribution of $\Lambda_c^+ \to p^+k^-\pi^+$ candidates, which are reconstructed as a part of the Λ_b candidates. 80
5.5 Invariant mass distribution for $\Lambda_b^0 \to \Lambda_c^+\pi^-$ candidates. The distribution is fitted with a sum of a single Gaussian and a linear background. 80
5.6 The correlation between the invariant masses of the Λ_b and a Λ_c. . . 81
5.7 Λ_b^0 invariant mass distribution. 83
5.8 The shape of the four-prong reflection sample reconstructed using the Λ_b^0 hypothesis, obtained from the realistic Monte Carlo simulation. . 84
5.9 A fit to the invariant mass distribution of all other non-four-prong B-meson decays. 85
5.10 A fit to the invariant mass distribution of all other non-four-prong B-meson decays, focusing on the behavior of the function near the Λ_b^0 peak. 86
5.11 A fit to the invariant mass distribution of all other Λ_b^0 decays. Other baryons species are ignored. 87
5.12 A fit to the invariant mass distribution of all other Λ_b^0 decays, focusing on the behavior of the function near the Λ_b^0 peak. 87
5.13 A fit to the invariant mass distribution of $\Lambda_b^0 \to \Lambda_c^+K^-$ decays when reconstructed as $\Lambda_b^0 \to \Lambda_c^+\pi^-$. 88
5.14 The "baseline" Λ_b mass fit. 92
5.15 The "baseline" Λ_b mass fit, but zoomed into the region just around the Λ_b peak, demonstrating a fairly good agreement between the data points and the fit result. 92
5.16 The distribution of negative log likelihood for 500 Monte Carlo "experiments." 95
5.17 The distributions of two fit parameters of interest, the number of Λ_b signal events, N_{Λ_b}, and the number of four-prong reflections, $N_{\rm ref}$. The values used to generate them were 96 and 88, respectively. 96

5.18 The pulls of the two parameters of interest: the number of Λ_b signal events N_{Λ_b}, the number of four-prong reflections $N_{\rm ref}$. 97
5.19 The pulls of the four parameters of interest: the number of events in the "other Λ_b" component $N_{\rm other\Lambda_b}$ and the mass of Λ_b. 98
5.20 The baseline fit, but without the constraint on $N_{\rm other\Lambda_b}/(N_{\rm ref}+N_{\rm otherB})$ ("C_3"). In this fit, the "other Λ_b" component (the black dashed line) can float freely. 99
5.21 The baseline fit, but *only* with the constraint on $N_{\rm ref}/N_{\rm otherB}$ ("C_2"). The "other Λ_b" component is unconstrained, and the only constraint on the four-prong reflection component comes from C_2. 100
5.22 The baseline fit, but *only* with the constraint on $N_{\rm ref}$ ("C_1"). 101
5.23 The baseline fit, but *without any* constraints. 101
5.24 The study of the effect of a sharper cut-off of the "other B" and "other Λ_b" components. The tails of these two components (given in green and black) are made shorter. 102
5.25 The study of the effect of a more smeared cut-off of the "other B" and "other Λ_b" components. The tails of these two components (given in green and black) are made longer. 103
5.26 The baseline fit, but with the width of Λ_b fixed to 20 MeV/c^2, one sigma away from the central value of 23 ± 3 MeV/c^2. 103
5.27 The baseline fit, but with the width of Λ_b fixed to 26 MeV/c^2, one sigma away from the central value of 23 ± 3 MeV/c^2. 104
5.28 The baseline fit but *without* the $\Lambda_b \to \Lambda_c K$ component. 104

6.1 Dalitz plot from data without sideband subtraction. 113
6.2 Λ_b decay angle definition for production polarization 114
6.3 Λ_c polarization in term of emission angle of proton 115
6.4 The system for testing Λ_b polarization 115
6.5 The ϕ_0 distribution of one pion candidate track. The pion here is the one from Λ_b^0 117
6.6 A comparison of p_T of the $\bar{B}^0$ candidates in the data and the realistic Monte Carlo. The red solid histogram is MC and green points are data. 118
6.7 Efficiency ratio *vs.* p_T of B^0. 118

A.1 Significance as a function of d_0 of Λ_b. Blue dots mark the significance and green triangles the reconstruction efficiency. 125
A.2 Significance as a function of p_T of Λ_b. Blue dots mark the significance and green triangles the reconstruction efficiency. 125
A.3 Significance as a function of p_T of Λ_c. Blue dots mark the significance and green triangles the reconstruction efficiency. 126
A.4 Significance as a function of p_T of the pion from Λ_b. Blue dots mark the significance and green triangles the reconstruction efficiency. . . 126

A.5 Significance as a function of p_T of the proton. Blue dots mark the significance and green triangles the reconstruction efficiency. 127
A.6 Significance as a function of $c\tau$ of the Λ_b candidate. Blue dots mark the significance and green triangles the reconstruction efficiency. . . 127
A.7 Significance as a function of $c\tau$ of the Λ_c candidate measured from the Λ_b vertex. Blue dots mark the significance and green triangles the reconstruction efficiency. 128

B.1 p_T of the proton in the realistic Monte Carlo simulation. The cut is at $p_T = 2.0$ GeV/c 129
B.2 A distribution of the p_T of the pion from Λ_b decay in the realistic Monte Carlo simulation. The cut is at $p_T = 2.0$ GeV/c. 130
B.3 Distribution of $c\tau$ for the Λ_b^0 in the realistic Monte Carlo simulation. The cut is at $c\tau = 0.0225$ cm. 130
B.4 The impact parameter d_0 for the Λ_b^0. The cut is at $|d_0| = 0.0085$ cm. 131
B.5 The p_T of Λ_b^0. The cut is at $p_T = 7.5$ GeV/c. 131
B.6 The $c\tau$ of the Λ_c^+ measured from the Λ_b^0 vertex. The cut is at $c\tau =$ -0.0065 cm. 132
B.7 The p_T of Λ_c^+. The cut is at $p_T = 4.5$ GeV/c. 132

C.1 $\bar{B}^0$ reflections explicitly reconstructed in Λ_b^0 's mass window. The result of this fit (40 ± 12 events) provides a normalization for the shape for all the four-prong reflections obtained from the Monte Carlo simulation (shown in Fig. 5.8). 134

List of Tables

2.1 Masses and Charges of Quarks and Leptons(The charge is in units of the absolute electron charge.) 7
2.2 Masses and Charges of Gauge Bosons (The charge is in units of the absolute electron charge.) 8
2.3 Predictions for $\Lambda_b \to \Lambda_c \pi^-$ branching ratio from reference [34] 24
2.4 Predictions for $\Lambda_b \to \Lambda_c \pi^-$ branching ratio from reference [35] 25

3.1 Current performance and Goals for Tevatron parameters. Run Ib parameters are also provided for comparison when available. 32
3.2 The parameters of the SVX II detector geometry. The parameters of the silicon vertex detector in RunIb (SVX') are also listed for comparison. 42
3.3 Design parameters of CDF II calorimeters, X_0 is the radiation length , λ is the hadronic interaction length, $\oplus$ means that the constant term in the energy resolution is added in quadrature. 47

5.1 A summary of the yield of $\bar{B}^0$ with different fit models and different cuts. 78
5.2 Parameter central values, uncertainties and global correlation coefficients from the fit. 93
5.3 A summary of the effects (in number of events) of various changes to the fit conditions. 105
5.4 Table of the 'trigger efficiency' –the probability that a $\Lambda_b^0 \to \Lambda_c^+ \pi^-$ or $\bar{B}^0 \to D^+ \pi^-$ candidate passes the Two Track Trigger selection criteria. 107
5.5 Table of the 'offline reconstruction efficiency' – the probability that all four tracks from the $\Lambda_b^0 \to \Lambda_c^+ \pi^-$ or $\bar{B}^0 \to D^+ \pi^-$ candidate decay are reconstructed, given that this event has already satisfied the Two Track Trigger. 108
5.6 Table of 'analysis efficiency' – the probability that the $\Lambda_b^0 \to \Lambda_c^+ \pi^-$ or $\bar{B}^0 \to D^+ \pi^-$ candidate passes all analysis cuts, given that it passed both the Two Track Trigger cut and that all four ultimate daughters are reconstructed as offline tracks. 109

5.7 Summary of efficiency ratios. 109

6.1 The main resonance states among decay modes of Λ_c^+ 112
6.2 A summary of the sources of the systematic uncertainty. 120

Chapter 1

Introduction

The final purpose of particle physics is to answer two questions " What is the world made of" and "what holds it together".

1.1 Brief History

Even in ancient times, people already thought the world was made from some fundamental building blocks. The ancient Greek thought the world was made from four basic components: earth, fire, air and water. The ancient Chinese believed the five elements theory: metal, wood, water, fire, earth. However, without our modern physical science methods and experimental technology, ancient philosophers couldn't go further than speculation.

The scientific approach to the above two questions began in the 19th century. In the early 19th century J.Dalton developed his atom hypothesis: matter is composed of small particles called atoms. The theory was based on experimental data about chemical reactions. Later, D.Mendeleev's periodic table proved the success of atomic theory. Atoms seemed to be the fundamental particles of the world until the discovery of radioactivity in the late 19th century by H.Becquerel, Pierre and Marie Curie. At about the same time as radioactivity was discovered, J.J.Thomson found a negatively charged particle coming from different atoms. He concluded that this particle is part of every atom, and, thus, is a subatomic particle. Later, it became known as the

electron. Since atoms are electrically neutral, there must be another positive part of atom. In the early 20th, E.Rutherford demonstrated that there is a hard center to the atom which he called the nucleus. Then he discovered that this nucleus contains a positively charged particle, called the proton. In 1932, J.Chadwick identified an electrically neutral particle, called the neutron, which also comes from the nucleus. During the same period, the photon, which is made of light, was shown to behave like a particle.

There is also antimatter in this world! In 1930, Dirac predicted that there is an antiparticle of the electron based upon his equation of motion for the electron. In 1932 this antiparticle was observed by C.Anderson.

Meanwhile on the theoretical front, physicists were also working very hard to develop a suitable theory to explain how electrons, protons and neutrons are held together. This theory would describe the subatomic world. In 1900 M.Planck first used quantized energy to explain the black body radiation. In 1905 Einstein used quantized light to explain the photoelectric effect. Later, in 1913 N.Bohr used quantized angular momentum to explain how electrons surround the nucleus inside atoms. Through the contributions of many talented physicists like de Broglie, Schrodinger, Heisenberg and Born, Quantum Mechanics became the basic theory for understanding the subatomic world. By the 1930's, physicists believed that the elementary particles which made up our world were electrons, protons, neutrons and photons. They also believed that there were four different interactions between particles: the strong, the weak,the electromagnetic and the gravitational interactions. The particles can be divided into different groups by the interaction between them. The particles that interact only weakly or electromagnetically, such as the electrons, are called "leptons". The particles that interact strongly, such as the proton and the neutron, are called "hadrons". A particle like the photon is called a force carrier. It exists when particles are interacting with each other.

Physicists felt fairly satisfied about understanding the elementary particle world, but the adventure of finding new "elementary" particle continued. By studying cosmic rays, the muon (μ) was discovered in 1937 and the pion (π) was found in 1947. After that, many new particles were discovered at particle accelerators. By the 1960's there

were already more than one hundred of them. The properties of those particles were studied: the mass, lifetime, how they decay. Based on experimental data, theorists wanted to develop some theory to group this suddenly large zoo of new particles. They felt those new particles should not be all elementary particles if there were more than one hundred of them. In 1964 Gell-Mann and Zweig independently realized that there are some more fundamental constituent particles in the hadrons. Gell-Man named them "quarks". In their theory the hadrons which consists of three quarks are called baryons, like the proton and neutron. The hadrons which consist of a quark and an anti-quark are called mesons, like the pion. At the beginning there were only 3 quarks in the theory, namely "up quarks", "down quarks", "strange quarks". Soon theoretical physicists needed another one to explain some experimental results and experimental physicist found it for them. In 1974 two experiments directed by S.Ting and B.Ritcher independently discovered a particle called the J/ψ meson which is made of the fourth quark (charm quark). In the following 20 years, a fifth and sixth quark (bottom quark, top quark) were proposed and discovered, and some more leptons and force carrier particles were discovered also.

Today, physicists believe that the world is made by six quarks and six leptons. There are four kinds of interactions between them. There are also a group of elementary particles that are carriers of different interactions. The successful theory to describe those elementary particles and their interactions is called the Standard Model.

1.2 High Energy Physics

Looking back over the past 200 years, physicists' knowledge about the elementary particles improved greatly. They kept making breakthroughs along two different front lines. Experimentalists discovered the new phenomena from nature. Theorists developed new theories with mathematical models to explain experimental data and predict more new phenomena. Then experimentalists tested these models and sometimes verified those predictions.

The objects which particle physicists study are many kinds of particles and do

not exist on the energy and time scales of human life. All are very tiny. Common microscopes can not see them at all. The shorter the distances we want to study, the higher the energy we need. Some particles are very heavy compared to the electron or proton. To create them, based on Einstein's famous equation $E = mc^2$, we need high energy again. That is why particle physics is also called high energy physics.

Experimentalists need some tools to create and study particles. The particle accelerator is one such tool. For example, the accelerator, nicknamed Tevatron, is at The Fermi National Accelerator Laboratory (FNAL). The FermiLab Tevatron, the most powerful accelerator in the world, accelerates proton and anti-proton beams to nearly the speed of the light and then lets them smash into each other. The energy produced from the collision is converted into showers of particles, which allows physicist to study the properties of those particles and find the traces of new particles. The lifetime of most of those particles are very short, i.e., 10^{-12} to 10^{-23} seconds. They decay into other particles right after being produced. Some of the decay products decay again. So experimental physicists also need detectors to measure and store information for those decay products and then trace back to reconstruct the original particles. The Collider Detector at FermiLab (CDF) is one of the detectors at the Tevatron collision points.

Although the Standard Model is a very successful theory and has been tested in many ways, there are still some questions that it can not answer. For example, why particles have mass, why there are only 6 quarks, why there is more matter in our universe than antimatter. Physicists believe there are some new physics phenomena beyond the Standard Model. Experimental physicists need to find them. Some new theories like Supersymmetry and String Theory exist. They also need experimental physicists to verify them. There are many ways to do it. Physicists can search for new particles predicted by new theories directly, or they can try to measure the properties of existing particles precisely and compare with the predictions of the current theory. For example, in this thesis a new decay mode of a baryon named Λ_b^0 will be studied and the branching ratio of this decay will be measured and compared with theoretical predications.

1.3 Outline of the Thesis

In this analysis,the result of a measurement of the decay branching ratio of a heavy baryon, Λ_b^0 , is presented. This is the world's first measurement of the decay channel $\Lambda_b^0 \to \Lambda_c^+ \pi^-$. In Chapter 2, the theoretical background and motivation for this measurement is introduced. In Chapter 3 the experimental apparatus used to perform this measurement is described. Both the FermiLab Tevatron accelerator and the CDF detector are described, with emphasis on the detector components relevant to this analysis. The data set used in this analysis and the techniques used to reconstruct the interesting events are discussed in Chapter 4. The method of the measurement and the whole process of the analysis are presented in Chapter 5 with details. The estimation of systematic uncertainties for the measurement follows in Chapter 6. Finally, results and conclusions are presented and discussed in Chapter 7.

Chapter 2

Theory

2.1 The Standard Model

The Standard Model [1, 2] is so far the most successful theory to explain all known particle physics phenomena. It is a theoretical framework based on gauge theories [3, 4] to describe the elementary particles and their interactions and has survived many precise experimental tests [5, 6].

2.1.1 Particles, Interactions and Gauge Symmetries

In the Standard Model, the elementary particles are point-like, the size of them being less than $10^{-18} - 10^{-19}m$. There are two types of elementary particles: matter particles and force carrier particles.

The matter particles, including quarks and leptons, are fermions with spin $s = 1/2$. There are 6 quarks: up(u), down(d), charm(c), strange(s), top(t) and bottom(b); and 6 leptons: electron(e), muon(μ), tau(τ) and their corresponding neutrinos ν_e, ν_μ, ν_τ. Both quarks and leptons are separated into 3 families.

$$\begin{pmatrix} u \\ d \end{pmatrix} \quad \begin{pmatrix} c \\ s \end{pmatrix} \quad \begin{pmatrix} t \\ b \end{pmatrix}$$

$$\begin{pmatrix} e^- \\ \nu_e \end{pmatrix} \quad \begin{pmatrix} \mu^- \\ \nu_\mu \end{pmatrix} \quad \begin{pmatrix} \tau^- \\ \nu_\tau \end{pmatrix}$$

Quark	Mass (MeV)	Charge	Lepton	Mass (MeV)	Charge
d	3-9	$-\frac{1}{3}$	e	0.511	-1
u	1.5-5	$+\frac{2}{3}$	ν_e	~ 0	0
s	75-170	$-\frac{1}{3}$	μ	105.7	-1
c	(1.1-1.4)$\times 10^3$	$+\frac{2}{3}$	ν_μ	< 0.17	0
b	(4.1-4.4)$\times 10^3$	$-\frac{1}{3}$	τ	1777	-1
t	$(173.8 \pm 5.2) \times 10^3$	$+\frac{2}{3}$	ν_τ	< 18.2	0

Table 2.1: Masses and Charges of Quarks and Leptons(The charge is in units of the absolute electron charge.)

Their masses and charges are listed in Table 2.1. The quarks have an additional quantum number, the color. There are three types: red, green and blue. Because the quantum number, color, is not seen in Nature, quarks must be combined into the experimentally observed and colorless matter particles: baryons and mesons. The baryons are made of three quarks and the mesons are made of one quark and one anti-quark. For example, the proton is a baryon which is made of two u quarks and one d quark (uud). The Λ_b^0 is a baryon which is made of one u quark, one d quark and one b quark (udb). The π^+ is a meson made by one u quark and one anti d quark ($u\bar{d}$). And the B^0 is a meson made by one d quark and one anti b quark ($d\bar{b}$).

The force carrier particles are bosons with spin equal to an integer. There are four different known forces or interactions acting on matter. Gravity is negligibly small at the energy scale of elementary particles. In the Standard Model, the other three forces are mediated by exchanging force carrier particles. The eight gluons, $g_\alpha, \alpha = 1, ..8$, are exchanged when there are strong interactions among quarks. The photon, γ, is the force carrier particle in the electromagnetic interactions, and the $W^\pm, Z$ are the exchanged particles in the weak interactions. The properties of the

Force	Range(m)	Carrier	Mass (MeV)	Charge
Electromagnetic	∞	Photon	0	0
Weak	$\sim 10^{-18}$	$W^{\pm}$	$(80.41 \pm 0.10) \times 10^3$	± 1
		Z^0	$(91.187 \pm 0.007) \times 10^3$	0
Strong	$\sim 10^{-15}$	Gluons	0	0

Table 2.2: Masses and Charges of Gauge Bosons (The charge is in units of the absolute electron charge.)

interactions and their force carriers are listed in the Table 2.2. The Standard Model is based on the gauge symmetry of $SU(2)_L \times U(1)_Y$ electroweak interactions and the $SU(3)_C$ strong interactions, thus $SU(3)_C \times SU(2)_L \times U(1)_Y$. The symmetry of $U(1)_{em}$ electromagnetic interaction is a subgroup of $SU(2)_L \times U(1)_Y$. Gauge invariance does not allow mass terms in the Lagrangian for the gauge bosons. This is not consistent with the experimental observation of the massive electroweak bosons $W^{\pm}, Z^0$. On the other hand, the photon is massless which indicates that the $U(1)_{em}$ is a good symmetry of vacuum. The mechanism to generate the masses for $W^{\pm}, Z^0$ bosons and fermions must be implemented as $SU(3)_C \times SU(2)_L \times U(1)_Y \rightarrow SU(3)_C \times U(1)_{em}$. This is called "Spontaneous Symmetry Breaking". However, this theory predicts another new particle, the Higgs, which has not been found yet.

2.1.2 Quantum Chromodynamics (QCD)

Quantum Chromodynamics is the part of the Standard Model for strong interactions of quarks and gluons. It is a gauge theory based on the symmetry group $SU(3)_C$. Here C stands for colors of quarks. Each quark has 3 possible color states. The gluons have eight combinations of colors, which corresponds to the number of SU(3) generators. The Lagrangian of QCD is written in terms of the quark and gluon

fields.

$$\mathcal{L}_{QCD} = i\sum_q \bar{\psi}_q^i \gamma^\mu (D_\mu)_{ij} \psi_q^j - \sum_q m_q \bar{\psi}_q^i \psi_{qi} - \frac{1}{4}(F_{\mu\nu}^\alpha(x))^2 \tag{2.1}$$

$$F_{\mu\nu}^\alpha = \partial_\mu A_\nu^\alpha - \partial_\nu A_\mu^\alpha + g_s f^{abc} A_\mu^b A_\nu^c \tag{2.2}$$

$$(D_\mu)_{ij} = \delta_{ij}\partial_\mu - i g_s \sum_a \frac{\lambda_{ij}^a}{2} A_\mu^a \tag{2.3}$$

where,

$\psi_q^j(x)$ are quark fields; i=1,2,3
$F_{\mu\nu}^\alpha$ is the strength of the gluon fields
A_μ^a are gluon fields; a=1, ...,8
g_s is strong coupling constant
f^{abc} is the structure constants of SU(3) algebra
$\frac{\lambda_{ij}^a}{2}$ is SU(3) generators.

The last term in $F_{\mu\nu}^\alpha$ will generate three and four gluon self-interactions. The self-interactions are a new feature in QCD and explain the quark color confinement and asymptotic freedom. From Deep Inelastic Scattering (DIS) experiments, we know the interaction is very strong at low energies (confinement) and very weak at very high energies. At high energies quarks behave almost freely (Asymptotic freedom). The Lagrangian 2.1 only has one single coupling constant g_s and can not explain both energy scales if g_s is always the same. The renormalization of QCD introduces a redefinition of the QCD coupling $\alpha_s(Q^2)$. Here $\alpha_s = g_s/(4\pi)$. It is a function of the transferred momentum Q^2.

$$\alpha_s(Q^2) = \frac{\alpha_s \mu^2}{1 - \frac{\beta_1 \alpha_s(\mu^2)}{2\pi} ln(Q^2/\mu^2)} \tag{2.4}$$

where

$$\beta_1 = \frac{2N_f - 11N_C}{6}. \tag{2.5}$$

In QCD, the number of flavors, N_f, is six and the number of colors, N_C, is 3, so β_1 is negative. That means α_s decreases when Q^2 increases, thereby explaining asymptotic freedom. To have a reference scale to determine if a given Q^2 is large or small, a

constant Λ_{QCD} is chosen as in Eq. 2.6. When the α_s becomes large giving strong coupling, QCD is non-perturbative. Roughly, $\Lambda_{QCD} \sim 0.2$ GeV is the energy scale that determines the regions of large or small coupling.

$$ln\Lambda = ln\mu + \frac{\pi}{\beta_1 \alpha_s(\mu^2)} \tag{2.6}$$

$$\alpha_s(\mu^2) = \frac{2\pi}{-\beta_1 ln(\mu^2/\Lambda^2)} \tag{2.7}$$

From Equation 2.7 when $\mu >> \Lambda$, $\alpha_s(\mu^2) \to 0$, one has the asymptotic freedom situation. When $\mu \to \Lambda$, $\alpha_s(\mu^2) \to \infty$, and one has color confinement at low energies. However, at this low energy scale the perturbation theory breaks down, and we can't get information from QCD.

2.1.3 Electroweak Theory

Electroweak Theory is the part of the Standard Model for electromagnetic and weak interactions. It is a gauge theory based on the Symmetry group $SU(2)_L \times U(1)_Y$. $SU(2)_L$ is the weak isospin group. The subscript L means only left-handed fermions interact weakly. The right-handed components are weak-isospin scalars. In the electroweak theory, the fermions are left-handed doublets and right-handed singlets. There are no right-handed neutrinos. Neutrinos are massless.

$$\begin{pmatrix} e^- \\ \nu_e \end{pmatrix}_L, \quad \begin{pmatrix} \mu^- \\ \nu_\mu \end{pmatrix}_L, \quad \begin{pmatrix} \tau^- \\ \nu_\tau \end{pmatrix}_L, \; e_R^-, \; \mu_R^-, \; \tau_R^-$$

$$\begin{pmatrix} u \\ d \end{pmatrix}_L, \quad \begin{pmatrix} c \\ s \end{pmatrix}_L, \quad \begin{pmatrix} t \\ b \end{pmatrix}_L, \; u_R, \; d_R, \; c_R, \; s_R, \; t_R, \; b_R$$

$U(1)_Y$ is the weak hypercharge group, where $Y = 2 \times (Q - T_3)$ is the hypercharge, Q is the electric charge, T_3 is the third component of weak isospin. In this way, $U(1)_{em}$ becomes a subgroup of the total electroweak group, thus unifying electromagnetic and weak interactions. The electroweak Lagrangian can be written as

$$\mathcal{L}_{EW} = \mathcal{L}_f + \mathcal{L}_G + \mathcal{L}_{SBS} + \mathcal{L}_{YW}. \tag{2.8}$$

The fermion term, including the kinetic and interaction terms, can be written as

$$\mathcal{L}_f = \sum_{f=l,q} \bar{f} i \not{D} f. \tag{2.9}$$

The gauge part includes gauge boson kinetic energy terms and gauge boson self-interaction terms,

$$\mathcal{L}_G = -\frac{1}{4} W^i_{\mu\nu} W_i^{\mu\nu} - \frac{1}{4} B_{\mu\nu} B^{\mu\nu} \tag{2.10}$$

where

$W^i_{\mu\nu} = \partial_\mu W^i_\nu - \partial_\nu W^i_\mu + g\epsilon^{ijk} W^j_\mu W^k_\nu$
$B_{\mu\nu} = \partial_\mu B_\nu - \partial_\nu B_\mu.$

The $W^i_\mu,\ i = 1, 2, 3$, are SU(2) gauge fields. B_u is a U(1) gauge field. Respectively, g' and g are the corresponding gauge coupling constants. The physical gauge bosons $W^\pm_\mu$, Z^0 and A_μ are obtained from electroweak eigenstates as follows:

$$W^\pm_\mu = \tfrac{1}{\sqrt{2}}(W^1_\mu \mp i W^2_\mu)$$
$$Z_\mu = \cos\theta_w W^3_\mu - \sin\theta_w B_\mu$$
$$A_\mu = \sin\theta_w W^3_\mu + \cos\theta_w B_\mu$$

where $\tan\theta_w = g'/g$.

The two terms $\mathcal{L}_{SBS}$ and $\mathcal{L}_{YW}$ are the Symmetry Breaking Sector Lagrangian and the Yukawa Lagrangian. The two terms are used to provide the experimentally observed $W^\pm$ and Z^0 gauge bosons masses and also the fermions masses. Because of the requirement of $SU(2)_L \times U(1)_Y$ gauge invariance, mass terms for gauge bosons and fermions are not allowed in the Lagrangian. Spontaneous Symmetry Breaking and the Higgs Mechanism are used to generate those mass terms. The symmetry breaking part of the Lagrangian is

$$\mathcal{L}_{SBS} = (D^\mu \phi)^\dagger D_\mu \phi - V(\phi) \tag{2.11}$$

where, $\phi = \begin{pmatrix} \phi^+ \\ \phi^0 \end{pmatrix}$ is a complex Higgs scaler and is a doublet under SU(2). The gauge covariant derivative is

$$D_\mu \phi = (\partial_\mu + ig\frac{\tau^i}{2} W^i_\mu + \frac{ig'}{2} B_\mu)\phi \tag{2.12}$$

where the τ^i are Pauli matrices. The square of this term leads to interactions between the gauge and scalar fields. $V(\phi)$ is the Higgs potential

$$V(\phi) = \mu^2 \phi^\dagger \phi + \lambda(\phi^\dagger \phi)^2. \tag{2.13}$$

When $\mu^2 < 0$ there will be spontaneous symmetry breaking. The λ term is the self interaction between scalar fields.

The last term of the Electroweak Lagrangian is the fermion mass term:

$$\mathcal{L}_{YW} = \lambda_e \bar{l}_L \phi_{eR} + \lambda_u \bar{q}_L \tilde{\phi}_{uR} + \lambda_d \bar{q}_L \phi_{dR} + h.c. + 2^{nd} \; and \; 3^{rd} \; families. \tag{2.14}$$

After spontaneous symmetry breaking, the mass terms are :

$M_W = \frac{g\nu}{2}$; $M_Z = \frac{\sqrt{g^2+g'^2}\nu}{2}$
$M_H = \sqrt{2}\mu$
$m_e = \lambda_e \frac{\nu}{\sqrt{2}}$; $m_\mu = \lambda_\mu \frac{\nu}{\sqrt{2}}$; $m_d = \lambda_d \frac{\nu}{\sqrt{2}}$; $\cdots$
where $\nu = \sqrt{\frac{\mu^2}{\lambda}}$.

We can see that all masses are given in terms of a mass parameter ν and the couplings g, g', λ, λ_e, etc.. Because ν can be determined from experiments, the masses of M_W and M_Z can be predicted by the Standard Model. Then the comparison between experimental results and theoretical predictions provides a good way to test the Standard Model.

2.1.4 Beyond Standard Model

Except for the fact that the Higgs boson has not been discovered, the Standard Model is a very successful theory. Can we just find the Higgs particle and declare the close of particle physics? Most physicists believe there is physics beyond the Standard Model. The reasons are from both conceptual problems and phenomenological indications.

- Gravity Problem: Quantum gravity is not included in the SM. There is no obvious method to unify gravity in the SM context.

- Hierarchy Problem: the Higgs Field is introduced into the SM to generate the masses for W, Z bosons and fermions. To be consistent, the mass of the Higgs particle should not be too different from the W mass. However, the radiative loop corrections from self-interactions, interactions with gauge bosons and fermions could make the Higgs mass much larger than expected if there is higher scale theory.

- Gauge Problems: The SM is built on $SU(3) \times SU(2) \times U(1)$. The SM can not explain why only the SU(2) part is parity violating.

- Fermion Problem: The SM can not explain why there are only 3 generations of fermion families, why the top quark mass is much heavier than the others or why the charges of particles are multiples of e/3.

- Inexplicable Phenomena: There are a series of phenomena in the universe that the SM can not explain: dark matter, baryogenesis, neutrino mass, the cosmological vacuum energy.

It is possible that the SM is a subgroup of a larger unified gauge group, for example, some GUTs (Grand Unified Theories). Under those GUTs, all interactions are unified and the SM is an effective theory valid up to some cut-off energy scale. The GUTs could explain questions like neutrino mass, baryon anti-baryon asymmetry. For explaining the Hierarchy problem, theories like Supersymmetry (SUSY), Technicolor, Large extra dimensions have been developed. Active searches for new physics predicted by these models are underway at many High Energy Experiments, including CDF.

2.2 The Bottom Quark

In 1977 a resonance at $\sim$ 9.5 GeV was observed at a FermiLab fixed target experiment, where 400 GeV protons collided with nuclei [7]. It was soon confirmed by experiments at DESY [8]. Soon thereafter, the resonance was found to be two narrow resonances at 9.44 GeV and 10.17 GeV. They were understood as two bound

states of $b\bar{b}$ and were called bottomonium (Υ, Υ'). The discovery of the b quark proved the existent of the third generation of matter. Since the single b quark is a color object, it cannot exist independently because of QCD color confinement. Once a b quark is produced, it has to bind with other quarks to become a color neutral object. This process is called hadronization or fragmentation. The hadrons that contain a b quark are usually called B hadrons, for instance $B_d^0(\bar{b}d), B_u^+(\bar{b}u), B_s^0(\bar{b}s), B_c^+(\bar{b}c)$ and $\Lambda_b^0(bdu)$. The study of the physics related to bottom quarks is interesting for both experimental and theoretical physicists. The phenomena observed within the B hadron systems like CP violation, flavor changing and rare decays provide important tests for the Standard Model. The precise measurement of those phenomena could reveal the physics beyond the Standard Model. However, the fact that the b quark is confined inside hadrons and that nonperturbative QCD plays an important role at the hadron level means it is a big challenge for theoretical physicists to untangle the wanted information from nonperturbative effects. Theoretical and experimental physicists have to work together to find the quantities that can be predicted from theoretical approaches and can be measured in experiments.

Several different accelerators have been used to study b quarks. The b quark pair can be produced at dedicated e^+e^- colliders at center-of-mass energy equal to the peak of Υ, a bottomonium state. This is done at Cornell, SLAC and Japan. It can also be produced with the center-of mass energy tuned to the Z^0 peak as was done at SLAC and CERN. Another place to produce b quark pairs is in a $p\bar{p}$ collider, for example at the FermiLab Tevatron. The cross section to produce b quark pairs at the $\Upsilon(4S)$ peak is $\sim 1\ nb$, at the Z^0 peak is $\sim 7\ nb$, at the $p\bar{p}$ collider with the center-of-mass energy at 1.8 TeV is $\sim 100\ \mu b$. So we can see the cross section is several order of magnitude higher in $p\bar{p}$ collisions. On the other hand, the backgrounds are also much higher in the $p\bar{p}$ collision environment, so doing B physics is both an opportunity and a challenge at a $p\bar{p}$ collider.

2.2.1 b quark Production at $p\bar{p}$ Colliders

Since being discovered in 1911, the understanding of the structure of the proton kept evolving over the years from a pointlike particle to a composite particle containing 3 quarks. Nowadays, the proton is believed to be an object with three "valence" quarks(uud) swimming in a sea of virtual particles including gluons and $q\bar{q}$ pairs. Each component particle, which is called a parton, carries a portion (x) of proton's momentum. In a $p\bar{p}$ collision, the partons from the proton and anti-proton interact and produce $b\bar{b}$ pairs along with other particles. Fig 2.1 shows at leading order how $b\bar{b}$ pairs can be produced from quark anti-quark annihilation ($q\bar{q} \rightarrow b\bar{b}$) and gluon fusion($g\bar{g} \rightarrow b\bar{b}$). Fig 2.2 shows some examples of Feynman diagrams of next-to-leading order $b\bar{b}$ production including radiative correction processes and gluon splitting processes.

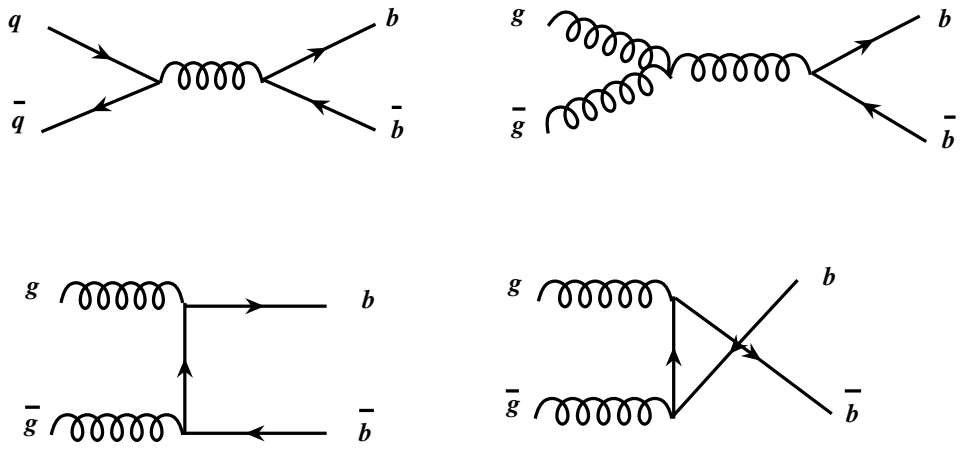

Figure 2.1: Leading order $b\bar{b}$ production Feynman diagrams in $p\bar{p}$ environments

The $b\bar{b}$ production process in a $p\bar{p}$ collision is a QCD process and the cross section can be calculated by perturbative QCD. The CDF collaboration studied the b quark production cross section at the Tevatron with $\sqrt{s}$=1.8 TeV [9, 10, 11]. Fig 2.3

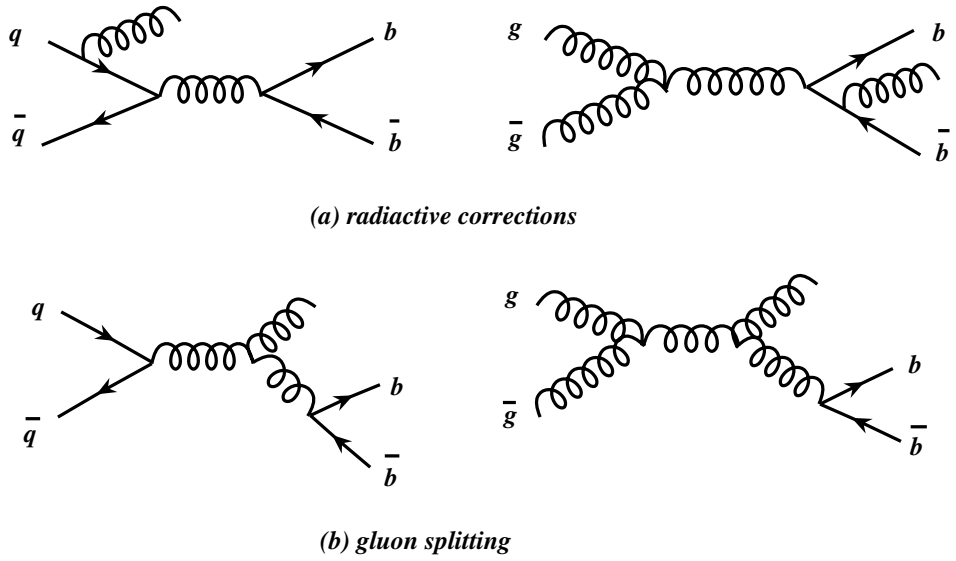

Figure 2.2: Some examples of Next-to-leading order $b\bar{b}$ production Feynman diagrams in $p\bar{p}$ environments

shows the measured integrated b-quark production cross section as a function of its transverse momentum(p_T^b). The measurement used both semi-leptonic channels and J/ψ channels. The comparison with theoretical predications is also made. The solid line is the calculation based on next-to-leading order QCD using the MRSD0 parton distribution functions [12, 13]. We can see that all the data points are about 2$\sim$4 times larger than the theoretical predication, although the shape is consistent between them.

2.2.2 b quark Fragmentation

After b quarks are produced, they will go through a fragmentation process by creating quark pairs from the color force field, and then form hadrons by combining with some of them. The fragmentation process involves soft gluon exchange. Thus, it is a low-energy process. Therefore, unlike the b quark production process, the b quark fragmentation process can not be calculated using perturbative QCD. Several

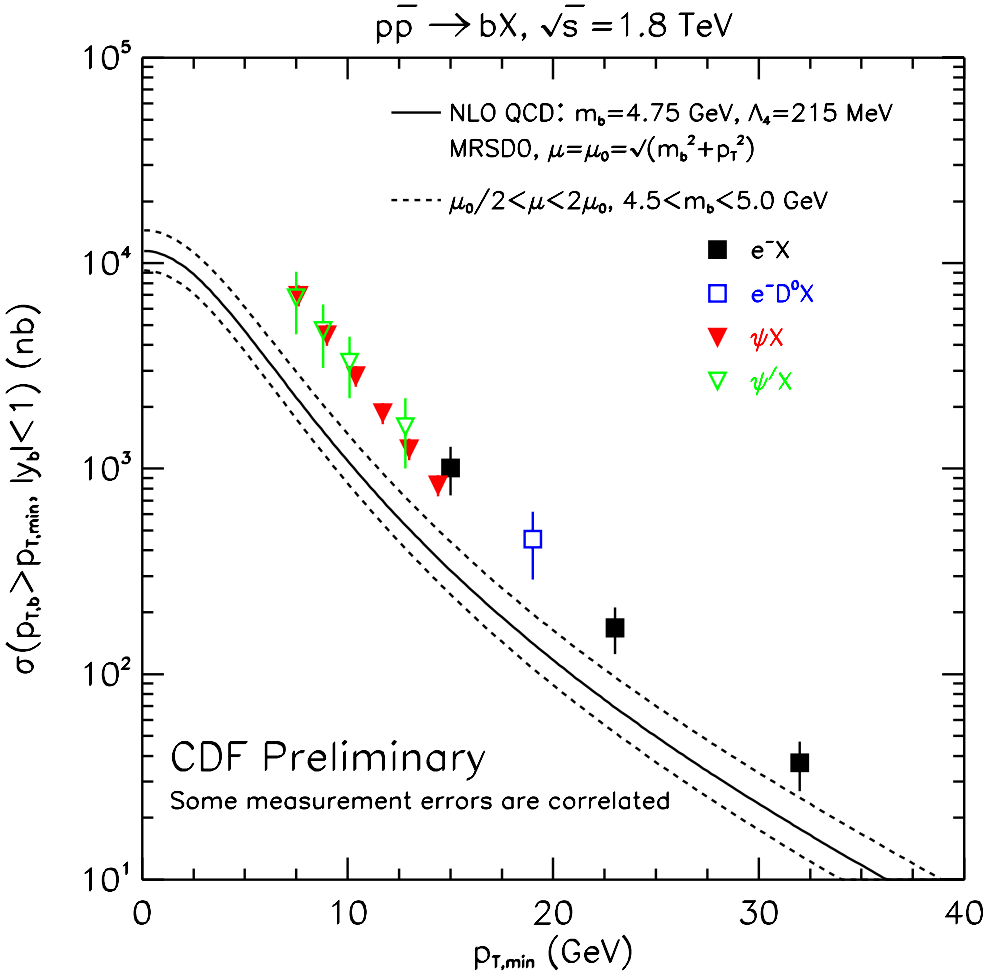

Figure 2.3: The b quark production cross section at CDF

phenomenological models have been developed to describe this process [14, 15]. The two main models are 1) the cluster model and 2) the string model. In the cluster model, the $q\bar{q}$ combinations are assumed to form clusters first, then the clusters decay into hadrons. The problem with this model is that it can not deal with very massive cluster decays and does not suppress baryon and heavy quark production enough. In the string model, a color flux string is stretched between two initial $q\bar{q}$ particles. The string breaks into hadrons in its intense color field. The string model also has problems in describing baryon production but fewer than the cluster model. The schematic diagrams of the two models are shown in the Fig 2.4.

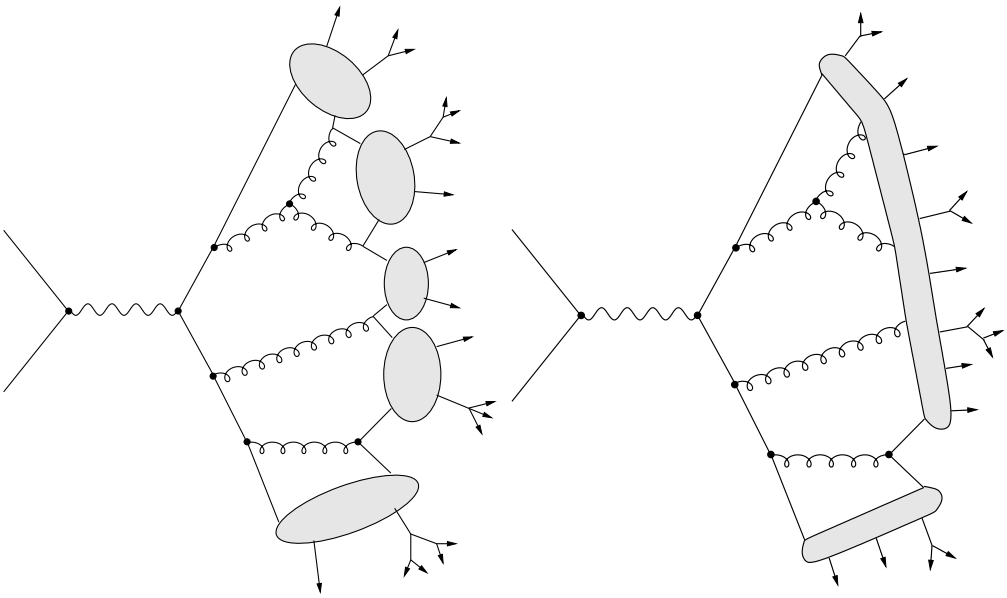

Figure 2.4: The b quark fragmentation process, the left is cluster model, the right is string model. (The figure is from reference [15])

One important method for understanding the fragmentation process is the study of momentum spectra for the heavy quark and the produced hadrons. Many functional forms for the momentum spectra have been suggested, but the most popular one is from Peterson *et al.* [16]. The Peterson fragmentation function is the probability of a heavy quark with momentum p_Q hadronizing to a hadron with momentum p_H after picking up a light anti-quark $\bar{q}$ (or a quark pair qq' in the case of a baryon):

$$\frac{dN}{dz} = \frac{1}{z[1-(1/z)-\epsilon_P/(1-z)]^2} \tag{2.15}$$

where z= $(E_H + p_{H||})/(E_Q + p_Q)$, and $p_{H||}$ is the hadron momentum projection along the direction of the parent heavy quark. The term $1-(1/z)-\epsilon_P/(1-z)$ is proportional to the energy transfer in the process ($\Delta E = E_H + E_q - E_Q$). The parameter ϵ_P is called the Peterson parameter and can be determined from collider experiments. In the e^+e^- annihilation experiments the ϵ_P was determined to be 0.006 ± 0.002 [17]. Although the z in the Peterson function is relativistically invariant with respect to the boosts in the direction of the parent quark, it is not directly accessible in experiments.

The approximate scaling variable $x_p = p_{hadron}/p_{max}$ or $x_E = E_{hadron}/E_{max}$ is usually measured experimentally instead.

During fragmentation, different species of hadrons $B_u^+(\bar{b}u), B_d^0(\bar{b}d), B_s^0(\bar{b}s)$ and $\bar{\Lambda}_b^0(\bar{b}d\bar{u})$ are produced. We define the fractions f_u, f_d, f_s, f_{baryon} as the probabilities that a $\bar{b}$ quark fragments into a B_u^+, B_d^0, B_s^0 and $\bar{\Lambda}_b^0$. From the 2002 Particle Data Group, the world average values of the fragmentation fractions are $f_u : f_d : f_s : f_{baryon} = 38.8\% : 38.8\% : 10.6\% : 11.8\%$. Those values are the combined results from the ALEPH, CDF, DELPHI, L3, OPAL and SLD collaborations [18].

2.3 Heavy Quark Effective Theory(HQET)

2.3.1 Heavy Quark Symmetry

The Standard Model of strong and electroweak interactions is a very successful theory as we described in the previous Section 2.1. However, there are still many open questions, even if we don't count those beyond the Standard Model. For example, Quantum Chromodynamics (QCD) can not provide much analytical information on hadron properties. At a typical hadron size $\sim 1fm$, the strong coupling constant α_s becomes large and leads to nonperturbative phenomena. Reliable predications do not come from perturbative QCD, but instead are based on symmetry principles. An example is Chiral symmetry, which arises in the limit of massless light quarks $(m_\mu, m_d, m_s, \rightarrow 0)$, and is based on the fact that the masses of light quarks are small compared to the scale of nonperturbative QCD [19]. Another example is the heavy quark effective theory which can be used for the study of b hadrons [20].

For a heavy quark Q (c,b,t), $m_Q >> \Lambda_{QCD}$, the coupling constant $\alpha_s(m_Q)$ is small, which means at this length scale ($\lambda_Q \sim 1/m_Q$) the strong interactions are perturbative. In the heavy quarkonium systems, there are only two heavy quarks $Q\bar{Q}$. The size of such systems can be defined as $\lambda_Q/\alpha_s(m_Q)$, which is much smaller than 1fm, so it is easy to make calculations on such systems in a perturbative way. In fact, before the discovery of charmonium and bottomonium, their properties had been predicted [21]. For a system that contains a heavy quark and a light quark(s),

it is more complicated. The heavy quark is surrounded by a cloud of light quarks, anti-quarks and gluons. Such systems can not be calculated perturbatively because the momentum exchanged between the heavy quark and the cloud is of order Λ_{QCD}. However, the fact that $m_Q >> \Lambda_{QCD}$ can still make things simple. To reveal the quantum numbers of the heavy quark, the needed momentum is at least m_Q^2, which is much larger than the momentum carried by the cloud. In other words, the cloud is blind to the mass and spin of the heavy quark. The heavy quark just acts as a static color field. So in the limit of $m_Q \to \infty$, the hadronic system containing a heavy quark $Q(v, s)$ with spin s and velocity v has the same configuration of light degrees of freedom as the hadronic system containing another heavy quark $Q'(v, s')$ with different spin and flavor. Thus, the spin of the heavy quark and the total angular momentum j of the light degrees of freedom are both conserved in strong interactions and the spin and mass of the heavy quark are not important to the properties of hadrons. The hadronic systems that contain a heavy quark can be classified by not only their total spin but also the total spin of the light degree of freedoms. If there are N_h heavy quark flavors, there is an SU($2N_h$) spin-flavor symmetry group. The spin-flavor symmetry can be used to explain the relations between the different hadrons containing a heavy quark. One of the predictions of heavy flavor symmetry is that the mass spectroscopic difference between the following meson states should be the same:

$$m_{B_s} - m_B \sim m_{D_s} - m_D \sim 100 MeV/c^2$$
$$m_{B_1} - m_B \sim m_{D_1} - m_D \sim 557 MeV/c^2$$
$$m_{B_2} - m_B \sim m_{D_2} - m_D \sim 693 MeV/c^2.$$

The first relation agrees with experimental results nicely. From the Particle Data Book, $m_{B_s} - m_B \sim 90\ MeV/c^2$. The next two relations are still waiting for verification because the masses of B_1 and B_2 are not measured precisely in experiments. The theoretical framework developed for the heavy quark symmetry system is called Heavy Quark Effective Theory (HQET) [22, 23].

2.3.2 HQET

It is useful to model the heavy quark symmetry by modifying the QCD Lagrangian and taking the limit of $m_Q \to \infty$. The part of the QCD Lagrangian containing a heavy quark is

$$\mathcal{L}_{QCD} = \bar{Q}(i\not{D} - m_Q)Q. \tag{2.16}$$

To take the $m_Q \to \infty$ limit and fix the four velocity v^μ, we write the quark field in terms of the space-time part:

$$Q = \exp^{-im_Q v\cdot x} Q_v; \quad \not{v} Q_v = Q_v. \tag{2.17}$$

Then the QCD Lagrangian becomes

$$\mathcal{L}_{QCD} \to \mathcal{L}_v = \bar{Q}_v iv\cdot\not{D} Q_v = \bar{Q}_v(iv^\mu\partial_u + gT_a v^\mu A_u^a)Q_v \tag{2.18}$$

where T^a is a color generator. The effective field Q_v annihilates a heavy quark Q, but does not create a corresponding anti-quark, so there is no pair creation in HQET. There are no Dirac matrices in the Lagrangian, so interactions between the heavy quark and gluons don't change the heavy quark's spin. Finally, there is no mass term in the effective Lagrangian. When there are more than one heavy quark and the heavy quarks move at different speeds, the HQET Lagrangian becomes:

$$\mathcal{L}_{HQET} = \sum_{i=1}^{N}\sum_{v} \bar{Q}_v^i iv\cdot\not{D} Q_v^i \tag{2.19}$$

2.4 Λ_b baryon and its decay rate

The Λ_b^0 baryon is the lightest baryon predicted by the Standard Model that contains a b quark. In 1991, the UA1 collaboration claimed the first observation of the Λ_b^0 in the decay channel $\Lambda_b^0 \to J/\psi\Lambda$ using 4.7 pb^{-1} of data from the CERN proton anti-proton collider [24]. Their measured Λ_b^0 mass was $5640 \pm 50 \pm 30$ MeV/c^2 and the branching fraction $B(\Lambda_b^0 \to J/\psi\Lambda) = (1.8 \pm 1.0) \times 10^{-2}$. However, both the Collider Detector at Fermilab (CDF) and LEP experiments at CERN didn't see this decay and set upper limits on the branching fraction which were smaller than UA1's

result [25, 26]. This discrepancy was settled by CDF's new measurement in 1997 [27]. Using 110 pb^{-1} data taken during the 1992-1995 run, CDF gives the branching fraction $B(\Lambda_b^0 \rightarrow J/\psi\Lambda) = (3.7 \pm 1.7) \times 10^{-4}$ and the Λ_b^0 mass at $5621 \pm 4 \pm 3$ MeV/c^2 discrediting the UA1 claim. Other Λ_b^0 decay channels are also studied by CDF and several LEP experiments. The Λ_b^0 lifetime is measured from its semi-leptonic decay $\Lambda_b^0 \rightarrow \Lambda_c^+ \, l^- \bar{\nu}$ [28, 29, 30, 31]. The Λ_b^0 events in the decay channel $\Lambda_b^0 \rightarrow \Lambda_c^+ \, \pi^-$ are also observed by both the ALEPH and DELPHI collaborations [32, 33].

In the above three decay channels, Λ_b^0 decays via the $b \rightarrow c$ transition by emitting a virtual W boson. The lowest order decay processes are shown in Fig 2.5. In Fig 2.5(a), the quarks from W decay join the other spectator quarks to form a Λ and J/ψ. This is called internal W emission. In Fig 2.5(b) and (c), the W decays into leptons or a quark pair that forms into a single hadron. This is called external W emission. From the decay diagram, we can see that to decay into J/ψ Λ , the virtual W has to decay into one c quark and one other quark, so the c quark can be used to form a color singlet J/ψ. Therefore, this process is color-suppressed and should have a smaller branching ratio than the other two decay channels.

Simultaneous with the new experimental measurements of Λ_b^0 baryon properties, the theoretical study of heavy hadron decays is also making progress. The development of the heavy quark effective theory (HQET) simplifies the study of the heavy hadrons. However, HQET can not give the final predictions of hadron decay properties. As we mentioned in Section 2.3.1, only relations between heavy hadrons can be predicted by heavy quark symmetry. In the end the nonperturbative QCD models still have to be used to do the calculations. Furthermore, in comparison to the significant progress made in the heavy meson decay studies, the heavy baryon studies are more complicated, and, thus progress more slowly because there are three quarks in the baryons. Hence, the study of heavy baryon decays is still of great interest to theoretical physicists.

In the three decay channels we mentioned above, the semi-leptonic decay is the simplest in the theoretical view because the lepton pair has no strong interactions with other quarks and can be extracted from the hadronic weak transition form factor. The non-leptonic Λ_b^0 decay is more complicated. The decay $\Lambda_b^0 \rightarrow J/\psi\Lambda$ is relatively

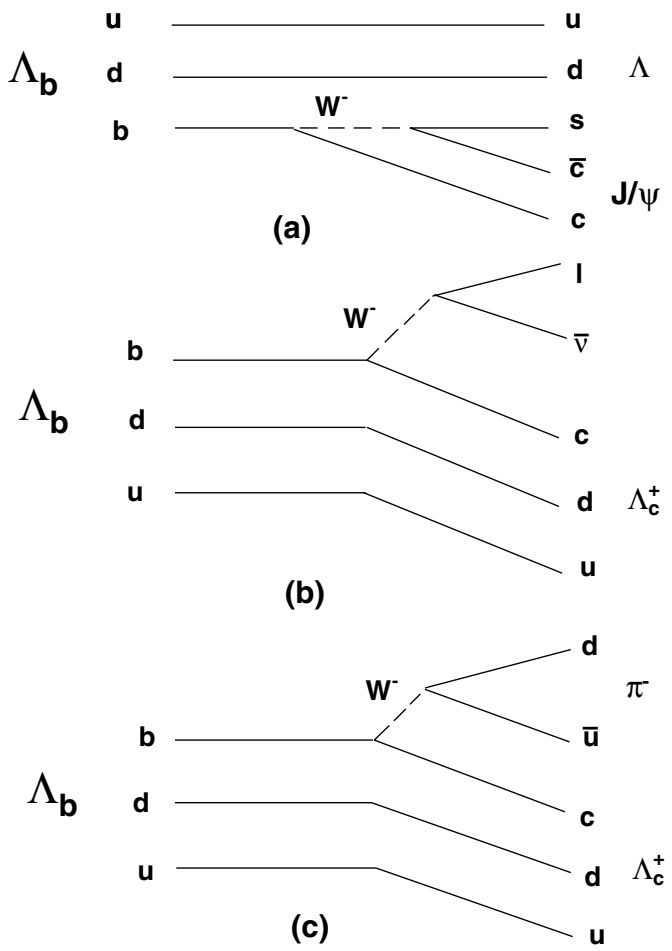

Figure 2.5: Lower order Λ_b^0 decay diagrams, all three channels are via b $\rightarrow$c transition.

easier than the decay $\Lambda_b^0 \rightarrow \Lambda_c^+ \pi^-$ because it is can be described by factorizing quark diagrams alone. The hardest one theoretically is the decay $\Lambda_b^0 \rightarrow \Lambda_c^+ \pi^-$, and, moreover, there are no experimental results on branching ratios on this channel available. This makes the analysis in this thesis even more important.

In this thesis, we will present the experimental result for the decay branching ratio of one of the Λ_b^0 non-leptonic decay channels, $\Lambda_b^0 \rightarrow \Lambda_c^+ \pi^-$. The result will provide important testing information for all possible theoretical approaches. Below, some of the theoretical approaches for decay rate predictions will be discussed and will be

Branching Ratio(10^{-3})	model
$1.8a_1^2 \sim 3.2a_1^2$	B-S model($m_{b,c} \to \infty$)
$0.73a_1^2 \sim 1.4a_1^2$	hadronic wave function($m_{b,c} \to \infty$)
$0.88a_1^2 \sim 3.9a_1^2$	hadronic wave function(with $1/m_Q$ correction)

Table 2.3: Predictions for $\Lambda_b \to \Lambda_c \pi^-$ branching ratio from reference [34]

used to compare with our result.

- In the reference [34], the two body non-leptonic weak decay $\Lambda_b \to \Lambda_c P(V)$ is studied using two models. One is the Bethe-Saltpeter(B-S) model and the other is the hadronic wave function model. In the calculation the factorization assumption is applied. This could simplify the calculation because one of the currents in the decay Hamiltonian is factorized out and forms a meson. This assumption is based on the fact that in the energetic weak decays the quark pair generated from one current moves very fast away from the weak interaction point. So the pair almost does not interact with the remaining quarks when forming a meson. However, the W-exchange diagrams are also involved in the process. The argument is that in the bottom baryon case the contribution of the W-exchange diagrams is suppressed by one order of magnitude. The result is shown in the Table 2.3, where a_1^2 is the parameter involving hadronization effects. Its value is determined experimentally to be roughly $a_1^2 \sim 1$.

- In the reference [35], $\Lambda_b \to \Lambda_c$ weak decays are analyzed in the framework the heavy quark effective theory (HQET). After simplifying the weak decay form factor using HQET, some nonperturbative methods are still needed to complete the calculation. In the paper, two nonperturbative methods, "QCD sum rules" and "large N_c limit", are applied. The result from another method "quark models" is also presented as a reference. In the calculation, the factorization assumption is also used. The numerical results are listed in the Table 2.4.

Branching Ratio(10^{-3})	model
9.6	QCD sum rule
5.0	large N_c limit
4.2	quark model

Table 2.4: Predictions for $\Lambda_b \to \Lambda_c \pi^-$ branching ratio from reference [35]

- In the reference [36], exclusive non-leptonic decays of bottom baryons are studied using a relativistic three-quark model with a Gaussian shape for the momentum dependence of the baryon-three-quark vertex. In this paper, non factorizing contributions are also considered. The result shows that about $\sim 30\%$ of the amplitude comes from the nonfactorizing contribution in the $b \to c\bar{u}d$ transitions. The branching ratio of the decay $\Lambda_b \to \Lambda_c \pi^-$ is given as 4.7×10^{-3}.

Chapter 3

Experimental Apparatus

The Fermi National Accelerator Laboratory (FermiLab) hosts the world's highest-energy particle accelerator, the Tevatron. The proton and anti-proton beams are accelerated in the Tevatron and collide with each other. The particle detectors are placed at the colliding points to study the nature of the matter. Fig 3.1 shows an aerial view of FermiLab.

3.1 The Accelerators

At FermiLab a complex chain of eight accelerators is used to provide the final accelerated proton and anti-proton beams. Fig 3.2 is a diagram of the Fermi accelerator chain. In 1996 the Fermi Accelerators were shut down for a major upgrade for increasing both the center mass energy and the luminosity. The new accelerators began commissioning in March, 2001, and the new data taking period called Run II began.

The proton source:

All protons stored in the Tevatron start from a bottle of compressed hydrogen gas. Hydrogen atoms are ionized to H^- ions by adding an electron to each of them. Then the H^- ions are accelerated to 750 KeV in the Cockcroft-Walton accelerator. Then the linear accelerator (LINAC) accelerates the H^- ions to 400 MeV. The original

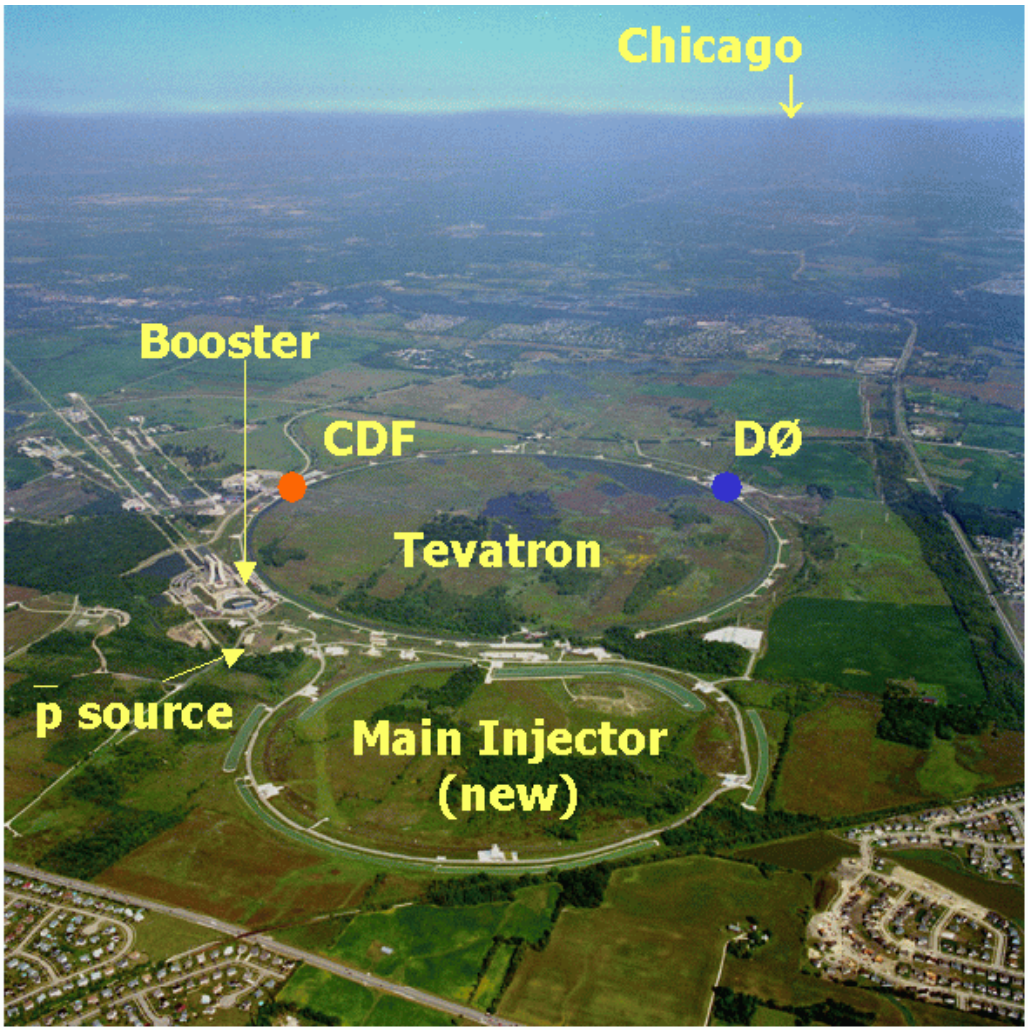

Figure 3.1: An aerial view of FermiLab Accelerator chain.

LINAC built in 1973 used a 201.25 MHz electric field to bring the beam to 200 MeV. In 1993 the last portion of the LINAC was replaced with a more modern structure running at 805 MHz which could accelerate the beam to 400 MeV. The H^- ions then enter the Booster, a 475 meter circumference synchrotron accelerator, where the H^- ions pass through a thin carbon foil and become bare protons when the electrons are stripped off. In a synchrotron, magnetic fields are used to focus the particle beam and keep the beam in a circular path. A RF (radio frequency) electric field is used to accelerate the particles. The booster is the first synchrotron in the Fermi accelerator

chain. It accelerates the protons to 8 GeV in 0.033 seconds with the beam circulating 16,000 times. The 8 GeV protons then are injected into another synchrotron, the Main Injector.

The anti-proton source:

A beam of 120 GeV protons in the Main Injector is directed onto a 7 cm Nickel Target every 1.5 seconds. The collisions create many particles including anti-protons. For every million protons only about 20 anti-protons with average 8 GeV kinetic energy are produced in different directions. Those anti-protons are then focused into a beam by a Lithium lens. A pulsed magnet is used to filter out other species of particles in the beam. The anti-protons in the beam have a large spread in energy. They have to be cooled before being sent back to the Main Injector. The Debuncher, an 8 GeV synchrotron, is used to narrow the energy spread of the anti-protons. The 120 GeV protons from the Main Injector are bunched, so the anti-protons produced are also bunched. The Debuncher is also used to increase the time spread of the anti-protons and produce a continuous beam. The beam stays in the Debuncher for 1.5 seconds and is then transfered to the next 8 GeV synchrotron, the Accumulator. As the name implies, the Accumulator is used to accumulate anti-protons. In addition, in the Accumulator the anti-protons will be cooled in three dimensions by a stochastic cooling system [37]. Stochastic cooling is a beam feedback technique that measures a particle's position with a pickup and corrects the position with a kicker. When there are enough anti-protons (usually 80-200$\times 10^{10}$), the stack of anti-protons is sent into the Main Injector and preparations begin for a new store in the Tevatron.

The Main Injector and Recycler:

The Main Injector is a new 150 GeV accelerator designed to replace the old Main Ring. It can be operated in different modes and used for the anti-proton production, the fixed target experiments and collider operation. In the collider operation both protons and anti-protons in the Main Injector are accelerated to 150 GeV and injected into the Tevatron. The Recycler is a fixed 8 GeV storage ring built in the same tunnel as the

Main Injector. It is a very reliable storage ring for anti-protons with very little loss. The main purpose of the Recycler is to provide more anti-protons for the Tevatron and, thus, to increase the luminosity. At some points during the acceleration, the stack size in the Accumulator is too large and the stacking rate decreases. By removing some anti-protons to the Recycler, the Accumulator can keep a high stacking rate. At the end of each Tevatron store, the left-over anti-protons (50%-70% of inital number) can also be kept in the Recycler for the next store. So, acting as a post-Accumulator and receptacle for recycled anti-protons from previous Tevatron store, the Recycler is a crucial part for achieving high luminosity in Run II.

The Tevatron:

The Tevatron is the world's first superconducting synchrotron and currently its most powerful accelerator. It is a 1 km radius ring with about 1000 superconducting magnets. The Tevatron came into operation in 1983 and undertook a major upgrade between 1996 and 2001. When the 150 GeV protons and anti-protons are injected into the Tevatron, they are accelerated to 0.98 TeV in opposite directions. Both the protons and anti-protons are grouped into 36 bunches and each bunch contains $\sim 30 \times 10^{10}$ protons and $\sim 3 \times 10^{10}$ anti-protons, respectively. The two beams are focused by quadruple magnets and brought into collision with each other at two points around the ring. One is located at B0 where the CDF detector resides. The other is at D0 which hosts the D0 experiment. The data used in this analysis was collected by the CDF detector. In the 36 bunch mode, the two beams collide with each other every 396 ns at B0 and D0. The Luminosity formula is as follows [38]:

$$L = \frac{10^{-6} f B N_p N_{\bar{p}} (6\beta_r\gamma_r)}{2\pi\beta^*(\epsilon_p + \epsilon_{\bar{p}})} H(\sigma_l/\beta^*) \quad (10^{31} cm^{-2} sec^{-1}) \tag{3.1}$$

where:

$f = revolution\ \ frequency = 47.7KHz$
$B = number\ \ of\ \ bunches = 36$
$\beta_r\gamma_r = relativistic\ \ beta \times gamma = 1045$
$\beta^* = beta\ \ function\ \ at\ \ IR = 35cm$

$H = hourglass\ \ factor = 0.60 - 0.70$

$N_p, N_{\bar{p}} = bunch\ \ intensities\ \ (E9)$

$\epsilon_p + \epsilon_{\bar{p}} = transverse\ \ emittances\ (\pi - mm - mrad)$

$\sigma_l = bunch\ \ length\ (cm)$

Table 3.1 lists the current Tevatron parameters and goals for the year 2003 and the future Run II. The Run Ib Tevatron parameters are also provided for comparison when available. Fig 3.3 shows the chart of integrated Run IIa luminosity starting from March 05, 2001, and Fig 3.4 shows the Tevatron's peak luminosity.

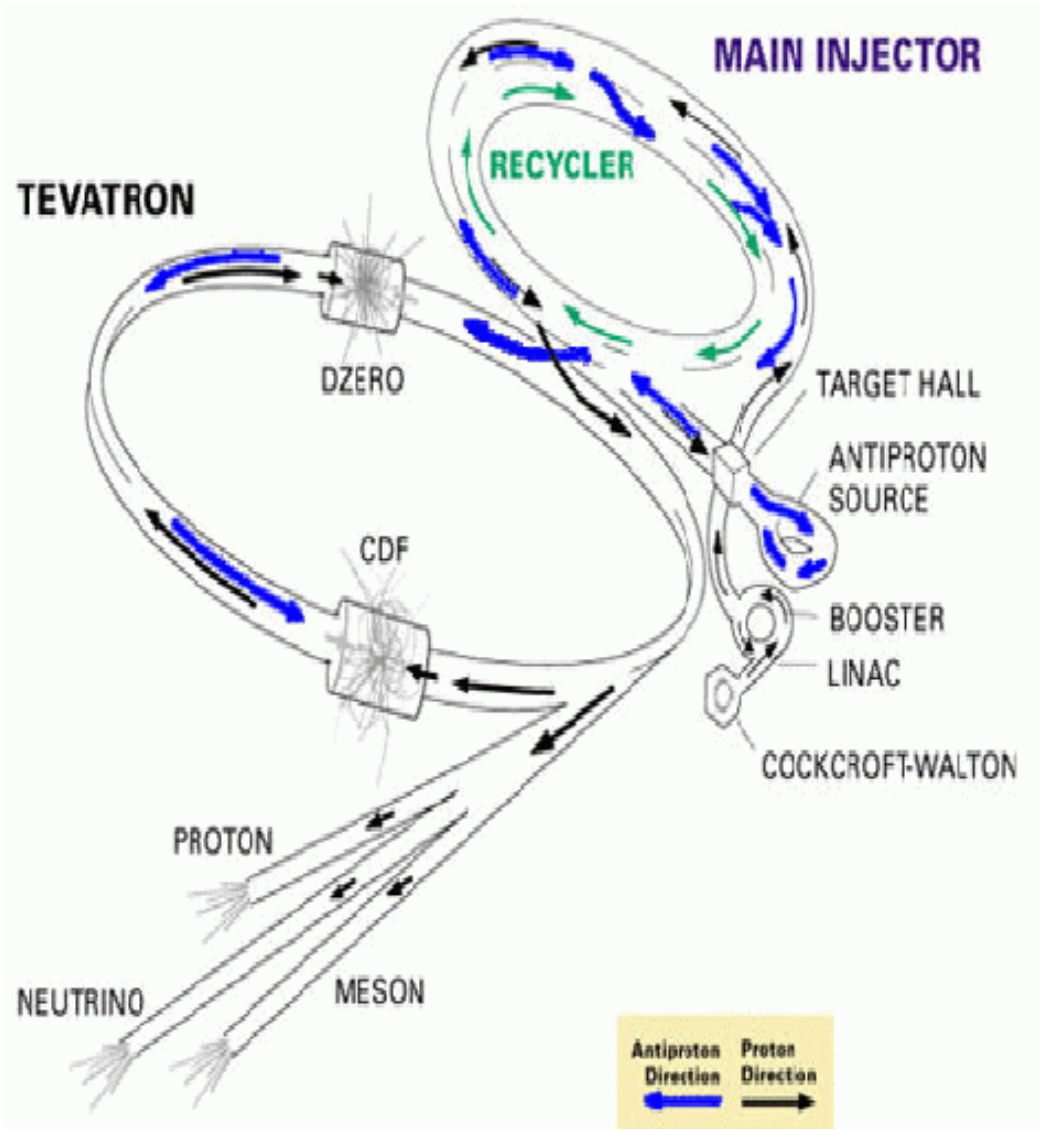

Figure 3.2: A diagram of FermiLab Accelerator chain.

parameter	Run Ib	Current performance (Feb.2003)	FY03 Goal	Run II Goal
Typical Luminosity($10^{31} cm^{-2} sec^{-1}$)	N/A	3.2e31	6.6e31	33e31
Integrate Luminosity(pb^{-1}/week)	90(total)	6.0	12.0	70.0
Protons/bunch	230e9	170e9	240e9	270e9
Pbar/bunch	55e9	22e9	31e9	135e9
proton emittance(πmm-mrad)	23	20	20	20
Pbar emittance(πmm-mrad)	13	18	15	14
Bunch length(m)	0.6	0.6	0.54	0.54
Peak Pbar production rate	N/A	11.5e10	18e10	45e10
number of bunches	6×6	36×36	36×36	36×36
$\beta^*(cm)$	35	35	35	35
Beam Energy(GeV)	900	980	980	980
Beam spacing(ns)	3500	396	396	396

Table 3.1: Current performance and Goals for Tevatron parameters. Run Ib parameters are also provided for comparison when available.

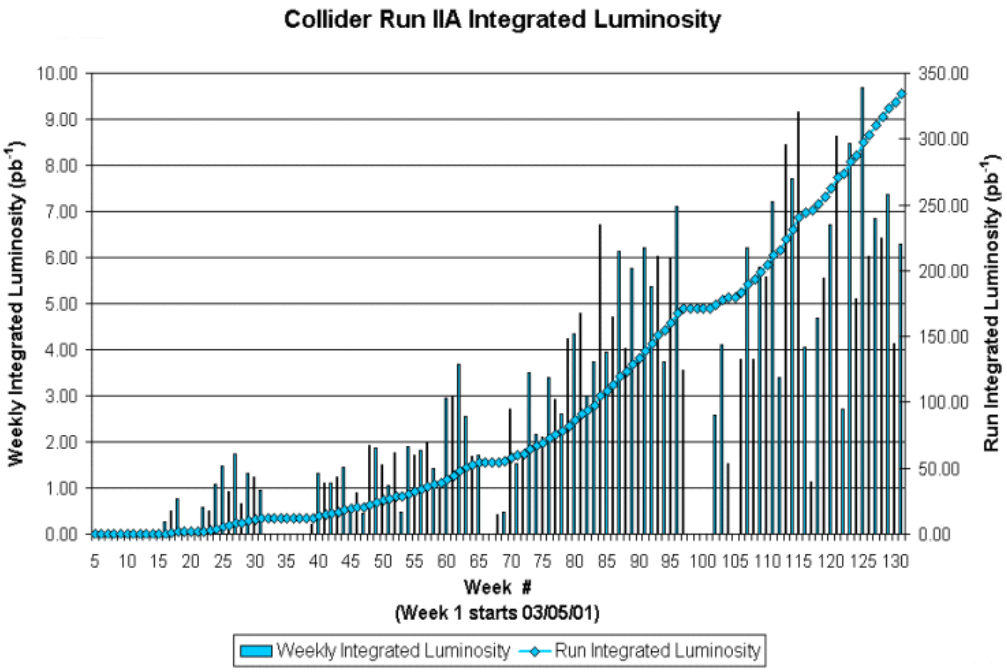

Figure 3.3: The Tevatron's integrated Luminosity from the beginning of Run II to Sept. 2003. The luminosity is plotted weekly. The vertical blue bar shows the weekly total luminosity in nb^{-1}. The diamond connected line displays the total integrated luminosity in pb^{-1}.

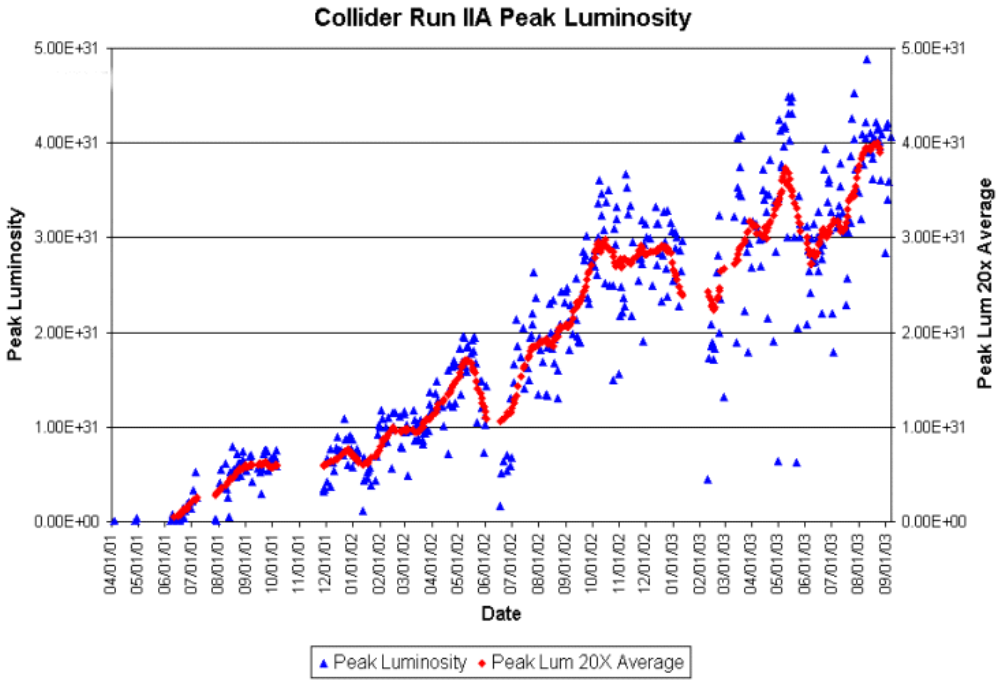

Figure 3.4: The Tevatron's peak Luminosity. The blue triangle shows the peak luminosity at beginning of each store. The red diamond displays the average of the last 20 peak values.

3.2 Collider Detector at Fermilab (CDF)

The Collider Detector at Fermilab (CDF) is a general purpose detector located at one of Tevatron's beam colliding regions. The detector is designed to identify the particles generated from proton and anti-proton collisions. The data taken from the detector are analyzed by the scientists in CDF collaboration to study all sorts of interesting physics. Along with the upgrade of FermiLab accelerators, the CDF detector also undertook a major upgrade. The new detector is called the CDF II detector. The detailed specifications of this detector can be found in the technical design report [39]

3.2.1 Detector Overview

The CDF II detector is a solenoidal detector with cylindrical and forward-backward symmetry. The origin of the detector coordinate system is at the interaction point, which is usually called the primary vertex. The z-axis is along the beamline in the direction of incoming proton, the polar angle θ is measured from the z-axis, and the azimuthal angle ϕ is measured from the Tevatron plane. Another useful quantity is pseudorapidity which is defined as $\eta = -ln(\tan\theta/2)$. The Fig 3.5 shows an elevation view of one half of the CDF II detector. The detector combines the tracking systems, calorimeter systems and muon systems as well as associated electronics and trigger systems. With all sub-systems, the CDF II detector has the abilities to reconstruct charged particles with high efficiency and measure their momentum with high precision, to identify and reconstruct e, μ leptons and photons, to reconstruct jets and measure their energy and to identify the types of particles using dE/dx and time of flight (TOF). The main parts of the detector systems used in this analysis are the tracking systems.

3.2.2 Tracking Systems

The efficient and precise tracking systems are the most crucial part of the CDF II detector. A schematic drawing of the tracking systems is shown in Fig 3.6. All of

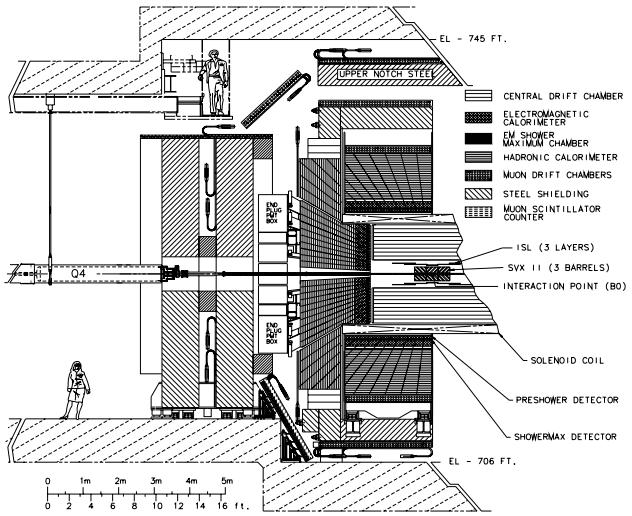

Figure 3.5: An elevation view of CDF II detector.

the tracking systems are located inside the superconducting solenoid, which provides an axial magnetic field of 1.5 Tesla over a volume 2.8 meters in diameter and 3.5 meters long. The CDF tracking systems consist of an inner silicon tracker outside the beam pipe and a Central Outer Tracker (COT) outside the silicon detector. Between the COT and the solenoid, a time-of-flight (TOF) detector was added to provide additional particle identification information.

When a charged particle passes through a uniform magnetic field, the trajectory of the particle, which is called a track, is bent to form a helix. The particle's charge and momentum can be determined from the curvature of the helix. The tracking systems are used to reconstruct the track trajectories. In CDF five parameters are used to describe a track: d_0 (impact parameter), C (curvature), ϕ_0, z_0 and λ ($\lambda = cot\theta$).

3.2.2.1 Inner Tracker: L00 + SVX II + ISL

The CDF silicon tracking system contains three mechanically separate sub-detectors: L00, SVXII and ISL. Fig 3.7 shows both the r-ϕ view and r-z view of the silicon detectors. The silicon detectors are high precision microstrip detectors which can provide information on both the r-ϕ and z views. The silicon tracking system has 7 silicon lay-

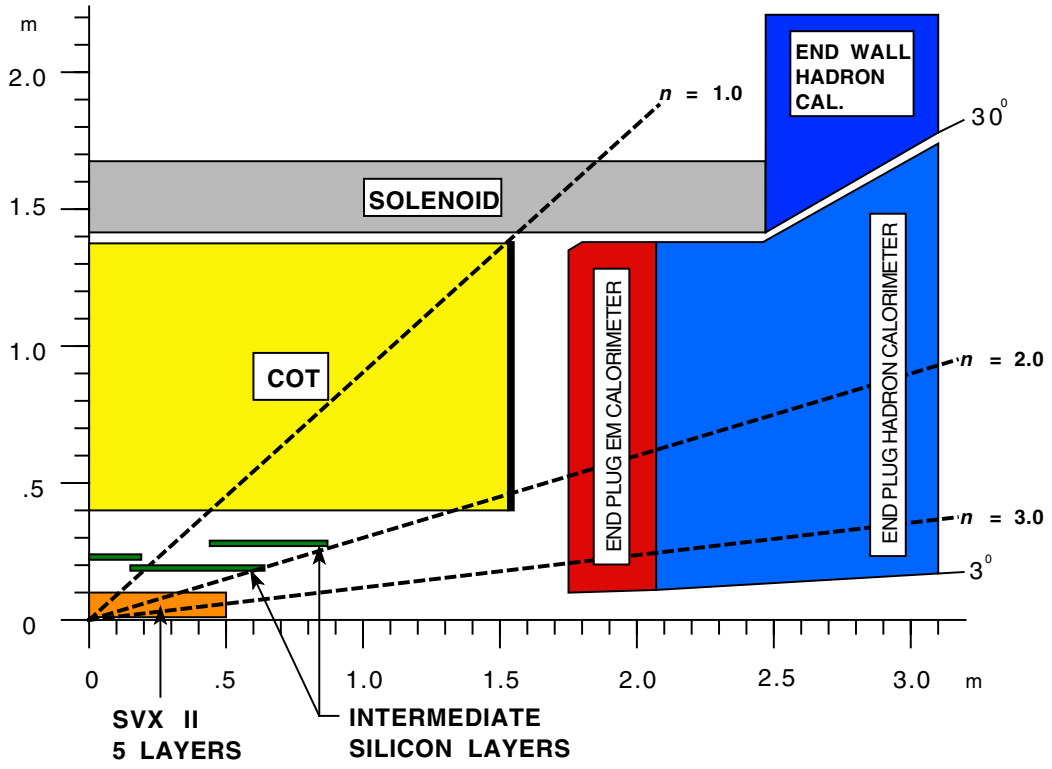

Figure 3.6: A Longitudinal View of the CDF II Tracking System.

ers in the central region ($|\eta|$ <1) and 8 silicon layers in the forward region (1< $|\eta|$ <2), with the radii spanning from 1.35 cm to 28.9 cm and the lengths ranging from 90 cm to 200 cm.

Layer 00 (L00)

L00 is a single sided and single layer radiation tolerant silicon strip detector. It provides full azimuthal coverage with r-ϕ information. Fig 3.8 shows the end view of L00. L00 lies inside the SVXII layers. The inner sensors have 128 strips and are located at radii of 1.35 cm. The outer sensors have 256 strips and are locate at radii of 1.62 cm. The readout pitch is 25 μm and 50 μm for the inner and outer sensors, respectively. The sensors are mounted on a carbon-fiber support structure just outside the beam pipe. There are 12 sensors along the z direction for a total

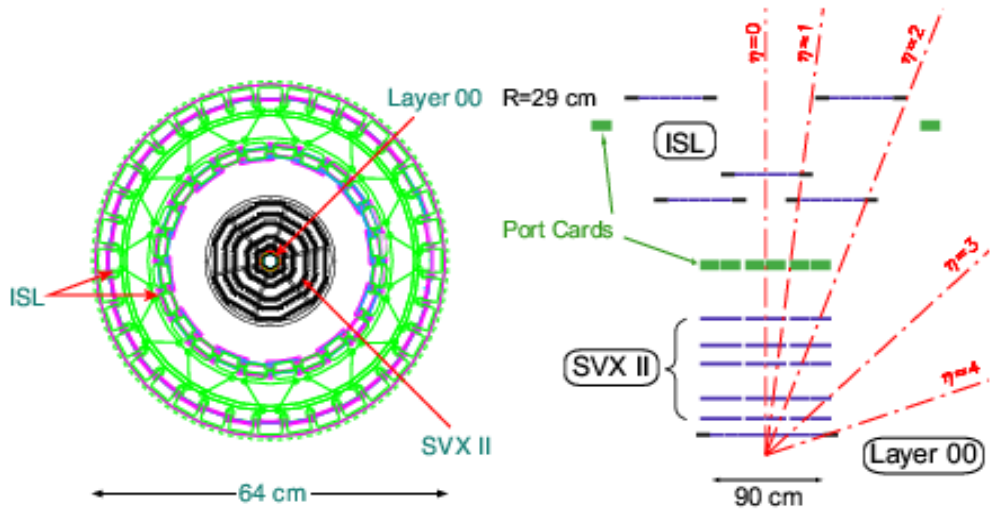

Figure 3.7: Both r-ϕ view and r-z view of the silicon tracking systems. Note in the r-z view, the z direction is compressed.

length of 94 cm. The total number of readout channels for L00 is 13,824. Placed at a smaller radius and with less material than SVXII, L00 can enhance the track's impact parameter (d_0) resolution which is essential for many physics analysis, for example the B_s mixing measurement. Another reason for adding L00 to the silicon tracking system is that the L00 uses radiation hard silicon material which can outlive the inner SVXII layers under the severe radiation environment near the interaction point. The L00 began commissioning in February, 2002. The study of the alignment is still incomplete.

Silicon Vertex Detector (SVXII)

The Silicon Vertex Detector is a core part of the CDF tracking system. Johns Hopkins University physicists played major roles in its design, construction, testing, installation and utilization. It is built in three cylindrical barrels with a total length of 96 cm. Each barrel supports five layers of double sided silicon strip detectors between radii of 2.4 cm and 10.7 cm, as shown in Fig 3.9. Each barrel is divided into 12 wedges in azimuth. The silicon sensors are supported by the low-mass substrate structures, called "ladders". Twelve ladders make a full circle for each layer. Three of the layers

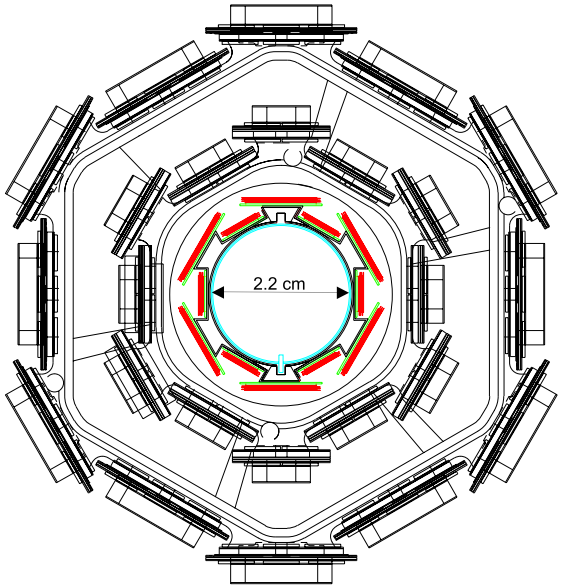

Figure 3.8: An end view of L00 and the inner sensors and outer sensors of L00.

(the first, second and fourth layers) have an $r-\phi$ measurement on one side and 90^o stereo measurement on the other side. The other two layers (the third and fifth layers) have small angle stereo (1.2^o) on the other side. On the ϕ side, the sensors have 60-65 μm pitch strips running axially. On the 90^o stereo side the strips run perpendicular to the axial strips with pitch 125.5 or 141 μm. On the small angle stereo side the strips are tilted by a small angle (1.2^o) with the pitch 60 or 65 μm depending on layers. The total number of readout channels is 405,504. The geometric parameters are listed in Table 3.2. The parameters from the RunI version of the silicon vertex detector are also provided for comparison. The SVXII is designed to provide precise 3D secondary vertex information. The information from the SVXII is sent to the Level-2 trigger where it is used to select events with displaced vertices.

Intermediate Silicon Layer (ISL)

The Intermediate Silicon Layer (ISL) is located between SVXII and Central Outer Tracker. It is double sided silicon with 55 μm strip pitch on the axial side and 73 μm strip pitch on the small angle stereo (1.2^o) side. Every other strip is read out to

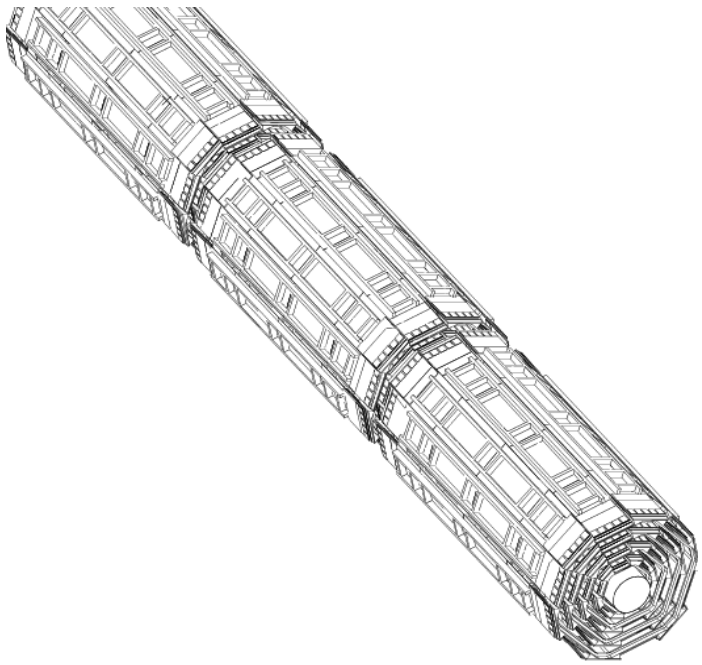

Figure 3.9: Three barrels of SVXII.

reduce the total number of channels to 268,800. In the central region, a single ISL layer is placed at a radius of 22 cm, which helps to extrapolate the COT tracks into the silicon. In the forward region ($1< |\eta| <2$), two silicon layers are placed at radii of 20 cm and 28 cm. This increases the tracking acceptance in the region the COT doesn't cover efficiently. The total length of the ISL is 190 cm. The silicon sensors are mounted on "ladders" similar to the SVXII. The ISL utilization is still under study.

SVX II Readout and DAQ System

When a charged particle passes through a silicon layer of SVX II, electron-hole pairs are created and the electrons drift to the readout strips under biased voltage. An on-board radiation hardened CMOS integrated circuit, called the SVX3 chip, is used to read out the silicon signals. Each chip has 128 channels and can be divided into an analog and a digital section. For each channel, the analog section contains an input amplifier, a low noise integrator and a 46 cell analog pipeline with 4 buffer cells. The digital section contains an 8 bit ADC Wilkinson comparator, a Dynamical Pedestal

Subtractions (DPS) and a differential output current driver. The SVX3 chips are mounted on an electrical hybrid on the surface of the silicon detectors. The chips from each wedge are read out over high density interconnects (HDI). The HDIs are connected to a port card (PC). At the port card, the digitized signals are converted from electrical to optical signals by dense optical interface modules (DOIM). Each DOIM drives a 10 m long ribbon of optical fibers at 53 MHz to VME boards located on the side of the CDF detector. This highly parallel readout system enables the entire detector (totaling ∼400k channels) to be read out in 10 μs. The VME crates on the west side of the CDF detector house the fiber interface board (FIB). Each port card is controlled by the FIB based on the commands sent from the silicon readout controller (SRC) located in the CDF counting room. A sketch of the SVXII DAQ system is shown in Fig 3.10.

The expected momentum resolution for SVXII is $\delta p_T/p_T^2 \simeq 7\%(GeV/c)^{-1}$. The impact parameter resolution is $\delta d_0 = 50\mu m$.

Detector Parameter	SVX'	SVXII
Readout coordinates	r-phi	r-phi; r-z
Number of barrels	2	3
Total length (cm)	51	87
Ladder/barrel length (cm)	25.5	29
Length readout (r-phi) (cm)	25.5	14.5
Number of layers per barrel	4	5
Number of phi-sectors per barrel	12	12
Radius innermost layer (cm)	3.0	2.45
Radius outermost layer (cm)	7.8	10.6
r-phi pitch (inner to outer) (mm)	60; 60; 60; 55	60; 62; 60; 60; 65
r-z readout angle (deg)		90; 90; +1.2; 90; -1.2
r-z pitch (mm)		141; 125.5; 60; 141; 65
Number of r-phi chips/ladder	2; 3; 4; 6	4; 6; 10; 12; 14
Number of r-z chips/ladder		4; 6; 10; 8; 14
Number of r-phi channels	46,080	211,968
Number of r-z channels		193,536

Table 3.2: The parameters of the SVX II detector geometry. The parameters of the silicon vertex detector in RunIb (SVX') are also listed for comparison.

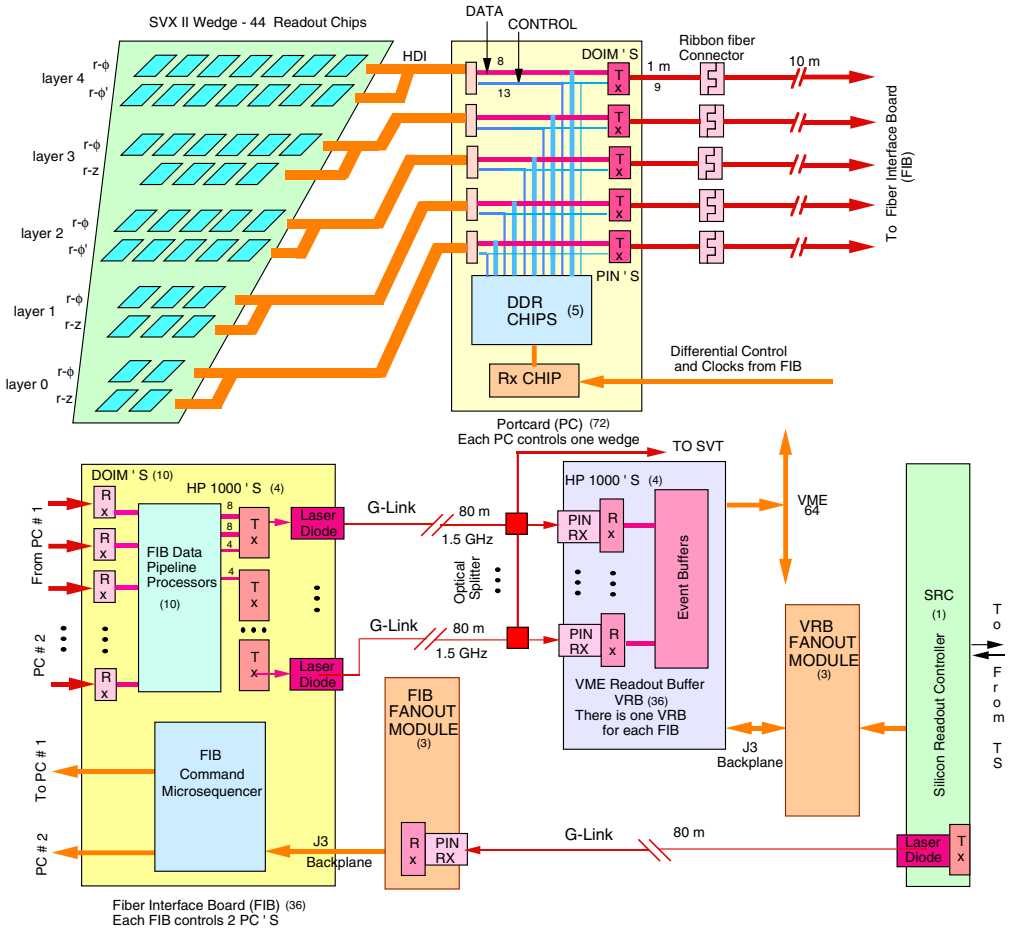

Figure 3.10: Schematic of the SVX II data acquisition system.

3.2.2.2 Central Outer Tracker: COT

The Central Outer Tracker (COT) is an open cell cylindrical drift chamber located between radii of 40 and 132 cm from the beam pipe and spans 310 cm in the z (axial) direction. The COT is segmented into 8 super layers (4 axial layers and 4 stereo layers), as shown from the end plate section in the Fig 3.11. Each superlayer is divided in ϕ into "super cells". A super cell consists of one wire plane and one field plane on either side. The slots for the wire planes and field planes are also shown in the end plate layout (Fig 3.11). In the wire plane sense wires alternate with potential wires as shown in the Fig 3.12. There are 12 sense wires, 13 potential wires and 4 field shaper wires in each cell. The wires are made of 40 μm diameter gold-plated tungsten. The sense wires are used for read out, the potential wires are used to provide the electric field and the field shaper wires are used to adjust the electric field due to the taper of the cell with decreasing radius. The field plane is 6.35 μm thick Mylar with vapor-deposited gold on both sides. The superlayer is titled by 35^o with respect to the radial direction because the electrons drift with a Lorentz angle of $\sim 35^o$ in the magnetic field. The super layers alternate between axial and stereo layers. In the axial layers, the wire planes and field planes are parallel to each other along the z direction and provide the precise $r-\phi$ information. In the stereo layers, both planes have a stereo angle of $\pm 2^o$ with the z direction, which provides the $r-z$ information although it is less accurate than $r-\phi$ information.

The COT is currently filled with a gas mixture of Argon/Ethane (50:50) when running on 36 bunches mode. A fast drift velocity gas mixture such as Argon/Ethane/CF_4 (50:35:15) can be used later if the accelerator operates in a mode with more bunches. When a charged particle passes through the COT, the electrons from ionized gas drift toward the sense wires due to the electric field. The electrons will cause more gas to be ionized and will cause an avalanche next the wire. The pulse caused by the movement of electrons and avalanche will be collected by the sense wire. An Amplifier/Shaper/Discriminator with Charge encoding (ASDQ) chip was developed to measure the charge collection and signal profile for the hits. The width of the discriminator output pulse indicates the total charge deposited on the sense wire. It

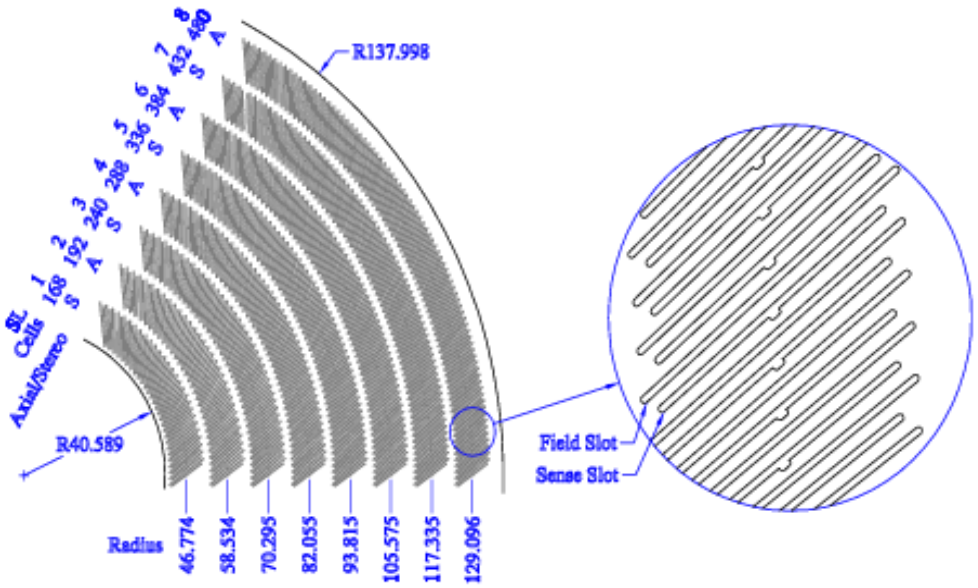

Figure 3.11: A section of the COT end-plate. The radius of each layer and number of cells in each layers are shown. The slots for the sense plane and field plane are also shown.

can be used to calculate dE/dx. A detailed description of the COT can be found in the reference [40]. The COT can find the tracks within the region $|\eta|$ <1 with the minimum p_t = 400 MeV/c. The hit resolution of the COT is about 180 μm, the momentum resolution is $\delta p_T/p_T^2 \simeq 0.3\%(GeV/c)^{-1}$, the impact parameter resolution for the COT alone is about 600 μm and the z_0 resolution is about 5 mm.

3.2.3 Calorimeter Systems

The CDF II calorimeter systems are located outside the solenoid and cover 2π in azimuth and the region $|\eta| < 3.64$ in pseudorapidity. The calorimeter systems are used to measure electron and photon energies, jet energies and net transverse energy flow. The calorimeter systems are separated into two independent physical sections: the Central Calorimeters and the Plug Calorimeters. The central detectors are the same as Run I except for new electronics. The Plug detectors are brand new and replace the old gas calorimeter in Run I. Each section consists of an Electromagnetic section

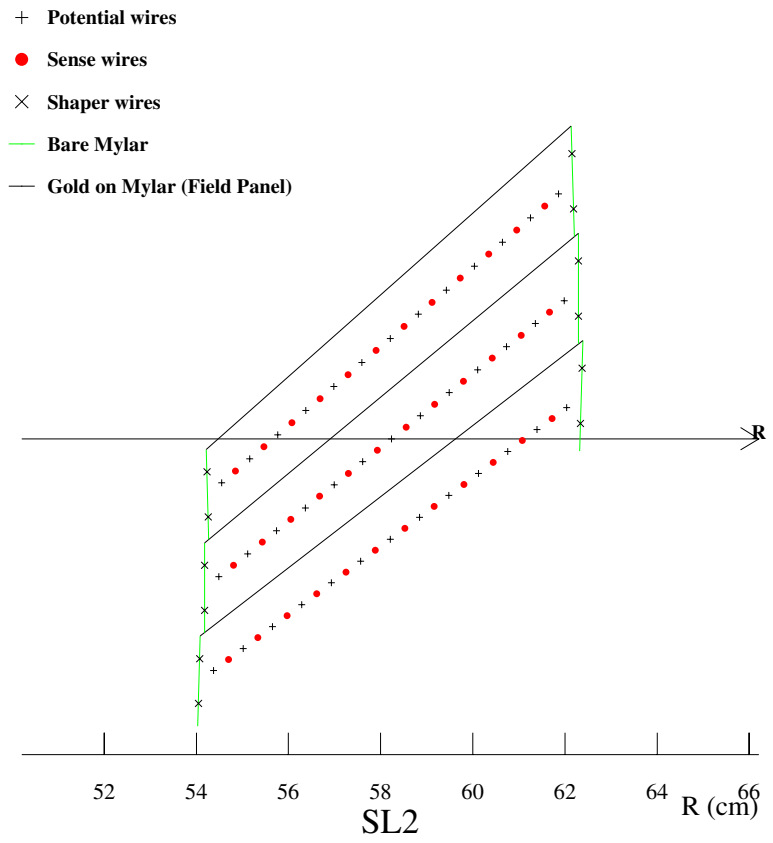

Figure 3.12: A $r - \phi$ view of three super cells in the COT.

(CEM for central region, PEM for plug region) and a hadronic section (CHA for central region, PHA for plug region). There is also an end-wall hadronic calorimeter (WHA) which covers the gap between the CHA and PHA. The EM Calorimeter is a lead/scintillator sampling device and the Hadronic Calorimeter is an iron/scintillator sampling device. In both the EM and HAD sections the active elements are the scintillator tiles read out by wavelength shifting (WLS) fibers embedded in the scintillator. The calorimeters are segmented in azimuth and in pseudorapidity to form a projective tower geometry. Two shower maximum detectors (CES and PES) are embedded in the central and plug EM calorimeters near the shower maximum to provide the precise position of the showers. There are also two preshower detectors (CPR and

	CEM	CHA	WHA	PEM	PHA
Coverage in ($\|\eta\|$)	<1.1	<0.9	$\|\eta\| > 0.7$ $\|\eta\| < 1.3$	$\|\eta\| > 1.1$ $\|\eta\| < 3.64$	$\|\eta\| > 1.2$ $\|\eta\| < 3.64$
Energy Resolution	$14\%/\sqrt{E_T}$ $\oplus 2\%$	$50\%/\sqrt{E_T}$ $\oplus 2\%$	$75\%/\sqrt{E}$ $\oplus 4\%$	$16\%/\sqrt{E}$ $\oplus 1\%$	$80\%/\sqrt{E}$ $\oplus 5\%$
Thickness	$19X_0, 1\lambda$	4.5λ	4.5λ	$21X_0, 1\lambda$	7λ
Segmentation					
($\|\eta\|$ range,	<1.1		1.1-1.8	1.8-2.1	2.1-3.6
$\Delta\eta \times \Delta\phi$	0.1×15^o		0.1×7.5^o	0.16×7.5^o	$\sim 0.4 \times 15^o$

Table 3.3: Design parameters of CDF II calorimeters, X_0 is the radiation length , λ is the hadronic interaction length, $\oplus$ means that the constant term in the energy resolution is added in quadrature.

PPR) placed between the front of the EM calorimeters and magnetic coil to provide additional information to separate photons, electrons and hadrons. In Table 3.3, the design parameters of the calorimeters are listed, including the tower segmentations, coverage ranges of different sub-detectors, energy resolutions, etc. Calorimeter information can be used not only for direct photon and lepton measurement, but also for an analysis which has photon and lepton backgrounds. In the data set used in this analysis the statistics and cleanliness were such that these backgrounds were not significant and the calorimeter information was not used.

3.2.4 Muon Systems

CDF II uses four similar systems of scintillators and proportional chambers to detect muons over the region $|\eta| \leq 2.0$. Geometric and engineering concerns led to

the four logical system, but they are all functionally similar. Fig 3.13 shows a 3-D CDF II detector, where the four muon systems are indicated with their coverage in pseudorapidity.

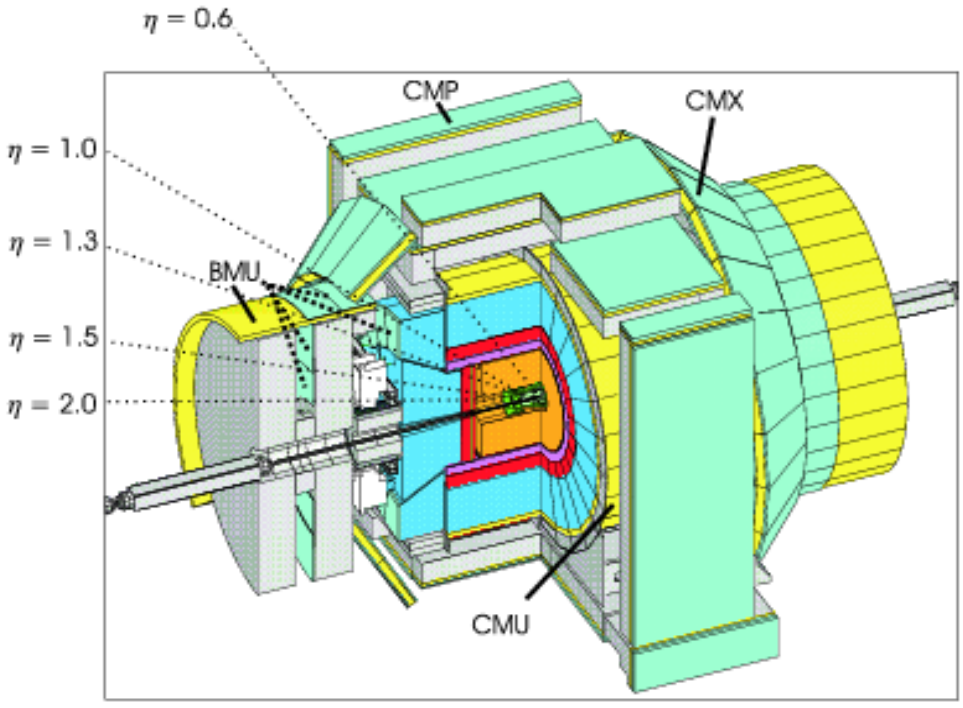

Figure 3.13: A 3-D View of the CDF II detector with the muon chambers and their coverage in pseudorapidity indicated.

- **Central MUon Detector (CMU)** The Central Muon Detector covers $|\eta| < 0.6$, and is embedded in the central calorimeter wedges at their outer radius. It's the oldest muon detector in CDF.

- **Central Muon uPgrade (CMP)** The Central Muon Upgrade Detector covers $|\eta| < 0.6$. It provides confirmation for CMU tracks but with reduced non-muon (hadronic) background. It consists of 4 layers of single-wire drift cells installed outside of 2 feet of additional steel.

- **Central Muon Extension (CMX)** The central muon extension consists of conical sections of drift tubes (CMX) and scintillation counters (CSX), located

at each end of the central detectors. It covers $0.6 < |\eta| < 1.0$.

- **Intermediate MUon system (IMU)** The intermediate muon system consists of the Barrel Muon Chamber (BMU), Barrel Scintillator Upgrade (BSU) and Toroid Scintillator Upgrade (TSU). It is designed to trigger on muons with $|\eta| < 1.5$ and to identify offline muons with $|\eta| \leq 2.0$.

3.2.5 Trigger systems

In hadron collider experiments the trigger system plays an important role to select the most interesting physics events and discard the rest of the data, because the collision rate is much higher than the rate at which data can be written to the permanent storage (e.g. tape). In Run II, the collision rate is 2.5 MHz, which corresponds to the 396 nsec beam bunch crossing rate, while the speed of tape writing is about 50 Hz. The CDF Front-End electronics, DAQ and trigger systems must meet this upgraded new accelerator conditions. The increased instantaneous luminosity requires a much faster data transfer rate. The reduced separation between beam bunches means more collisions at the same time interval and requires a faster decision time for the trigger systems. The CDF has a three level architecture of trigger systems with each level providing enough rate reduction to allow the next level to have enough time to process its events and finally make the event rate reach below 50 Hz. The block diagram of the Run II trigger systems is shown in Fig 3.14.

The functional block diagram of the CDF II data flow is shown in Fig. 3.15. All data from the detectors go into the fully pipelined front-end electronics with on-board buffering for 42 beam crossings. The pipelined electronics allow the Level-1 trigger to have at least 5.5μsec decision time at a 132 or 396 nsec bunch crossing rate. The data from the calorimeters, the central tracking chamber and the muon detectors are sent to the Level-1 trigger system, which determines if the events are interesting enough to be sent to next level trigger system. When the data are accepted by the Level-1 trigger, the data on the front-end boards are transferred to the Level-2 local buffers. The Level-2 buffers can hold as many as four events. The Level-2 trigger system makes the decision in about 20 μsec as to whether the event should go to the next

trigger level or be discarded. The selected data in the Level-2 buffers are collected into DAQ buffers and then sent to a Level-3 CPU node, where the data from different sub-detectors are assembled into a complete event. If the event is selected by the Level-3 trigger system, it will written out to the permanent storage.

Level-1 Trigger

The Level-1 trigger uses custom designed electronics to find physics objects based on the information from calorimeters, COT and muon detectors and makes a decision based on simply counting these objects (e.g. two 1.5 GeV/c P_T tracks or one 8 GeV electron). The Level-1 electronics consists of three parallel synchronous processing streams which serve as the inputs of the single Global Level-1 decision unit as shown in Fig 3.14. Following are three streams:

- **XFT + XTRP + L1 Track**: XFT (the eXtrmemely Fast Tracker) is an online parallel, pipelined track processor to identify high-momentum charged tracks. XFT gets the hit data from 4 axial COT layers and finds the tracks of $p_T >$ 1.5 GeV/c with 96% efficiency. Then the Extrapolation Unit (XTRP) receives tracks from the XFT and distributes the tracks or the information derived from the tracks to Level-1 and Level-2 sub-trigger systems.

- **Level 1 calorimeter Trigger (L1CAL)** The purpose of Level-1 calorimeter Trigger is to identify electrons, photons, jets, total event transverse energy ($\sum E_T$) and missing transverse energy ($\not\!\!E_T$). L1CAL combines the information from calorimeters and XTRP track matching information and sends it to the Level-1 trigger decision unit.

- **Level 1 Muon Trigger (L1 MUON)** The Level-1 Muon trigger gets the muon information from the muon detectors and the track matching information from XTRP, and then provides single and dimuon objects for the Level-1 trigger decision.

Different triggers can be formed using simple ANDs and ORs of objects from the above three streams. All elements of the Level-1 trigger use the same 132 nsec synchronized

clock. Global Level-1 makes its decision within 132 nsec. The data used in this analysis was taken in the 36 bunch mode (396 nsec). The trigger is clocked, however, every 132 nsec with the two intermediate clock cycles rejected automatically. The Level-1 accept rate is about 35 KHz.

Level-2 Trigger

The Level-2 trigger uses several asynchronous subsystems to provide data for the programmable Global Level-2 processors, which will decide if any Level-2 triggers are satisfied. After the event is accepted by the Level-1 trigger, the event is written into one of four Level-2 buffers. If all four buffers are full, the buffers can not be used for additional Level-1 accepts. Dead time will then occur. To keep the dead time at an acceptable level, the Level-2 processing time is set to about 20 μsec and pipelined in two stages each taking approximately 10 μsec. The first stage of the pipeline is building the event, which includes collecting data from Level-1 trigger systems (XFT and L1MUON) and from the shower maximum detector (XCES), processing calorimeter data in a hardware cluster finder (L2CAL) and processing silicon detector data in a hardware track finder (SVT). All information output from the above steps is sent into the memory of Level-2 processors. This stage is clearly shown in the Fig 3.14. Then the second stage of the pipeline examines the data and decides if any Level-2 triggers are satisfied. The final Level-2 accept rate is about 300 Hz.

- **Silicon Vertex Tracker (SVT)** The ability to use the impact parameter of tracks in the trigger to detect secondary vertices can substantially increase the physics reach of a hadron collider experiment. Studies of B hadron decays like this analysis benefit greatly by this ability, because the B hadrons usually travel a few millimeters before decaying and the tracks from B hadron decays usually have large impact parameters. The Online Silicon Vertex Tracker (SVT) is a new CDF II Level-2 trigger processor designed to reconstruct 2-D SVX II tracks with high speed and accuracy [41, 42]. With the precise measurement of impact parameters by SVT, the Run II trigger can select potential B hadron events which typically show displaced secondary vertex. The SVT has only about

$\sim$20 μsec to perform this task, so the whole design is concentrated on speedy operations. To accomplish this, the SVT is organized as 12 identical sectors running in parallel. Each sector processes the data from only one SVX II wedge. In addition, the SVT only reconstructs the tracks in the $r-\phi$ plane and only with $p_t > 2.0$ GeV/c. Fig 3.16 shows the architecture and data flow of the SVT trigger. The main function blocks of each SVT sector are the Hit Finders, the Associative Memory System, the Hit Buffer and the Track Fitter. The tracking process is performed in two steps: pattern recognition and track fitting. When the event is accepted by the Level-1 trigger, the digitized SVX data are sent to the Hit Finder where the hit positions are calculated. The hits found by the Hit Finder and the COT tracks from the XFT are fed to the Associative Memory system and to the Hit Buffer. The Associative Memory finds the legitimate track trajectory (roads) by searching all the coincidences of 4 silicon hits and XFT tracks and comparing these with precalculated patterns. The output of the patterns are also sent to the Hit Buffer. Finally, the Track Fitter checks all the hit combinations in each road and calculates track parameters with a precision comparable to the offline analysis.

Event Builder and Level-3 Trigger

Because the Level-1 and Level-2 systems have to make their decisions at very high rates, their algorithms only use small predefined pieces of event data to make their selections. Those event pieces are stored in the buffers of Front-End crates when Level-1 and Level-2 are making their decisions. After a Level-2 decision is made, the Event Builder fetches the data fragments from the passed event and assembles them into one data block with an appropriate data structure for analysis. The assembling process has two stages. First, event pieces from Front-End crates are concentrated in 15 EVB crates. Then the event fragments from EVB crates are sent to one of 16 Level-3 subfarms where the event is finally assembled and processed.

A Level-3 subfarm is an independent logical unit of the Level-3 farm. Each subfarm consists of one converter node which serves as the subfarm input and control

center and 14 to 18 processor nodes which are running on a set of software packages (e.g Control code, Reformatter and L3 filter code). Every two subfarms share one output node. Each processor node is a dual Pentium III Linux PC. It takes about a second for one Linux PC to make a trigger decision on one event. The 16 subfarms have about 250 such PCs to meet the required processing rate. Within the processor node the Control code receives raw events from the Converter node, then the Reformatter code rearranges the event data to offline (Trybos) format, performs some consistency checks and discards corrupted events. An event which has passed the Reformatter is sent by Control code to the Level3 Filter code which runs an offline-type reconstruction and makes Level-3 trigger decisions and discards failed events. It also transforms passed events to Flat Root format. Finally, the Control code sends the events which passed the Level-3 trigger to the output node, and the output node sends the events to the Consumer Server Logger(CSL). The CSL writes the event data to disk and distributes a small fraction of the events to the Consumer monitoring programs.

The Level-3 algorithms take advantage of the full detector information and improve the resolutions which are not available to the lower trigger levels. The Level-3 input rate is $\sim$300 Hz and output rate is $\sim$ 75 Hz.

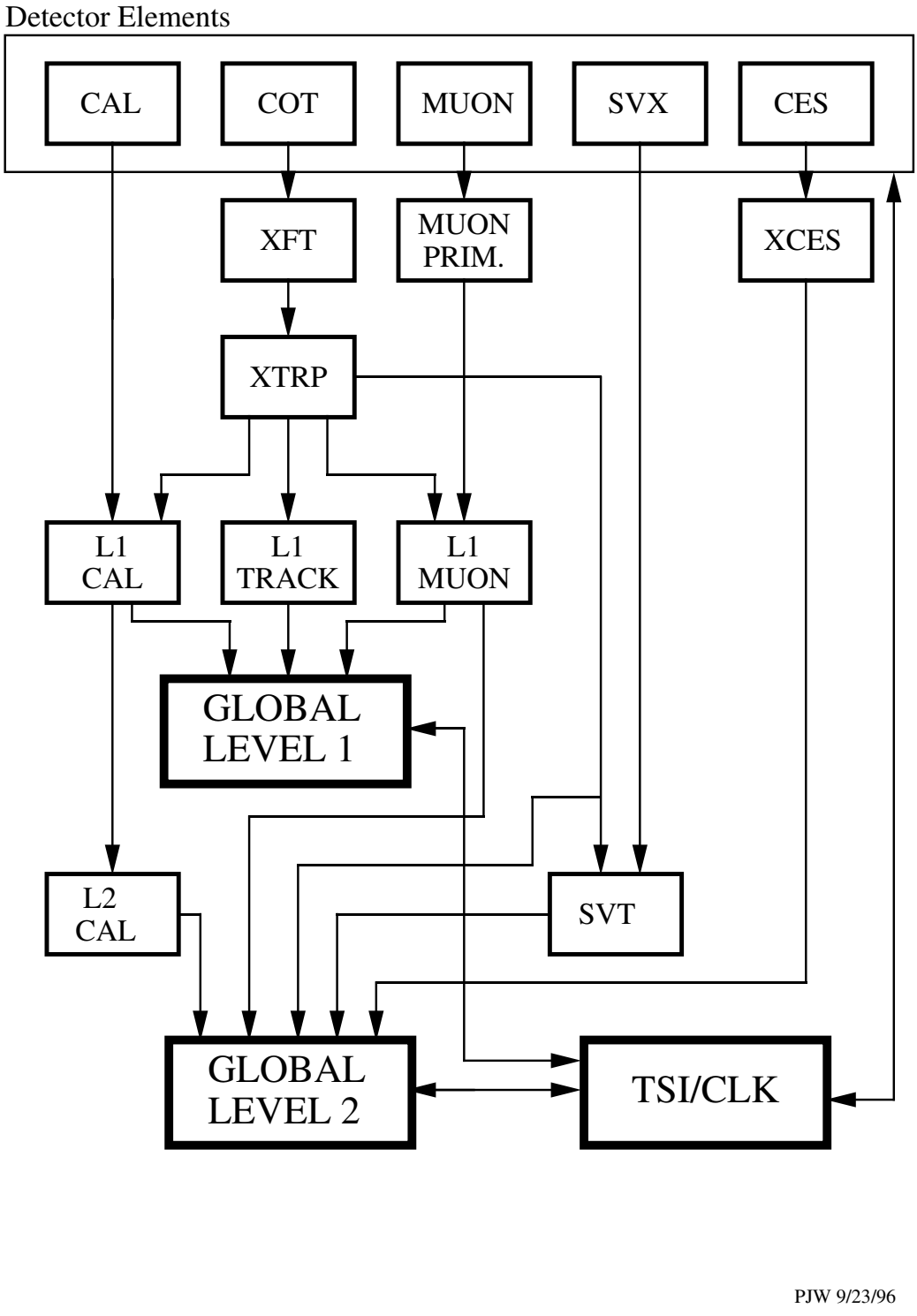

Figure 3.14: The CDF II readout functional block diagram.

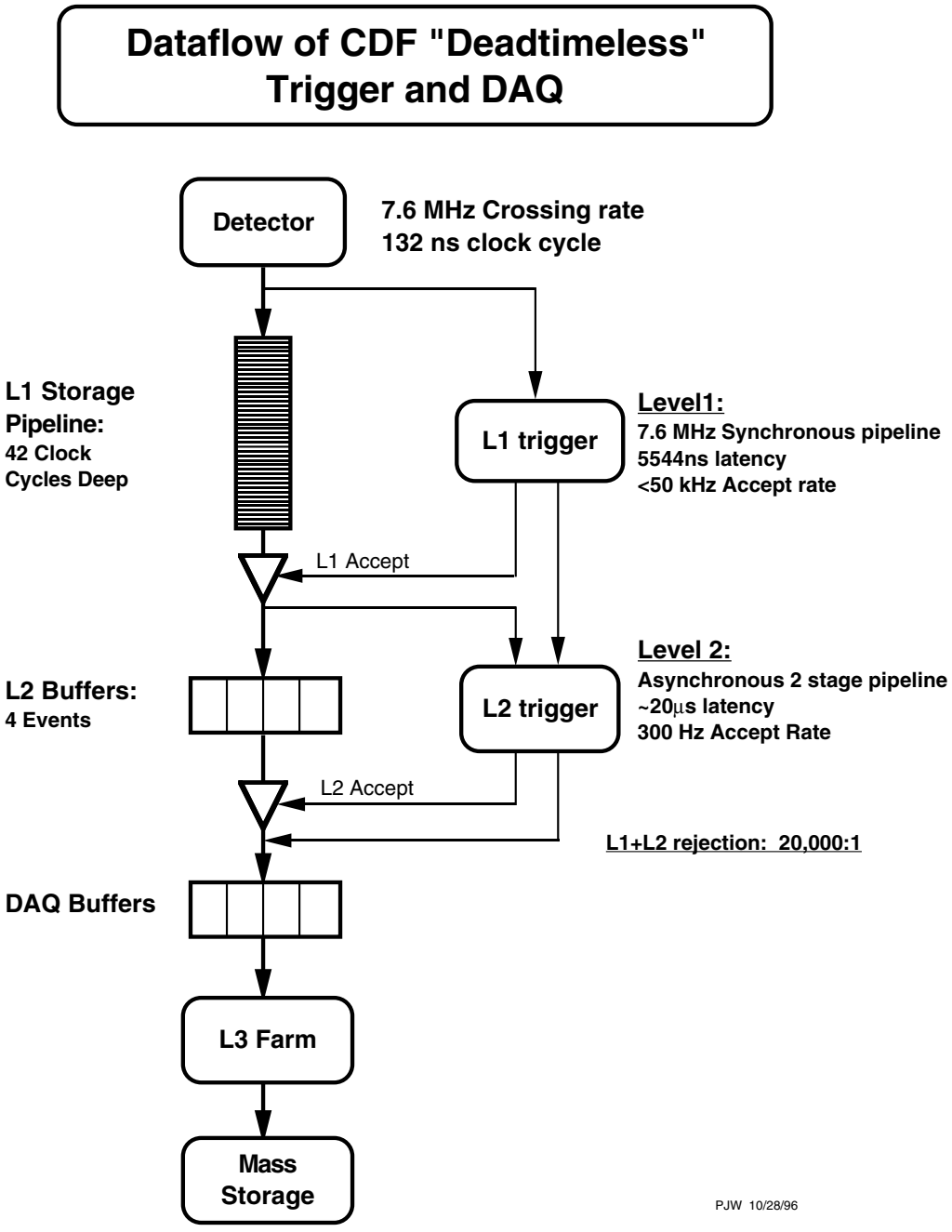

Figure 3.15: The block diagram of CDF II data flow

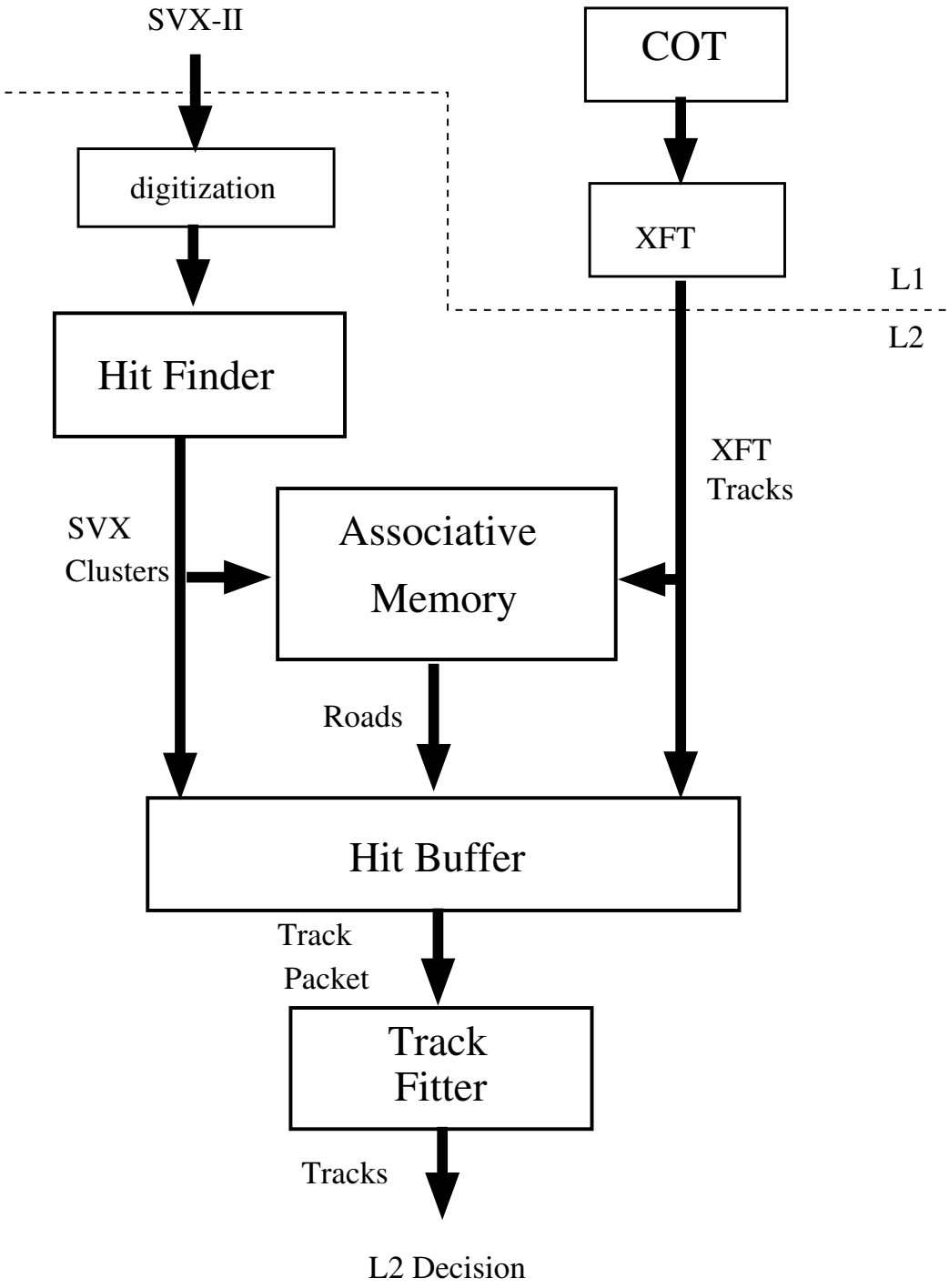

Figure 3.16: Architecture and data flow of the SVT trigger.

Chapter 4

Data Sample and Event Selection

4.1 Hadronic Data Sample

After passing the Level 3 selection, the raw data are processed on a PC farm [43]using CDF Production software. In the process the high level objects like tracks, electrons, muons and jets are reconstructed. The events with those reconstructed objects are separated into different data sets based on the triggers passed by the events.

The dataset, hbot0h, is used in this analysis. This dataset is from a specific trigger, named Two-Track Hadronic Trigger. This trigger is designed to collect data with enhanced charm and bottom hadron content. The proposal of this trigger was made long before Run II started and had been studied in detail using Run I data and signal Monte Carlos [44, 45]. There are three scenarios proposed, commonly called scenarios "A", "B", "C". For example, the scenario "A" trigger requires two opposite charged tracks with 2.0 GeV/c minimum p_T for each track, 5.5 GeV/c minimum sum p_T for the track pairs, the track impact parameter d_0 should satisfy 120 $\mu m < |d_0| < 1$ mm, and the track ϕ_0 difference should satisfy $2^o < \Delta\phi < 90^o$. The difference between these three scenarios is the values of minimum p_T requirement for the individual tracks and the minimum sum p_T requirement for the track pairs. In the dataset hbot0h, events are from three different trigger paths (B_CHARM, B_CHARM_LOWPT, B_CHARM_HIGHPT). The trigger path B_CHARM is closest

to the scenario "A". CDF has a three level trigger system. Each trigger path is sequence of well defined selection criteria utilized by the Level 1-3 trigger. Usually, the lower level triggers are more stable and higher level triggers change more frequently. In the dataset hbot0h, the trigger cuts in three trigger paths have all changed slightly from time to time. Only the typical definitions of those trigger paths are given in the following. The details of the time dependent changes can be found in the reference [46].

4.1.1 The Trigger Paths

B_CHARM Trigger Path

The Level-1 trigger decisions in the B_CHARM trigger path are made on XFT tracks. The selection cuts are:

- two XFT tracks
- 4 XFT layers per track
- XFT p_T >2.04 GeV/c for both tracks
- two tracks have opposite charge
- $0 < \Delta\phi < 135^o$
- scalar sum p_T of two tracks > 5.5 GeV/c

The Level-2 trigger decisions in the B_CHARM trigger path are made on SVT tracks. The selection cuts are:

- two SVT tracks
- SVT $\chi^2 < 25$
- SVT p_T >2.0 GeV/c for both tracks
- two tracks have opposite charge

- $2^o < \Delta\phi < 90^o$
- 120 $\mu m < |d_0| < 1$ mm
- L_{xy} >200 μm
- $\sum p_T$ of two tracks > 5.5 GeV/c

The Level-3 executable matches the SVT tracks to COT tracks. The impact parameter d_0 is found from SVT tracks. The other four track parameters are from COT tracks. Level-3 trigger has following requirements for an event to pass:

- at least two tracks in the event
- p_T >2.0 GeV/c for both tracks
- 120 $\mu m < |d_0| < 1$ mm
- L_{xy} >200 μm
- $|\Delta z_0| < 5.0$ cm
- $|\eta|$ <1.2

B_CHARM_LOWPT Trigger Path

The B_CHARM_LOWPT trigger path picks events with lower momentum tracks and uses the remaining bandwidth for the bottom trigger. A dynamical prescale factor is associated with this trigger path. The factor changes when the instantaneous luminosity changes during the store. Some trigger requirements in the B_CHARM trigger path have been loosened to allow more events to pass within the remaining bandwidth. The two tracks are not required to have opposite charge. A minimum value for the sum of the two track's p_T is not required either. The details of this trigger path are discussed in the following.

The Level-1 trigger decision in B_CHARM_LOWPT trigger path is made on XFT tracks. The selection cuts are:

- two XFT tracks
- 4 XFT layers per track
- XFT p_T >2.04 GeV/c for both tracks
- $\Delta\phi < 90^o$

The Level-2 trigger decision in B_CHARM_LOWPT trigger path is made on SVT tracks. The selection cuts are:

- two SVT tracks
- SVT $\chi^2 < 25$
- SVT p_T >2.0 GeV/c for both tracks
- $\Delta\phi < 90^o$
- 120 $\mu m < |d_0| < 1$ mm
- L_{xy} >200 μm

The Level-3 executable matches the SVT tracks to COT tracks. The impact parameter d_0 is found from SVT tracks. The other four track parameters are from COT tracks. The Level-3 trigger has the following requirements for an event to pass:

- at least two tracks in the event
- p_T >2.0 GeV/c for both tracks
- 120 $\mu m < |d_0| < 1$ mm
- $2^o < \Delta\phi < 90^o$
- $|\Delta z_0| < 5.0$ cm
- $\sum p_T$ of two tracks > 4.0 GeV/c

B_CHARM_HIGHPT Trigger Path

The B_CHARM_HIGHPT trigger path is used as a non-prescaled and low-yield trigger path. This is useful for the cross section measurements. The trigger requirements are similar to the B_CHARM trigger path. The only difference between the two trigger paths is that B_CHARM_HIGHPT trigger has higher p_T and $\sum p_T$ requirements. The details of this trigger path are listed in the following.

The Level-1 trigger decision in the B_CHARM_HIGHPT trigger path is made on XFT tracks. The selection cuts are:

- two XFT tracks
- 4 XFT layers per track
- XFT p_T >2.23 (changed to 2.46 later) GeV/c for both tracks
- two tracks have opposite charge
- $0 < \Delta\phi < 135^o$
- scalar sum p_T of two tracks > 6.0 (changed to 6.5 later) GeV/c

The Level-2 trigger decision in the B_CHARM trigger path is made on SVT tracks. The selection cuts are:

- two SVT tracks
- SVT $\chi^2 < 25$
- SVT p_T >2.25 (changed to 2.5 later)GeV/c for both tracks
- two tracks have opposite charge
- $2^o < \Delta\phi < 90^o$
- 120 $\mu m < |d_0| < 1$ mm
- L_{xy} >200 μm

- $\sum p_T$ of two tracks > 6.0 (changed to 6.5 later) GeV/c

The Level-3 executable matches the SVT tracks to COT tracks. The impact parameter d_0 is found from SVT tracks. The other four track parameters are from COT tracks. The Level-3 trigger has the following requirements for an event to pass:

- at least two tracks in the event
- p_T >2.0 GeV/c for both tracks
- 120 $\mu m < |d_0| < 1$ mm
- L_{xy} >200 μm
- $|\Delta z_0| < 5.0$ cm
- $|\eta|$ <1.2

4.1.2 Trigger Path Selection

In this analysis, the "realistic simulation" package will be used to determine the trigger efficiency of different decay channels. Currently, this package only simulates the trigger response by making scenario "A" requirements. Among the three trigger paths in the dataset "hbot0h", the B_CHARM trigger path is very close to the scenario "A" requirements. The B_CHARM_HIGHPT is also similar to scenario "A", only with different p_T cuts for individual tracks and track pairs. On the other hand the B_CHARM_LOWPT trigger path is significantly different from the scenario "A" requirements. To make the data and Monte Carlo sample consistent, we don't use the events from B_CHARM_LOWPT trigger path in this analysis. To exclude the events from the B_CHARM_LOWPT trigger path, a Level-3 filter "Prereq" [47] is used to select events by checking the Level-3 trigger bits.

4.1.3 Good Runs Selection

The run range covered in this analysis is from 138425 to 156116. However, not every run is suitable for this analysis due to different conditions when the data was

taken. The good run criteria are set by the CDF B validation subgroup [48], which is a subgroup of the CDF validation group. The CDF Run II Run Database provides run-by-run information about the DAQ system, trigger rates and beam conditions [49]. The good run criteria are determined by the entries in the RunConfiguration table in the CDF Run Database. For a run to be considered as a "Good Run", the following Boolean values in the RunConfiguration table have to be true: RUNCONTROL_STATUS, SHIFTCREW_STATUS, OFFLINE_STATUS, CLC_STATUS, L1T_STATUS, L2T_STATUS, L3T_STATUS, SVT_STATUS, SVX_STATUS, SVTOFFLINE and COT_OFFLINE.

- The RUNCONTROL_STATUS is automatically set to true by Run Control when there are at least 100 million collisions, 10000 Level-1 accepts, 1000 Level-2 accepts and at least 1 nb^{-1} integrated live luminosity in a run.
- The SHIFTCREW_STATUS is filled by the DAQ Ace at end of each run.
- The OFFLINE_STATUS is filled by the offline monitor.
- The CLC_STATUS is set to true if the CLC high voltage was on during the run and the consumer plots of luminosity and beam conditions are normal.
- The L1T_STATUS and L2T_STATUS are set by the consumer operator (CO) when the TrigMon plots are normal.
- The L3T_STATUS bit is set to true if the SVX reformatter error rate is less than 1%.
- The SVX_STATUS is set to true if the SVX is powered on.
- The SVT_STATUS is set to true if the SVT online beam position subtraction is done correctly and the SVT occupancy is normal.
- Both COT_OFFLINE and SVT_OFFLINE are set after the data is examined by experts. When the D^0 and D^{*+} yields are within the expected range the SVT_OFFLINE is set to true. When there are fewer than 1% bad COT channels

and the integrated live luminosity is at least 10 nb^{-1}, the COT_OFFLINE bit is set to true.

After excluding "bad" runs, the total integrated luminosity used in this analysis is $\sim$ 65 pb^{-1}.

4.2 Monte Carlo Data Sample

In this section we will describe the Monte Carlo data sample used in this analysis. Monte Carlo data samples are used intensively in this analysis to obtain the selection criteria for our interesting decay channels, to study the background compositions and to evaluate the reconstruction efficiency. The Monte Carlo samples are usually prepared in three steps. First a particle generator is needed to simulate the process of $b\bar{b}$ pair creation and hadron fragmentation. Then the particles generated in the first step need to be handled by a decay package to decay to stable particles. Finally a trigger simulation and a detector simulation package are used to simulate what really happens in the real detector and DAQ systems.

4.2.1 B Generator

The $b\bar{b}$ Monte Carlo generator we used in this analysis is a CDF software package called "Bgenerator" [50], [51]. The Bgenerator contains two processes: generate a single b quark and then fragment it into a single B hadron, or generate a $b\bar{b}$ pair and then fragment both quarks into two hadrons. In this analysis we only generate a single quark each time. The input to the single b quark generation is a two dimensional histogram containing the correlation between the b quark transverse momentum spectrum $p_T(b)$ and the b quark rapidity y(b). The $p_T(b)$ spectrum is calculated according to reference [52]. After a single b quark is produced, it is fragmented into a B hadron based on the Peterson fragmentation function. The default value of Peterson parameter is ϵ_b= 0.006. In the generation, one can force the b quark to fragment into a specific B hadron, or into different species according to the fragmentation fraction

which we discussed in Section 2.2. The first case is useful when we just want signal events. The second case is useful when studying the background.

4.2.2 Decay Packages: EvtGen and QQ

After B hadrons are produced two decay packages are used to describe the decays of B hadrons. One is called "EvtGen" and the other one is "QQ"

EvtGen package

EvtGen [53, 54] is a decay package developed specially for B physics. It has a framework such that each decay mode is added as a module and these modules perform the simulation of the decays. The framework uses the decay amplitude for each node in a decay tree to simulate the entire decay chain, including angular correlations and CP violation effects. When we make the Monte Carlo samples for $\bar{B}^0$ study, we use EvtGen because it correctly describes all decay distributions for decays like $\bar{B}^0 \to D^+\pi^-$. However, the current version of EvtGen only describes the B meson decays and is not able to simulate B baryon (e.g. Λ_b^0 in our analysis) decays.

QQ package

QQ [55] is a decay package adapted from the CLEO experiment. It is used to decay bottom and charm particles. The new updated decay file in QQ contains all known decay channels for B mesons and baryons. So we will use QQ to generate Λ_b^0 decays and to generate the background events from all B hadron decays.

4.2.3 Trigger and Detector Simulation

After B hadrons decay, the decay products will go through the CDF detector and trigger systems. There are two different approaches to simulate this process. One is called "realistic simulation", the other is called "parametric simulation"

"realistic" simulation

The so called "realistic" simulation is actually the full simulation including effects from the time dependent SVT and SVX configurations. The full simulation includes the detailed detector simulation based on a GEANT program and the trigger simulation based on trigger emulator programs developed in CDF. The GEANT program [56] is a detector description and simulation tool which can describe the passage of elementary particles through matter. In CDF, GEANT is used to describe the detailed geometry of the CDF II detector, to track the particles passing through the detector and simulate the detector response. When Monte Carlo particles pass through the detector the simulated detector response is kept in the same format as in real data. The information from the detector is then sent to trigger emulators which simulate the CDF trigger systems. During the data taking period, the configurations of the detector and the trigger system change from time to time. For example, some parts of the Silicon detector could be turned off due to a power supply problem in some specific runs. The different configurations of the silicon detector will have different effects on the trigger efficiency. A similar thing could happen to the trigger system, for example, the SVT trigger. The "realistic" simulation allows physicists to define the specific run number that they want to simulate by supplying the corresponding detector and trigger system configurations. The "realistic" can reproduce the details of real data very well. However, it takes about half a minute to simulate one event. In some studies when millions of events are needed, it would take an unreasonably long time. In this analysis we use the "realistic" simulation to generate the signal events.

"parametric" simulation

In a study when the most detailed description of the detector and trigger system is not necessary but the speed of generating large amounts of Monte Carlo events is important, the "parametric" simulation is used. In this analysis a fast tracking simulation tool QuickSim [57] is used to simulate COT and SVX. In this tool, the descriptions of the tracking detector COT and SVX are simplified and the tracks are

created parametrically. Those parameters are tuned by comparing with real data to get the correct impact parameter resolution. The quick simulation is about two orders of magnitude faster than the full simulation. A generator level trigger simulation program GenTrig [58] is used to do trigger simulation. The program simply uses the particle information from the Monte Carlo generator and makes a selection or rejection based on the Level 1 and Level 2 trigger algorithms. Since no detector information is needed, the GenTrig works perfectly with the QuickSim. In this analysis, when we study the background for Λ_b^0 events, the GenTrig plus QuickSim are used.

4.3 Offline Track Reconstruction and Refitting

The most important high level object used in this analysis is CdfTrack [59]. In this section we will describe how tracks are reconstructed and refitted in the offline.

4.3.1 Offline Track Reconstruction

The tracks in CdfTrack are reconstructed using the information from the CDF tracking system (COT + Silicon). The Central Outer Tracker is outside the Silicon Tracking system with larger radii. Therefore, the tracks are more isolated than those in the silicon detectors. The track reconstruction is faster and easier in the COT and is therefore performed first. Before the reconstruction, the TDC readout from the COT is translated into hit positions. There are two different algorithms to form tracks from hit information in the COT. The first one is called "Segment Link", which is based on a Run I algorithm [60]. In this algorithm, the hits from each superlayer are joined up to form line segments, then those line segments are linked together to make tracks. At first the segments from axial superlayers are formed into 2D tracks, then stereo segments are picked up and attached to axial tracks. The other algorithm uses a different approach [61]. A "telescope" is created using one segment in the outer superlayer with the constraint from the expected beam spot. Then the distances of the hits from the "telescope" are calculated and filled into a histogram. The histogram will be used to determine the track parameters. The two algorithms

are combined in a way to achieve the best performance and speed of reconstruction. The tracks reconstructed with only COT hits are referred as COT-only tracks.

In the Silicon Tracker (L00+SVXII+ISL), the charge deposited on each strip is first translated into hit position information. Then the COT-only tracks are used as seeds and extrapolated into the silicon detector. When the seed track intersects the outtermost silicon layer, a window around the intersection is created based on the errors of the seed track. All the hits in the window are attached to the track and a fit will be performed for each hit. The output of the fit will be used as a seed track to add hits from the next silicon layer until there are no more silicon layers left. In the end there might be more than one output track from one seed COT track after picking up different combinations of silicon hits. The best one is chosen based on the χ^2 of the fit and the number of silicon hits picked up. This procedure is called Outside-In(OI) Tracking [62]. In the OI tracking, the $r-\phi$ hits are picked up first and SAS and 90^o z hits are added later. After OI tracking, there are still some silicon hits left which have not been picked up by any COT seed track. The Silicon Standalone tracking algorithm is then used to reconstruct the tracks with those silicon hits only.

4.3.2 Track Refitting

The tracks reconstructed using the above procedures in the process of Production are usually called default tracks (defTracks). Before we use those tracks in the further analysis, some more work needs to be done.

The defTracks are fitted with a pion hypothesis, although the real particles could be kaons or protons. To account for the correct energy loss and multiple scattering, each track is refitted for a pion, kaon and proton hypothesis. The refitted tracks from each hypothesis are stored into different collections for later analysis. For example, in the future when we mention a proton candidate track, the track is from the collection refitted with the proton hypothesis. The typical refit procedure is done as follows:

- The refit starts from a COT parent track associated with any track. Because the CDF COT tracking code does not include the multiple scattering effect in the COT volume, the errors on the COT track parameters are underestimated.

The covariance matrix of the COT track is rescaled according to the study in the reference [63]. The new scale factors for the five track parameters $(C, d_0, \phi_0, z_0, \lambda)$ are (5.33, 3.01, 3.7, 0.653, 0.58).

- Before refitting, the silicon hits from ISL and L00 are dropped. The reason for that is the alignments of both ISL and L00 detector are still in the process of being understood.
- The tracking package (TrackingKal) from the Karlsruhe group [64] is used to describe the material in the silicon detector.
- The alignment table used for the refitting is the "100030 1 GOOD".
- Finally, the tracks are refitted for the pion, kaon and proton hypothesis.

4.4 Event PreSelection

4.4.1 Track Quality Cuts

A set of track quality cuts are applied on each track according to the CDF B physics group's standard analysis advice:

- at least 20 Axial and 20 Stereo COT hits on each track
- at least 3 $r-\phi$ silicon hits on each track
- $P_t > 0.4$ MeV/c and $|\eta| < 1.3$ for each track
- $|d_0| < 0.2$ cm for each track

4.4.2 Trigger Confirmation

Another important thing to do before physics analysis is trigger confirmation. We want to assure that the tracks that we are interested in are actually those which fired the trigger. Confirming this is especially crucial for the relative branching ratio measurement. In a relative branching ratio measurement in order to determine the

trigger efficiency the Monte Carlo events are generated with only one b hadron and its decay particles per event. However, in the data there could be the tracks from B hadron on the other side of event or other volunteers from fake XFT or SVT tracks which fire the trigger. The Monte Carlo will not reproduce those situations. By requiring that candidate tracks are the trigger tracks we can exclude those volunteer events.

In the data the Level-2 trigger decision is made on SVT tracks, while in the analysis the tracks we are using are from offline reconstruction. The reconstruction algorithms are different for online and offline tracks. Thus it is is useful to match the SVT tracks and offline tracks. The matching algorithm we use is in the CDF svtsim package [65]. There, the differences between SVT tracks and offline tracks $(\Delta C, \Delta\phi_0)$ are compared. When the distance in matching space is less than 95 and the χ^2 of SVT tracks is less than 25, we accept it as a match. After the matching, the SVT track quantities (track charge, SVT track p_T, d_0, $\Delta\phi$ between two SVT tracks) are used to confirm the Scenario A trigger. In this way the online trigger decision can be redone in the offline. In addition, the Scenario A trigger cuts are performed again on the offline track quantities in this analysis. This once more reduces the possibility of volunteer events in the data.

After all the above preparation of the tracks and events, we are ready to do our physics analysis.

4.5 Event Reconstruction

In this section, we will give a brief introduction to the event reconstruction process used in this analysis.

Fig 4.1 shows two B hadron decay channels ($\bar{B}^0 \to D^+\pi^-$, $\Lambda_b^0 \to \Lambda_c^+\pi^-$) that we will study in next chapter. B hadrons are produced at the $p\bar{p}$ interaction point, which is also called the primary vertex. After being produced, B hadrons have a longer lifetime ($\sim 10^{-12}$ sec) than many other unstable particles. They will travel a few millimeters before decaying into other particles, as shown in Fig 4.1. Some of decay products decay again, such as the D^+ and Λ_c^+ in our case. If the final decay products

are all hadrons, which is our case, those decays are called hadronic decays. Those particles like protons, kaons and pions will pass through the CDF detector and leave tracks in the CDF tracking systems. Starting from those tracks we can trace back to original parent particles. This process is called event reconstruction.

At a $p\bar{p}$ collider, there are lots of tracks reconstructed in one event. Those tracks are coming from the B hadron fragmentation process, underlying events and pile-up events. The B hadron fragmentation process has been discussed in the Chapter 2. When protons and anti-protons collide, it is actually the partons inside the proton and anti-proton which interact with each other. The particles produced in the collisions, excluding those which produced the b quark pair, are called underlying events. There can be more than one proton and anti-proton collision at each beam bunch crossing. The additional collisions are called the pile-up events. There is not much difference between tracks from B hadronic decays and other processes we discussed above. The decays we are interested in, like the two decays channels shown in Fig 4.1, are called signals. All other tracks are background. Our job is to distinguish the signal tracks from the background.

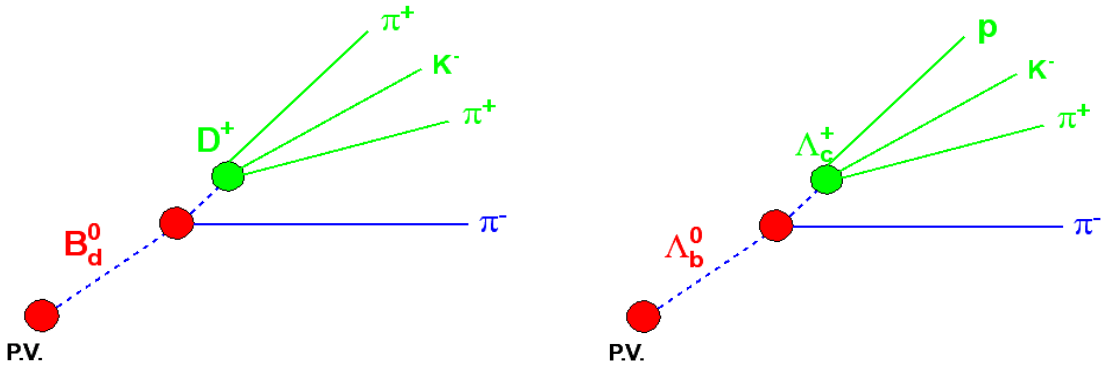

Figure 4.1: The decay diagrams of $\Lambda_b^0 \to Lambda_c^+ \pi^-$ and $\bar{B}^0 \to D^+ \pi^-$

From Fig 4.1 we can see the decay topology of the two signal channels is identical, so the reconstruction process for the two channels are also almost the same. In the next paragraph, we will only use the Λ_b^0 reconstruction as an example to explain the reconstruction process.

We start the signal reconstruction using any combination of 4 tracks in the event. Three of tracks are assigned as proton, kaon and pion candidates which come from a Λ_c^+ candidate. The fourth track is assumed to be a pion from the Λ_b^0 candidate. The charges of the four tracks should match the hypothesis of Λ_b^0 . For example, the charge of the fourth track should be opposite to the sum of the charges of the three candidate tracks from Λ_c^+ because Λ_b^0 is a neutral particle. These four candidate tracks should pass the trigger confirmation and track quality cuts we discussed in the Section 4.4. Then they should pass a set of cuts developed to select only real Λ_b^0 s and to reject fake Λ_b^0 s. The details of those cuts will be described in the next chapter. For example, given that the B hadrons travel a short distance before decaying, the distance between the primary vertex and the Λ_b^0 vertex and the distance between the Λ_b^0 and the Λ_c^+ vertex can be used to reduce the background. However, no cuts can reject all background, our signals will always sit on some kind of background in the mass distribution plots.

Chapter 5

Physics Analysis

5.1 Analysis Overview

A combination of the increased luminosity of Run II and new triggers oriented toward B-physics creates new opportunities to study the heavy baryons and expand our knowledge of the structure of baryonic matter. The spectroscopy of heavy baryon states is interesting in its own sake: only a small fraction of the heavy baryon states predicted by the quark model have been observed. Furthermore, bottom baryons may turn out to be an excellent laboratory for testing the Heavy Quark Effective Theory.

In this analysis a search for the decay[1] $\Lambda_b^0 \to \Lambda_c^+ \pi^-$ with $\Lambda_c^+ \to p^+ K^- \pi^+$ has been done with the Two Track Hadronic Trigger data. A $\Lambda_b \to \Lambda_c^+ \pi^-$ signal is observed with about 5 σ significance. This leads to a branching fraction measurement. At CDF measurements of ratios of branching fractions are more precise than absolute measurements, since most of the systematic errors cancel. It is then possible to rely on the B factories to provide precise measurements of higher-statistics branching ratios for use as denominators. So in this analysis the event yield rate of the Λ_b^0 baryon is compared with the event yield rate of the $\bar{B}^0$ meson. The number of Λ_b^0 events we observe in the data depends on the fragmentation fraction of f_{Λ_b}, the branching fraction of $\Lambda_b^0 \to \Lambda_c^+ \pi^-$, the branching fraction of $\Lambda_c^+ \to p^+ K^- \pi^+$

[1] Throughout this thesis, a reference to the charge conjugate states is implicit. For example, here, the decay $\bar{\Lambda}_b^0 \to \Lambda_c^- \pi^+$ with $\Lambda_c^- \to p^- K^+ \pi^-$ has also been searched for and reconstructed.

and the overall reconstruction efficiency ϵ_{Λ_b}. We choose the decay $\bar{B}^0 \to D^+\pi^-$ with $D^+ \to \pi^+ K^- \pi^+$ as our reference mode for the relative branch ratio measurement. The number of $\bar{B}^0$ events depends on the fragmentation fraction f_d, the branching fraction of $\bar{B}^0 \to D^+\pi^-$, the branching fraction of $D^+ \to \pi^+ K^- \pi^+$ and the overall reconstruction efficiency $\epsilon_{\bar{B}^0}$. So we get the following formula:

$$\frac{f_{\Lambda_b} BR(\Lambda_b \to \Lambda_c^+ \pi^-) BR(\Lambda_c^+ \to pK\pi) \epsilon_{\Lambda_b}}{f_d BR(\bar{B}^0 \to D^+\pi^-) BR(D^+ \to K\pi\pi) \epsilon_{\bar{B}^0}} = \frac{N_{\Lambda_b}}{N_{\bar{B}^0}}. \tag{5.1}$$

It is advantageous to package the branching ratios together with other poorly known quantities such as fragmentation fractions. Therefore, the quantity reported first in this analysis is

$$\frac{f_{\Lambda_b}}{f_d} \frac{BR(\Lambda_b \to \Lambda_c^+ \pi^-)}{BR(\bar{B}^0 \to D^+\pi^-)} = \frac{BR(D^+ \to K\pi\pi)}{BR(\Lambda_c^+ \to pK\pi)} \frac{N_{\Lambda_b}}{N_{\bar{B}^0}} \frac{\epsilon_{\bar{B}^0}}{\epsilon_{\Lambda_b}}. \tag{5.2}$$

Then the branching fraction of $\Lambda_b^0 \to \Lambda_c^+ \pi^-$ is extracted from the above formula.

In the next part of this chapter, the $\bar{B}^0$ and Λ_b^0 signals will be reconstructed first. The proper fit models will be developed to extract the correct number of events. Then the event number ratio $N_{\Lambda_b}/N_{\bar{B}^0}$ can be obtained. Lastly, the "realistic" Monte Carlo samples are used to determine the efficiency ratio $\epsilon_{\bar{B}^0}/\epsilon_{\Lambda_b}$.

5.2 Event Reconstruction

As indicated in Section 4.5, we begin the reconstruction of Λ_b^0 candidates by confirming offline the trigger cuts corresponding to the 'Scenario A'. The offline tracks are then associated with the SVT online tracks and the 'Scenario A' trigger is confirmed again using the SVT track parameters. Then we proceed by iterating over all the tracks in the event, and retain all candidates that pass the cuts.

5.2.1 Cut Selection and Optimization

A set of selection criteria is needed to reduce the background. We use the Monte Carlo signal sample to get the distribution of quantities that we will cut on. First,

the cut values are chosen to maximize the reconstruction efficiency. Then a cut optimization process is done to determine the cut values which maximize the signal to background ratio. The details of the cut optimization are discussed in Appendix A. The final cut values we selected through this optimization are listed below. The distributions of some cut quantities from the Monte Carlo sample are shown in Appendix B.

- p_T(proton) > 2.0 GeV/c, p_T(π from Λ_b^0) > 2.0 GeV/c
- $p_T(\Lambda_c^+)$> 4.5 GeV/c, $p_T(\Lambda_b^0)$ > 7.5 GeV/c
- c$\tau(\Lambda_b^0$) > 225 μm, cτ(Λ_c^+ from Λ_b^0) > -65 μm
- $d_0(\Lambda_b^0$) < 85 μm
- p_T(proton) > p_T(π from Λ_c^+)
- Λ_c mass window [2.269,2.302] GeV/c^2
- $\chi^2_{xy}(\Lambda_b) < 30$, $\chi^2_{xy}(\Lambda_c) < 20$

5.2.2 B^0 reconstruction

We reconstructed our reference mode $\bar{B}^0 \to D^+\pi^-$ with $D^+ \to \pi^+K^-\pi^+$ first. The cuts we used to select $\bar{B}^0$ candidates are the same as the cuts we optimized for Λ_b^0 , except that we use a different mass window for D^+. The cuts are listed below. The reason for using the same cuts for both decay channels is to avoid introducing any systematic uncertainties when evaluating the reconstruction efficiency for both channels.

- p_T(one π from D^+) > 2.0 GeV/c, p_T(π from $\bar{B}^0$) > 2.0 GeV/c
- $p_T(D^+)$>4.5 GeV/c, $p_T(\bar{B}^0)$ >7.5GeV/c
- c$\tau(\bar{B}^0)$ > 225 μm, cτ(D^+ from $\bar{B}^0$) > -65 μm
- $d_0(\bar{B}^0)$ < 85 μm

- D^+ mass window [1.849,1.889] GeV/c^2
- $\chi^2_{xy}(\bar{B}^0) < 30$, $\chi^2_{xy}(D^+) < 20$

After running through the data sample using the above cuts, the mass distribution of $\bar{B}^0$ event is shown in Fig. 5.1. We can see that there is a very clear Gaussian shape

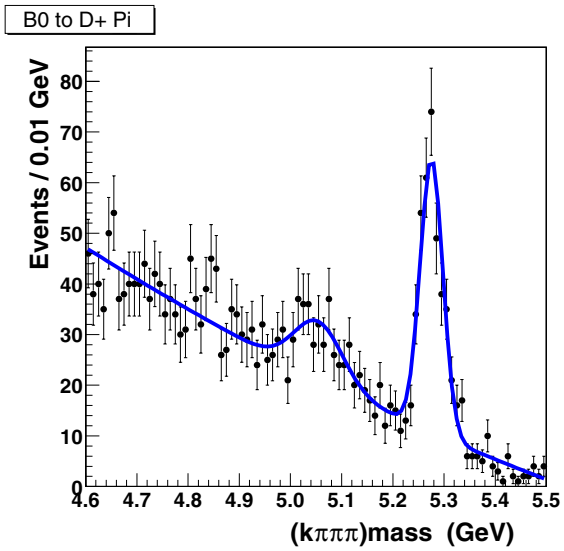

Figure 5.1: Invariant mass distribution of $\bar{B}^0 \to D^+\pi^-$ candidates. The histogram is fit with two Gaussians on top of a second order polynomial background.

peak at the value of the PDG $\bar{B}^0$ mass 5.279 GeV/c^2. This is the signal peak we are looking for. There is another roughly Gaussian shaped peak at the left of the signal peak. This peak is mainly coming from the decay $\bar{B}^0 \to D^{+*}\pi^+$ while D^{+*} decays to a D^+ and a π^0. Because the neutral pion does not leave a track in the detector, we can only reconstruct the D^+ and π^+. So the reason the peak shifted to the left is that we missed a π^0. We usually call this kind of peak a satellite peak. The two Gaussian peaks are sitting on top of a rather smooth background. In Fig 5.1 we fit the mass distribution histogram with two Gaussian peaks and a second order polynomial background. In Fig 5.2 a broad Gaussian function is used to describe the background. This alternate fit is also plotted on the histogram. The results of the two fits are shown in the Table 5.1.

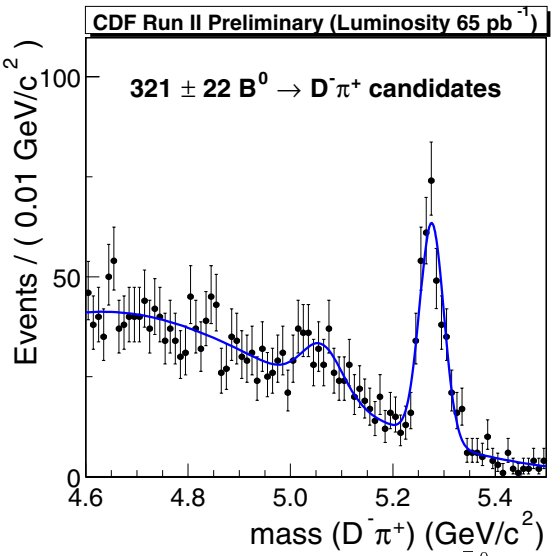

Figure 5.2: Invariant mass distribution of $\bar{B}^0 \to D^+\pi^-$ candidates with an alternative fit. The histogram is fit with two Gaussians on top of a broad Gaussian background.

The cuts we use are optimized to enhance the $\Lambda_b^0 \to \Lambda_c^+\pi^-$ signal. So the number of $\bar{B}^0$ events found here is different from the yield in other CDF analyses in which the cuts are optimized for the B^0 signal. We did a comparison with the cuts utilized in the B_s and B_d yield analysis [66]. The following are the cuts in that analysis:

- $\Delta R(D^+, \pi_B) < 1.5$ (π_B is the π from $\bar{B}^0$)
- $p_T(D^+) > 4.0$ GeV/c, $p_T(\bar{B}^0) > 6.0$ GeV/c
- $L_{xy}(\bar{B}^0) > 100$ μm, $L_{xy}(D^+) > 600$ μm
- $d_0(\bar{B}^0) < 100$ μm
- $\chi^2_{xy}(\bar{B}^0) < 15$, $\chi^2_{xy}(D^+) < 10$

The result from applying the above cuts are shown in Fig. 5.3. We fit the histogram with two Gaussian peaks and an exponential background as was done in the B_s and B_d yield analysis. The output of the fit is shown in Table 5.1. A consistent $\bar{B}^0$ yield is observed. This serves as a cross check of our analysis.

Cuts	Fit Model	Num of $\bar{B}^0$	Mass (MeV/c^2)	Width (MeV/c^2)	χ^2/ndf
our cuts	Polynomial bkg.	301±22	5276±2	22±2	1.22
our cuts	Gaussian bkg.	321±22	5276±2	22±2	0.92
cuts in Ref. [66]	Exponential bkg.	505±44	5276±2	24±2	1.07

Table 5.1: A summary of the yield of $\bar{B}^0$ with different fit models and different cuts.

When comparing the results of our two different fits using our analysis cuts as shown in Fig 5.1 and 5.2, we find that the fit with a broad Gaussian background has the smaller χ^2/ndf. So we choose that fit and the resulting 321±22 as the number $\bar{B}^0$ events we found in the data.

5.2.3 Λ_b^0 reconstruction

The cuts in Section 5.2.1 are now applied in the $\Lambda_b^0 \to \Lambda_c^+\pi^-$ search. We first look at the invariant mass distribution for the three Λ_c^+ candidate tracks (p, K, π). The resulting Λ_c^+ peak is given in Fig. 5.4. These are all Λ_c^+ candidates corresponding to a Λ_b^0 mass window from 5.2 GeV/c^2 to 5.8 GeV/c^2. We can see a clear peak on top of a background. Setting a mass window around the Λ_c^+ peak and adding a fourth candidate track to it, we get the invariant mass distribution for the Λ_b^0 signal. The Λ_b^0 signal is shown in Fig. 5.5. A $\sim 5\sigma$ peak is evident. A simple fit is performed on the histogram using a single Gaussian and a linear background. This is just to show that there is an obvious Λ_b^0 peak. The distribution is, however, far more complicated than a simple linear background, especially at the left side of the Λ_b^0 peak. To measure the branching fraction, an accurate number of Λ_b^0 events is crucial. In the next few sections, the background will be studied in detail and a proper fit model will be developed to extract the event number.

Finally, the correlation between the invariant masses of the Λ_b^0 and the Λ_c^+ is

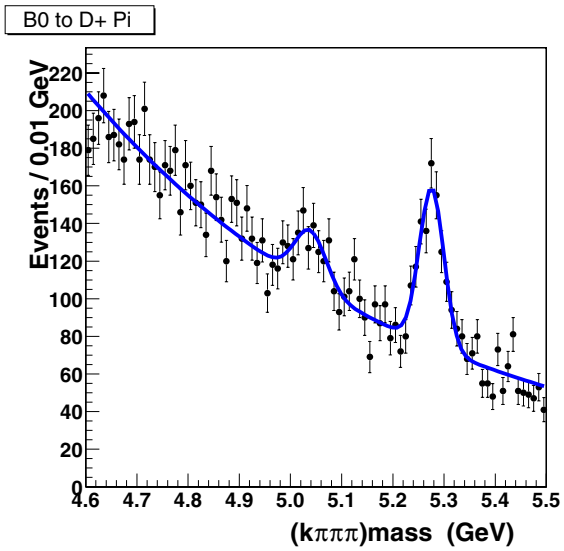

Figure 5.3: Invariant mass distribution of $\bar{B}^0 \to D^+\pi^-$ candidates. The histogram is fit with two Gaussians on top of an Exponential background shape.

shown in Fig. 5.6. There is a clear simultaneous excess near the world average mass values of both Λ_b^0 and Λ_c^+, demonstrating that all of the Λ_b yield is indeed arising from $\Lambda_b^0 \to \Lambda_c^+\pi^-$ decays. This plot also indicates that the remaining Λ_c^+'s from Fig. 5.4 are coming from the reflections of other modes that end up in the low Λ_b mass sideband.

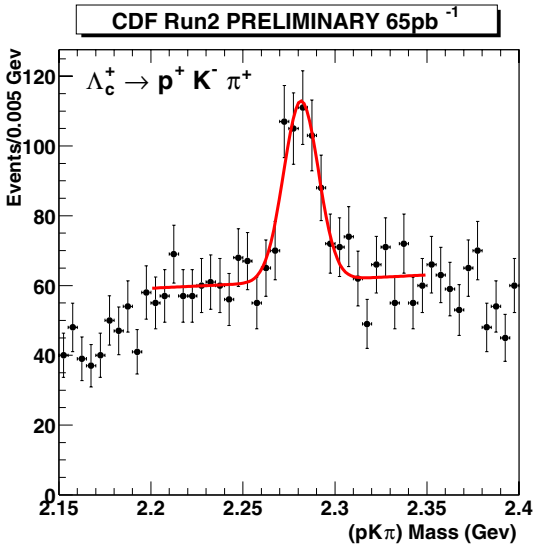

Figure 5.4: Invariant mass distribution of $\Lambda_c^+ \to p^+ k^- \pi^+$ candidates, which are reconstructed as a part of the Λ_b candidates.

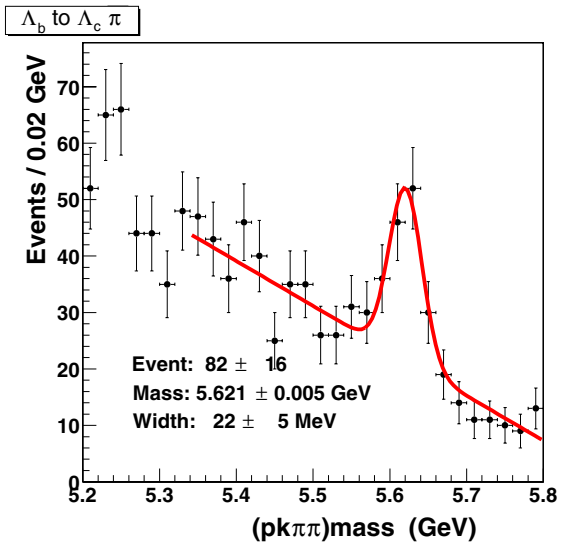

Figure 5.5: Invariant mass distribution for $\Lambda_b^0 \to \Lambda_c^+ \pi^-$ candidates. The distribution is fitted with a sum of a single Gaussian and a linear background.

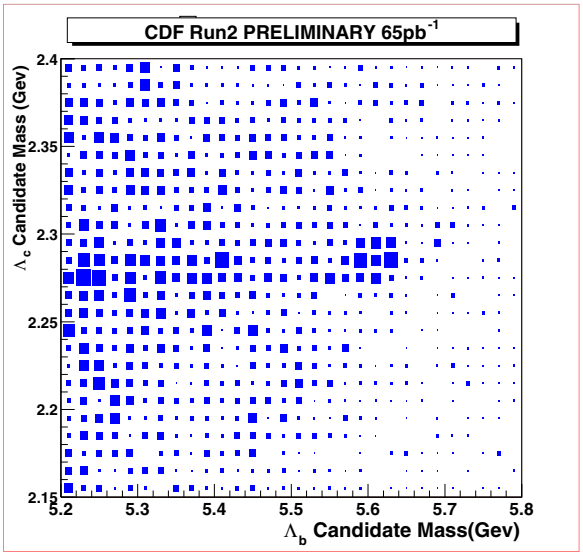

Figure 5.6: The correlation between the invariant masses of the Λ_b and a Λ_c.

5.3 Background Study

The background from the Λ_b^0 invariant mass distribution can be divided into two categories: combinatorial background and physics background. The combinatorial background comes from the randomly selected four candidate tracks which happen to pass all selection cuts. The shape of a combinatorial background is usually a smooth distribution without bumps or peaks on it. The physics background in our case comes from other decay modes. Because the daughter tracks from B hadrons have many of the same properties, like large impact parameters, many of them will survive our Λ_b^0 selection cuts. Then they can be reconstructed as Λ_b^0 candidates when one or more candidate tracks are assigned the wrong mass. This kind of background is called a reflection. For example, if one pion track from the decay $D^+ \to \pi K \pi$, where D^+ comes from $\bar{B}^0 \to D^+ \pi^-$, is taken as a proton track in the decay $\Lambda_c^+ \to pK\pi$, where Λ_c^+ comes from a Λ_b^0 decay, and if all of the other three candidate tracks come from the same $\bar{B}^0$ decay and are assigned with correct masses, this $\bar{B}^0$ can be reconstructed as a Λ_b^0 and possibly pass all of the Λ_b^0 selection cuts. Because the proton is heavier than a pion, the invariant mass of these four tracks will move up from where the $\bar{B}^0$ mass should be ($\sim$5.28GeV/c^2) toward the Λ_b^0 peak ($\sim$5.62GeV/c^2) and appear as a background in the Λ_b^0 invariant mass distribution. There are many other B hadron decays which might be reconstructed as Λ_b^0 just like the above example. These reflections can have distinct shapes in the Λ_b^0 mass region which could bias the mass fit. To take account of this effect we need do a thorough study on those B hadron backgrounds. To get a better sense of the background shape, a Λ_b^0 invariant mass distribution with a wider mass window is provided in the Fig 5.7. The mass range is from 4.6 GeV/c^2 to 7.0 GeV/c^2. We will study the background and perform our fit in this range. The details of the analysis of the physics background is described below.

5.3.1 Background from "Four prong" B meson decay

As discussed above, the decay

$$\bar{B}^0 \to D^+ \pi^-, \quad D^+ \to \pi^+ K^- \pi^+$$

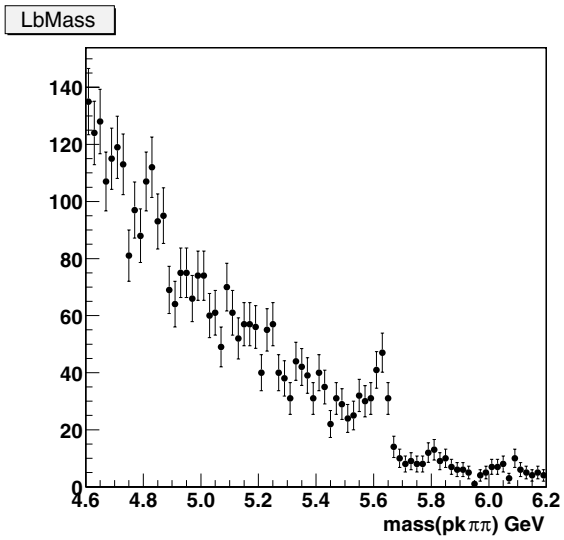

Figure 5.7: Λ_b^0 invariant mass distribution.

might be reconstructed as a Λ_b^0 and make up part of the left side background. Other B meson decays which have exactly four final charged decay products can also be fully reconstructed as Λ_b^0 and reside in the Λ_b^0 mass distribution as background. Those decays are called "four prong" decays. The reflections from those decays are called "four prong" reflections. Four prong reflections are dangerous because they might have a narrow and Gaussian-like structure and be close to the region of the signal peak. A $b\bar{b}$ Monte Carlo sample was generated with only four prong B hadron decays being allowed. The "realistic" simulation is then performed on this sample. Finally, we try to reconstruct Λ_b^0 out of this sample. The resulting mass distribution is shown in Fig 5.8. This is the background shape from four prong decays. The distribution is fitted using a combination of a Gaussian and a Landau probability density function.

5.3.2 Background from all other B meson decays

Besides the four prong B meson decays, other B meson decays can also comprise part of the background. For example, the following decays belong to this category.

$$\bar{B}^0 \to D^+\pi^-, \quad D^+ \to \pi^+K^-\pi^+\pi^0$$

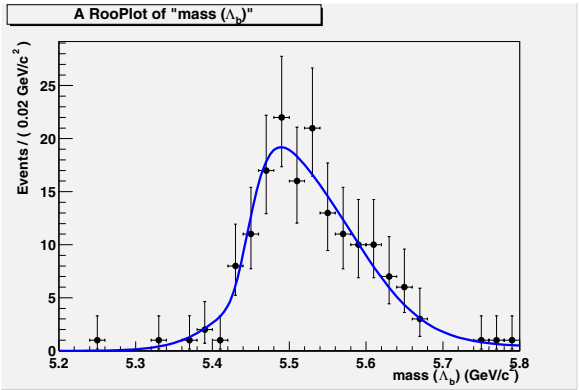

Figure 5.8: The shape of the four-prong reflection sample reconstructed using the Λ_b^0 hypothesis, obtained from the realistic Monte Carlo simulation.

$$B^+ \to D^0\pi^+, \quad D^0 \to \pi^+K^-\pi^0$$

Those decays can only be partially reconstructed when using the Λ_b hypothesis because there are more than four final decay products and one or more daughter particles are missing in the Λ_b^0 reconstruction. The shape of the distribution of reflections from partially reconstructed B mesons is smoother and lies further away from the Λ_b^0 signal peak than the four prong reflections. So this reflection shape is not as important as the shape from the four prong reflections. To get the shape a parametric Monte Carlo sample of generic B meson decays was generated and only the decays from this category are kept. Again, we try to reconstruct Λ_b^0 from this sample. The invariant mass distribution is the reflection shape we want and is shown in Fig 5.9. A zoom-in version of this reflection shape is shown in Fig 5.10 focusing upon the region near the Λ_b^0 signal peak.

5.3.3 Background from all other Λ_b decays

Besides the contribution from B meson decays, the background also contains the reflections from other Λ_b^0 decay modes, for example the following decays.

$$\Lambda_b^0 \to \Lambda_c^+\rho^-, \quad \rho^- \to \pi^-\pi^0$$

$$\Lambda_b^0 \to \Sigma_c^+\pi^-, \quad \Sigma_c^+ \to \Lambda_c^+\pi^0$$

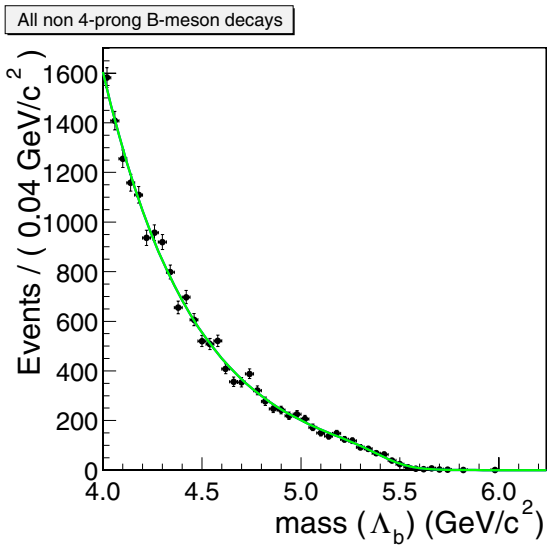

Figure 5.9: A fit to the invariant mass distribution of all other non-four-prong B-meson decays.

Those decays have more than four final decay products and, thus, can be only partially reconstructed as Λ_b^0 . Therefore, the invariant mass from them will move toward the left of Λ_b^0 signal peak because one or more daughter particles are missing. A parametric Monte Carlo simulation of Λ_b^0 decays to all known modes was generated and then the Λ_b^0 signal was reconstructed from it. Other b baryons are ignored in this study because they are produced very rarely. The output invariant mass distribution is shown in Fig 5.11 with a zoom-in version shown in Fig 5.12 focusing only on the region near the Λ_b^0 peak.

5.3.4 Reflection from $\Lambda_b^0 \to \Lambda_c^+ K^-$ decays

This decay mode is not included in the above "all other Λ_b decays" because it has not been explicitly observed yet. However, the reflection from this decay due to assigning a pion mass to a kaon track is very close to the Λ_b^0 signal peak. Moreover, a BELLE measurement [67] showed that the branching fraction of $\bar{B}^0 \to D^+ K^-$ is about 8% of the branching fraction of $\bar{B}^0 \to D^+ \pi^-$. Due to the similarity of the decay $\Lambda_b^0 \to \Lambda_c^+ \pi^-$ and $\bar{B}^0 \to D^+ \pi^-$, we expect that the number of the $\Lambda_b^0 \to \Lambda_c^+ K^-$ decays

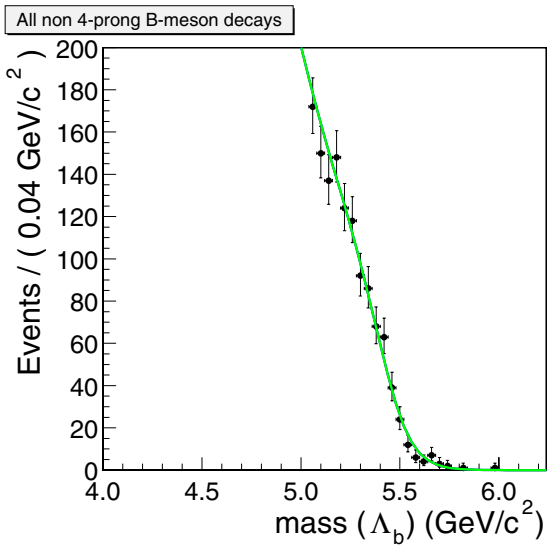

Figure 5.10: A fit to the invariant mass distribution of all other non-four-prong B-meson decays, focusing on the behavior of the function near the Λ_b^0 peak.

is about 8% of the Λ_b^0 yield. Because of the above reasons we consider this reflection as part of our background. A "realistic" Monte Carlo sample is used to get the shape of the reflection since the reflection is very close to the signal peak and the Λ_b^0 signal number may be sensitive to the shape. The shape with a Gaussian fit is shown in Fig 5.13.

5.3.5 Combinatorial Background

Because B hadrons that are heavier than Λ_b^0 are produced very rarely, the background on the right side of Λ_b^0 is not likely to be coming from other B hadron decays. So we assume the background on the right sideband is from the random combinations of any four candidate tracks which have successfully passed all Λ_b^0 selection cuts. From Fig 5.7, the background shape on the right side of the signal is a falling exponential function.

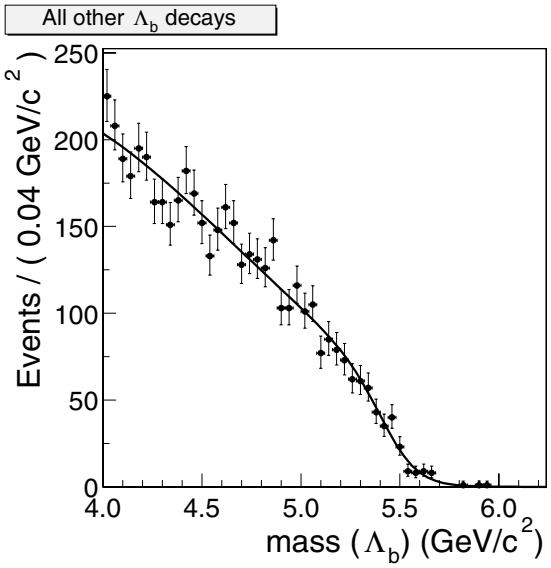

Figure 5.11: A fit to the invariant mass distribution of all other Λ_b^0 decays. Other baryons species are ignored.

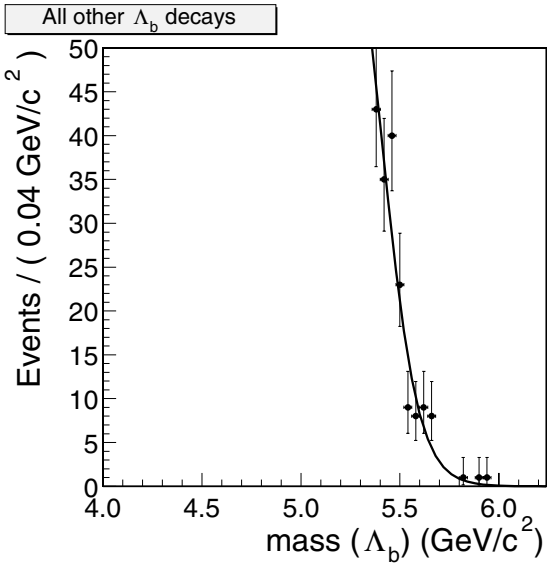

Figure 5.12: A fit to the invariant mass distribution of all other Λ_b^0 decays, focusing on the behavior of the function near the Λ_b^0 peak.

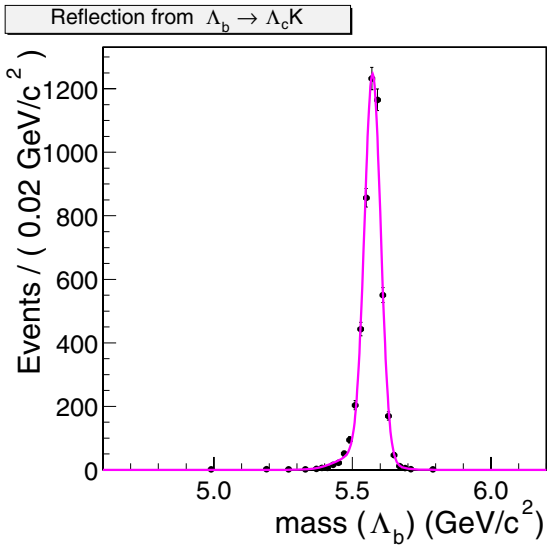

Figure 5.13: A fit to the invariant mass distribution of $\Lambda_b^0 \to \Lambda_c^+ K^-$ decays when reconstructed as $\Lambda_b^0 \to \Lambda_c^+ \pi^-$.

5.4 Fitting for the $\Lambda_b^0 \to \Lambda_c^+\pi^-$ yield

Usually it is sufficient to use a Gaussian distribution for the signal on top of a slowly varying background shape in order to extract the number of signal events in a fit. Unfortunately, the decay $\Lambda_b^0 \to \Lambda_c^+\pi^-$ is plagued by reflections from B meson decays and satellite contributions from both B mesons and other baryons. This section is devoted to a detailed description of how these contributions are taken into account and how the Λ_b^0 yield is extracted. The strategy we use here is:

- first, define all the components of the Λ_b^0 invariant mass distribution including the signal and the background,
- then the constraints and normalization between those components are determined based on all available information,
- finally put the fit components and constraints into a one dimensional binned likelihood fit and get the number of signal events from the output of the fit.
- The goodness of the fit will be studied using a Toy Monte Carlo sample.

5.4.1 Components of the Λ_b^0 mass fit

The Λ_b^0 mass fit is a one-dimensional binned extended likelihood fit that has the following six components:

1. $\Lambda_b^0 \to \Lambda_c^+\pi^-$ **signal:** It is modeled by a Gaussian distribution with the width fixed to 23 MeV, which is obtained from the "realistic" signal Monte Carlo. The center of the Gaussian and its normalization are floating in the fit.
2. **Four-prong B meson reflections:** This is a collection of all known reflections from B mesons decaying to four tracks. The shape has been obtained in Section 5.3 and is frozen in the fit for the Λ_b^0 yield. Only its normalization is floating.

3. **Background from all other B meson decays:** This is the background from B meson decays except for four-prong B meson reflections which are treated separately. The shape is modeled by a histogram from the parametric simulation and fit to a smooth functional shape as was discussed in Section 5.3. This shape is frozen in the fit for the Λ_b^0 yield and only its normalization is floating.

4. **Background from all other Λ_b^0 decays:** This is also modeled by a histogram obtained from the parametric simulation and is fit to a smooth functional shape as was discussed in Section 5.3. This shape is frozen in the fit for the Λ_b^0 yield and only its normalization is floating.

5. $\Lambda_b^0 \to \Lambda_c^+ K$ **decays:** The shape is from the realistic simulation and is fixed in the fit. The number of events for this reflection is also fixed at 8% of the Λ_b^0 yield as discussed in Section 5.3.

6. **Combinatorial background:** The shape is represented by a falling exponential. This component is almost exclusively constrained on the right sideband, where the contribution of components 2-4 is negligible. The slope of the exponential is floating in the fit.

5.4.2 Constraints in the Λ_b^0 mass fit

The shapes of the components 2-5 from Sec. 5.4.1 are frozen in the fit and only their normalizations are floating. In an extended likelihood fit, the normalization is the number of events of each particular component. We denote the number of events of the four-prong reflections by $N_{\rm ref}$, the number of "other B meson decays" by $N_{\rm otherB}$ and the number of "other Λ_b decays" by $N_{{\rm other}\Lambda_b}$.

However, these numbers of events are not completely independent. Firstly, we can find the number of reflection events from the decay $\bar{B}^0 \to D^+\pi^-$ in the Λ_b^0 mass region. That puts a constraint on $N_{\rm ref}$, because about half of $N_{\rm ref}$ is comprised of the decay mode $\bar{B}^0 \to D^+\pi^-$. Secondly, the total branching ratio contributing to the four-prong B meson component is related to the total B meson branching ratio. That constrains $N_{\rm ref}/N_{\rm otherB}$. Lastly, the contribution of other Λ_b decays is driven by $f_{\rm baryon}$.

Assuming that the $BR(\Lambda_b^0 \to \Lambda_c^+\pi^-)$ is relatively small, $N_{\mathrm{other}\Lambda_b}/(N_{\mathrm{ref}} + N_{\mathrm{otherB}})$ is proportional to $f_{\mathrm{baryon}}/(f_u+f_d+f_s)$. The detailed description of how those constraints are determined is given in the Appendix C. A summary of the constraints we obtained is given in the following.

Summary of the fit model and constraints

These three external constraints are added to the negative log-likelihood as χ^2 terms multiplied by 0.5. The factor of 0.5 comes from taking a negative log of a Gaussian probability and is necessary to obtain the correct correlation between the fit parameters in the presence of the terms for the external constraints. Consequently, the negative log-likelihood is modified in the following way:

$$-\ln\mathcal{L} \to -\ln\mathcal{L} + \sum_{i=1}^{3}\frac{1}{2}\left(\frac{f(N,\cdots)-C_i}{\sigma_i}\right)^2$$

The three constraints, C_i, as explained above, are:

C_1: the number of four-prong B meson reflections, N_{ref}, is constrained to 81.6 ± 24.5

C_2: the ratio of the number of four-prong reflections to all other B meson decays, $N_{\mathrm{ref}}/N_{\mathrm{otherB}}$, is constrained to $5.6 \pm 1.5\%$

C_3: the fraction of the Λ_b component to the sum of the B meson components $B_d + B_u + B_s$, $N_{\mathrm{other}\Lambda_b}/(N_{\mathrm{ref}} + N_{\mathrm{otherB}})$, is constrained to $74.7 \pm 25.2\%$

5.4.3 The Fit Result

The result of the fit, including all the external constraints, is shown in Fig. 5.14. We will take this fit as our "baseline" fit. The solid blue line overlapped with the data points is the overall fit. The different background components are also shown in the figure. A zoom-in version of the fit with focusing on the region in the Λ_b^0 signal is shown in Fig 5.15. The data points and the fit agree with each other fairly well. The output of the fit parameters is given in Table 5.2. The number of Λ_b^0 events we get is 96 ± 13. The Λ_b^0 mass from the fit is 5.623 ± 0.004 GeV/c^2. The world average value is 5.624 ± 0.009 GeV/c^2.

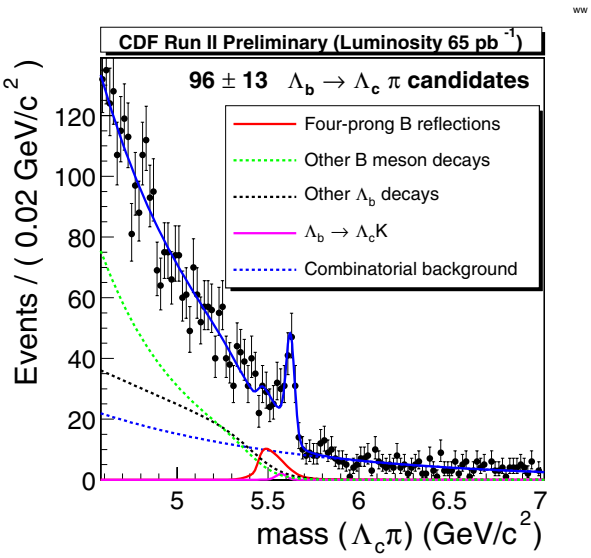

Figure 5.14: The "baseline" Λ_b mass fit.

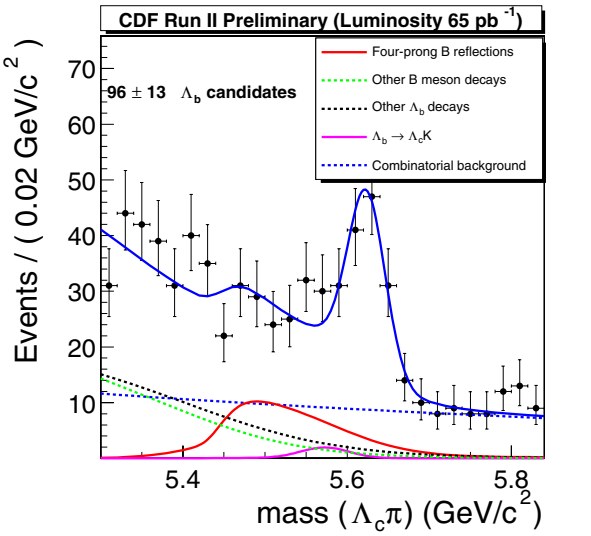

Figure 5.15: The "baseline" Λ_b mass fit, but zoomed into the region just around the Λ_b peak, demonstrating a fairly good agreement between the data points and the fit result.

Parameter	Fit Output	Global Corr
Nos Signal Events	96 ± 13	0.316655
Λ_bMass(MeV/c^2)	5.623 ± 0.004	0.150600
Nos 4-prong Reflections	91 ± 19	0.621319
Nos Other B decays	1484 ± 180	0.951576
Nos Other Λ_b	1072 ± 184	0.950523
Nos Comb Background	1098 ± 159	0.950848
Comb Bkg exp slope	-0.88 ± 0.16	0.929133

Table 5.2: Parameter central values, uncertainties and global correlation coefficients from the fit.

The following sections are devoted to the exploration of the probability of the fit quality using a Toy Monte Carlo approach, as well as further studies exploring the parameter space of the fit.

5.4.4 Studies of the fit quality using the Toy Monte Carlo approach

A "Toy Monte Carlo" technique is usually used as a sanity check of a fit. It can also be used as a method to establish the quality of a fit. The basic idea of a Toy Monte Carlo check is: first generate some Monte Carlo events according to a known distribution, then run the fit to be checked on this sample to see if the correct parameters and errors are returned by this fit. Such a Monte Carlo sample is usually called a Toy Monte Carlo sample. In this section we will use the results from our "baseline" fit to generate the Toy Monte Carlo sample and to confirm that we indeed get back the values that we put in, with correct errors. Moreover, we will demonstrate

that our fit is not an unusual case and that the discrepancies between the data points and our fit in Fig 5.15 are very likely to occur as statistical fluctuations.

Our toy Monte Carlo procedure is as follows:

1. Run the fit on real data and take this fit as the "baseline" fit. This is the fit that we are going to check using the Toy Monte Carlo sample. This step was done in the previous sections.

2. The fit parameters from the output of this fit are saved. They will be used to generate the Toy Monte Carlo samples which mimic our data.

3. A new Toy Monte Carlo "experiment" is generated according to the parameters obtained from real data. This experiment takes the contribution from each component in the "baseline" fit according to its probability density function. The overall normalization of each component is smeared based on a Poisson distribution. Assembling all of these components results a mass distribution, just like the one we got from data.

4. The external constraints are generated as well, using a Gaussian probability. For each constraint, the Gaussian is centered on the 'true' value which is calculated from the parameters output from our "baseline" fit. The width of the Gaussian is the original measurement error.

5. Now we have a mass distribution with the corresponding constraints from this Toy Monte Carlo experiment. We run our fit on this "data". The output of the fit is saved and can be used at the end to plot the pulls, fit parameters and the negative log-likelihood.

6. Steps 3-5 are repeated as many times as necessary. For our study we generate 500 such "experiments".

Fig. 5.16 shows the distribution of the negative log likelihood for the 500 Toy Monte Carlo "experiments." The value of the likelihood from the fit on real data is -26796.4, which lies near the middle of the distribution in the Fig. 5.16. The

agreement of the fitting curve from the real data is better than about 40% of "fake" data samples generated from the Toy Monte Carlo. This makes our fit fairly typical and not at all unusual, despite small discrepancies.

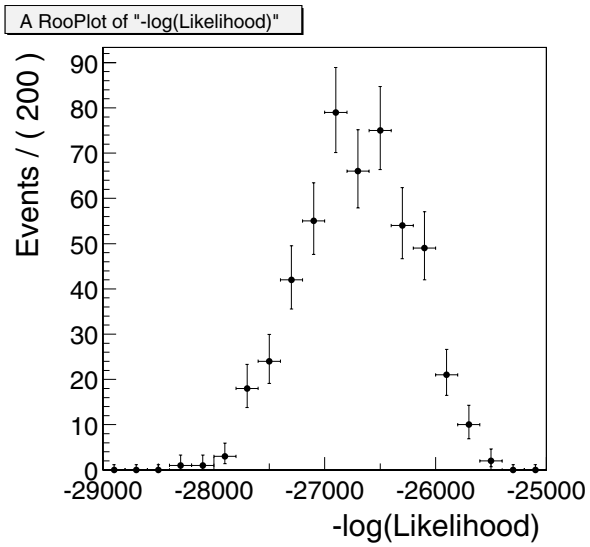

Figure 5.16: The distribution of negative log likelihood for 500 Monte Carlo "experiments."

Fig. 5.17 shows the distributions of two fit parameters of interest, the number of Λ_b^0 signal events, N_{Λ_b}, and the number of four-prong reflections, $N_{\rm ref}$. The values used to generate them were 96 and 88, respectively. The distributions peak near the input values, indicating that the fit is working well.

Finally, Fig. 5.18, 5.19 shows the pulls of the four parameters of interest: the number of Λ_b^0 signal events N_{Λ_b}, the number of four-prong reflections $N_{\rm ref}$, the number of events in the "other Λ_b" component $N_{\rm other\Lambda_b}$ and the mass of Λ_b^0 . The plot shows that those pulls are centered around 0 with width about 1. This proves there are no significant biases in the fitter and that the errors returned by it are correct.

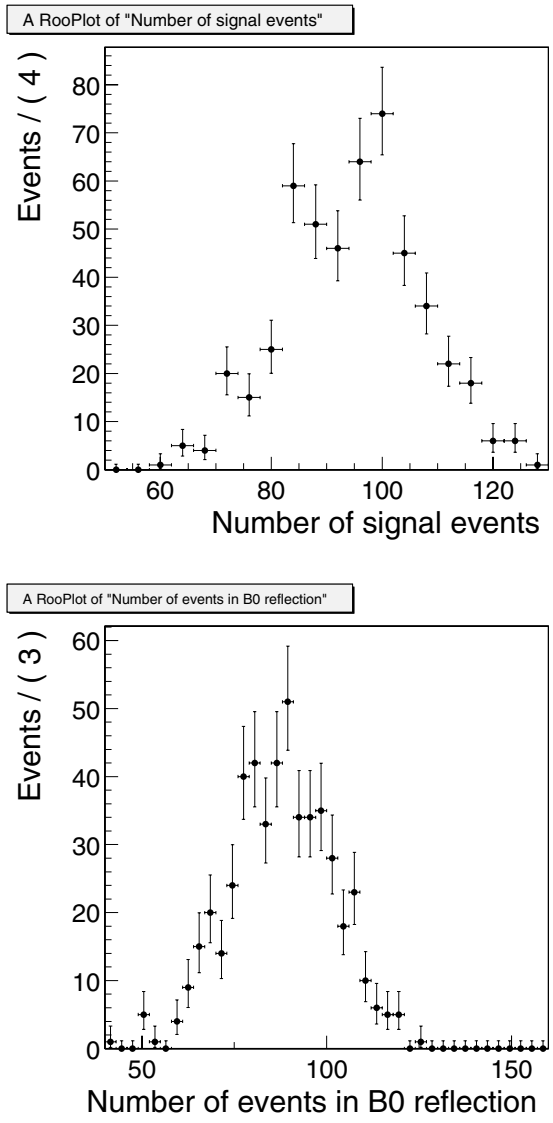

Figure 5.17: The distributions of two fit parameters of interest, the number of Λ_b signal events, N_{Λ_b}, and the number of four-prong reflections, $N_{\rm ref}$. The values used to generate them were 96 and 88, respectively.

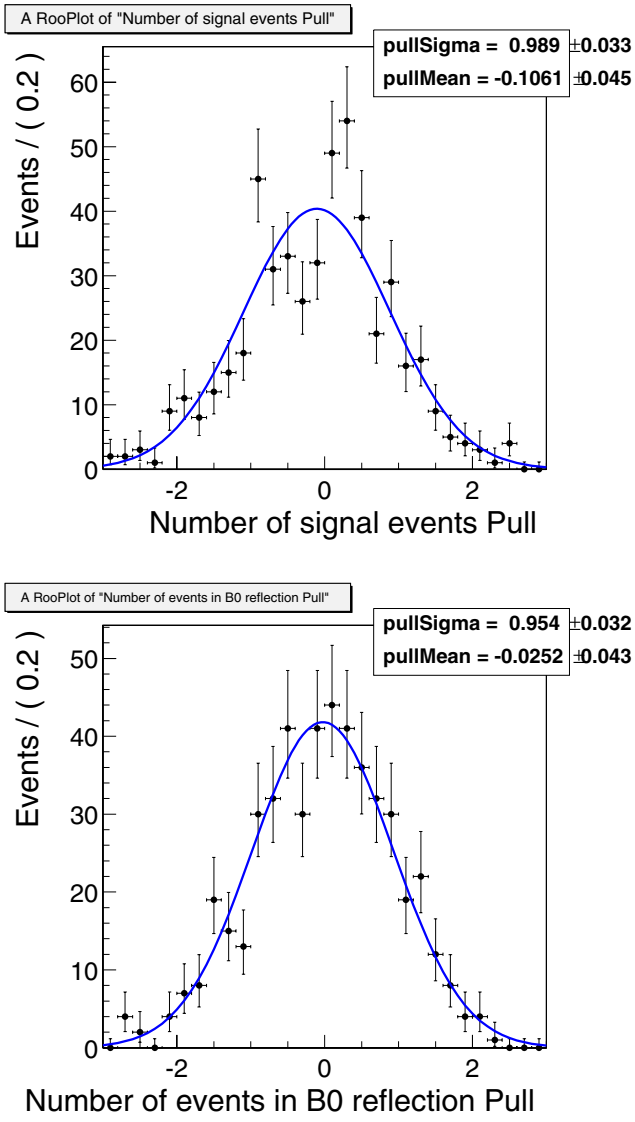

Figure 5.18: The pulls of the two parameters of interest: the number of Λ_b signal events N_{Λ_b}, the number of four-prong reflections $N_{\rm ref}$.

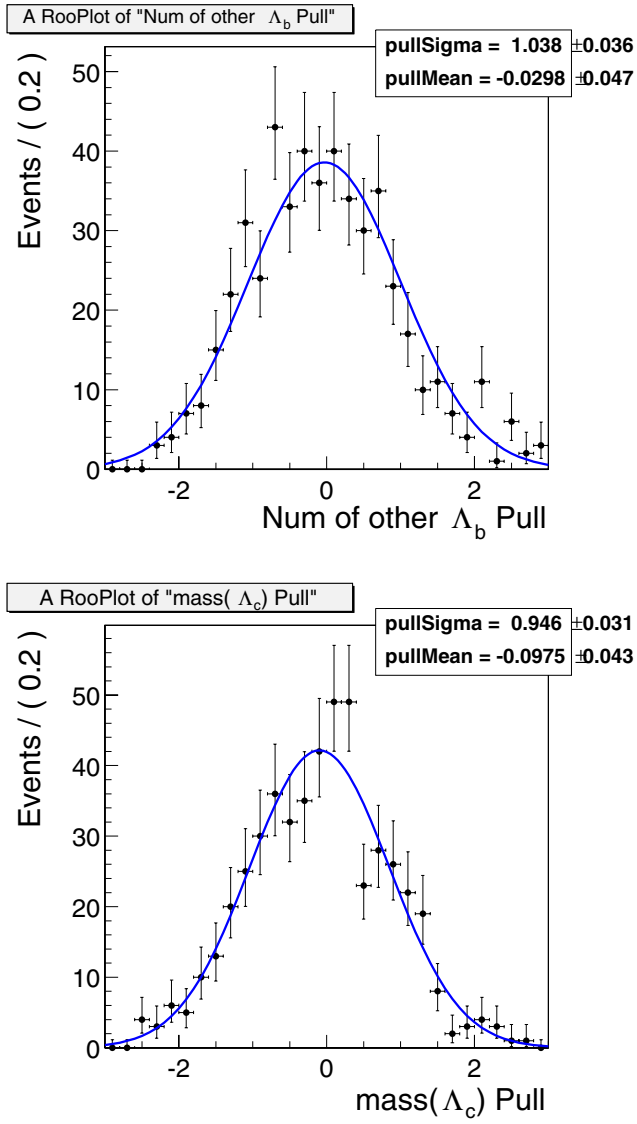

Figure 5.19: The pulls of the four parameters of interest: the number of events in the "other Λ_b" component $N_{\mathrm{other}\Lambda_b}$ and the mass of Λ_b.

5.4.5 The Λ_b fit Studies

This section describes several checks performed on the Λ_b^0 fit. Even though we determined the shape and the constraints of the fit components to the best of our knowledge, we would like to see how small changes of those constraints affect the output of the Λ_b^0 fit. In the following, one or more constraints in the fit will be dropped and then the fit is performed again. The shapes of the different fit components will also be varied and then the fit redone with the new shapes. The changes of the Λ_b^0 signal parameter in these various fits will be recorded as the systematic errors.

Fig. 5.20 shows a variation on the baseline fit, but without the constraint on $N_{\mathrm{other}\Lambda_b}/(N_{\mathrm{ref}} + N_{\mathrm{otherB}})$ ("C_3"). In this case, the "other Λ_b" component (the black dashed line) can float freely. The change of the output Λ_b^0 number of events is very small, $\Delta N_{\Lambda_b} = 0.197$.

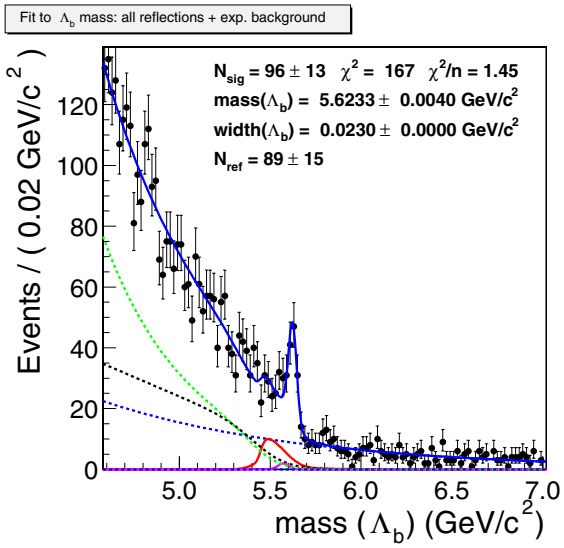

Figure 5.20: The baseline fit, but without the constraint on $N_{\mathrm{other}\Lambda_b}/(N_{\mathrm{ref}} + N_{\mathrm{otherB}})$ ("C_3"). In this fit, the "other Λ_b" component (the black dashed line) can float freely.

A similar fit, but with the constraint on N_{ref} also removed, is shown in Fig. 5.21. The "other Λ_b" component is unconstrained, and the only constraint on N_{ref} comes from the constraint on $N_{\mathrm{ref}}/N_{\mathrm{otherB}}$ (*i.e.*, "C_2"). From the output of the fit, $\Delta N_{\Lambda_b} = 0.709$

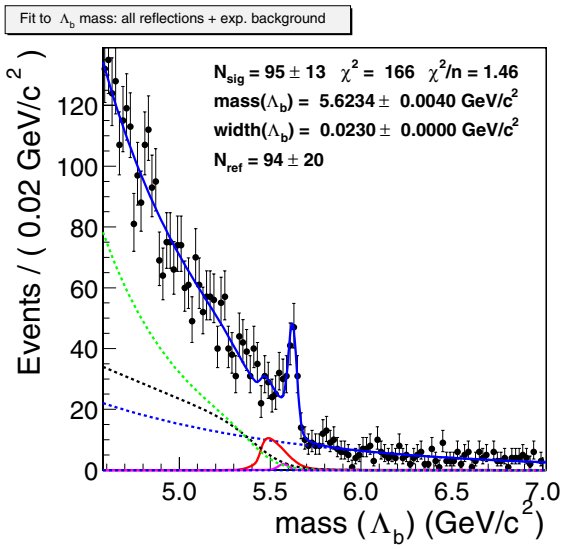

Figure 5.21: The baseline fit, but *only* with the constraint on $N_{\rm ref}/N_{\rm otherB}$ ("C_2"). The "other Λ_b" component is unconstrained, and the only constraint on the four-prong reflection component comes from C_2.

A fit with only the constraint on $N_{\rm ref}$ is given in Fig. 5.22. This fit behaves similarly to the previous two, except that $N_{\rm ref}$ is now not constrained by $N_{\rm otherB}$. The change of the Λ_b^0 number of events is also small, $\Delta N_{\Lambda_b} = 0.654$.

Finally, a fit without any constraints is shown in Fig. 5.23. The fit is still very similar to the above three fits with a change of the Λ_b^0 signal $\Delta N_{\Lambda_b} = 1.874$.

From all of the above checks, we can see that even though we applied several constraints on the fit components based on the effects we are aware of, the effect of these constraints is negligible. The agreement between the parameters of the fit without any constraints and those from our original fit with all of the constraints is excellent.

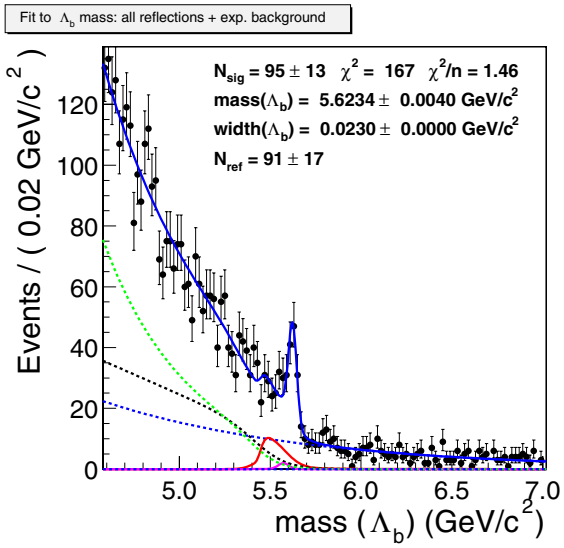

Figure 5.22: The baseline fit, but *only* with the constraint on N_{ref} ("C_1").

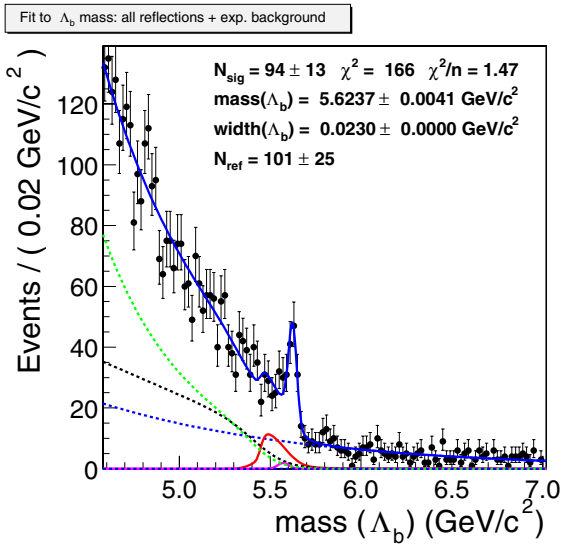

Figure 5.23: The baseline fit, but *without any* constraints.

The shapes of the "other B" and "other Λ_b" distributions were obtained by the parametric Monte Carlo and fitted in Section 5.3. By changing the parameters of the fit function, we can manually change the shapes of these two background components. In Fig 5.24, the tails of both components are made shorter and in Fig 5.25 the tails of both components are longer. The changes give us the average change of the Λ_b^0 signal $\Delta N_{\Lambda_b} = 5.778$.

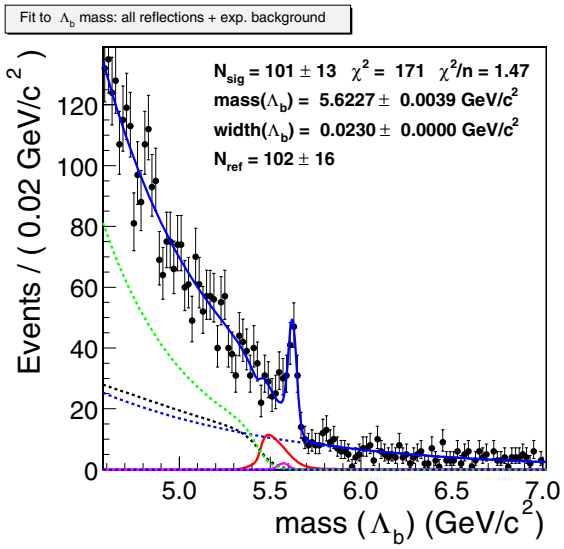

Figure 5.24: The study of the effect of a sharper cut-off of the "other B" and "other Λ_b" components. The tails of these two components (given in green and black) are made shorter.

The width of the Λ_b^0 Gaussian shaped signal is from the "realistic" Monte Carlo with the central value 23 MeV/c^2 and the one sigma error 3 MeV/c^2. We vary the width by one sigma and look at the effects of the change. In Fig 5.26, the mass distribution is fitted with the Λ_b^0 signal fixed to 20 MeV and in Fig 5.27 the width is fixed to 26 MeV. The average change of the Λ_b^0 signal event $\Delta N_{\Lambda_b} = 5.477$.

The last check is removing the background component from $\Lambda_b \to \Lambda_c K$ decay. This yields a 0.430 event change from fitting the data without this component. The output of the fit is shown in Fig 5.28.

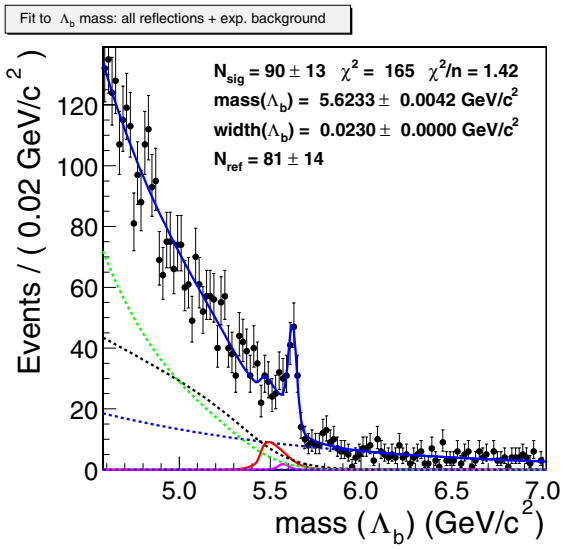

Figure 5.25: The study of the effect of a more smeared cut-off of the "other B" and "other Λ_b" components. The tails of these two components (given in green and black) are made longer.

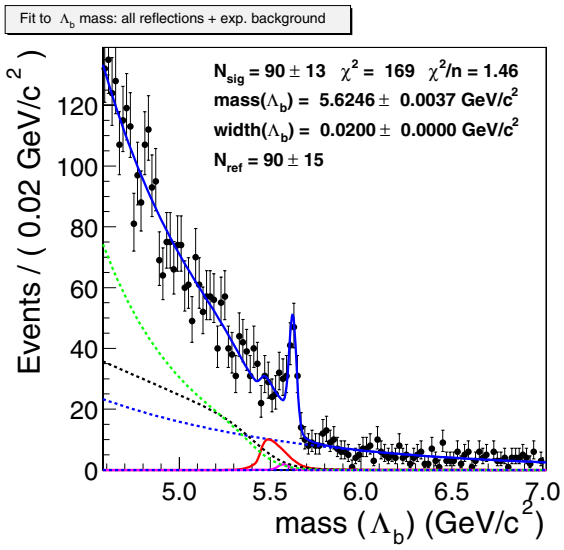

Figure 5.26: The baseline fit, but with the width of Λ_b fixed to 20 MeV/c^2, one sigma away from the central value of 23 ± 3 MeV/c^2.

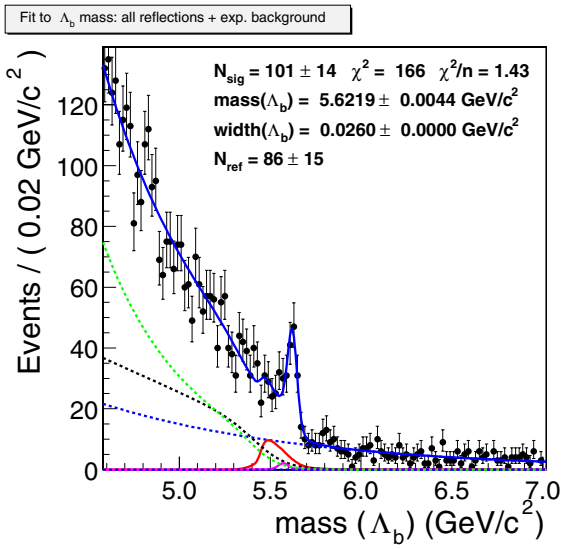

Figure 5.27: The baseline fit, but with the width of Λ_b fixed to 26 MeV/c^2, one sigma away from the central value of 23 ± 3 MeV/c^2.

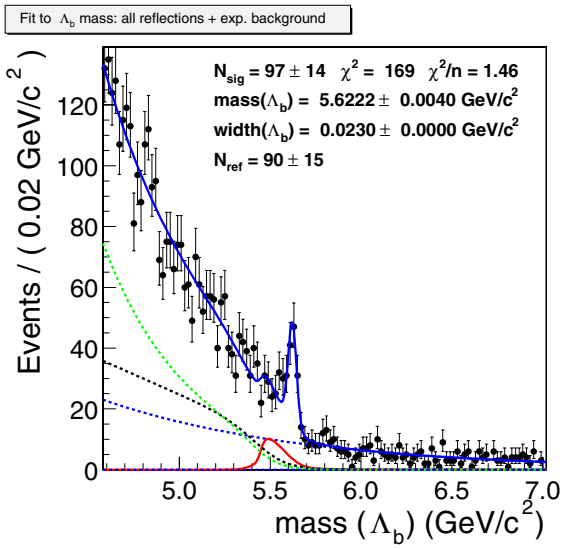

Figure 5.28: The baseline fit but *without* the $\Lambda_b \to \Lambda_c K$ component.

A list of the event number changes in different fit conditions is given in Table 5.3. In summary, we have considered the effects of the constraints and shape changes in the Λ_b^0 fitter. The quadrature sum of the event number changes will be taken as the fit model systematic uncertainty.

Type of check	ΔN_{Λ_b}
No $N_{\mathrm{other}\Lambda_b}/(N_{\mathrm{ref}} + N_{\mathrm{otherB}})$ constraint	± 0.197
N_{ref} constraint only	± 0.654
$N_{\mathrm{ref}}/N_{\mathrm{otherB}}$ constraint only	± 0.709
No constraints	± 1.874
Tails of "other B" and "other Λ_b"	± 5.778
Width of Λ_b (± 3 MeV)	± 5.477
No $\Lambda_b \to \Lambda_c K$	± 0.430
total : quadrature sum	± 8

Table 5.3: A summary of the effects (in number of events) of various changes to the fit conditions.

5.5 Determination of the efficiency ratio $\epsilon_{\bar{B}^0}/\epsilon_{\Lambda_b}$

An essential component of Eq. (5.2) is the ratio of the total reconstruction efficiencies for the two channels. To evaluate it, we use the "realistic" Monte Carlo data sample. The Bgenerator is used to generate the single $\bar{B}^0$ or Λ_b. In Bgenerator, the b-quarks are generated with $p_T(b) > 5.5$ GeV/c and $|y| < 1.3$. Two decay packages are used for b-hadron decays. QQ is used for Λ_b^0 decay and EvtGen is used for $\bar{B}^0$. Then the realistic trigger and detector simulation is performed. To take advantage of the realistic simulation, three typical run numbers are input into the simulation program. The corresponding configurations of the SVX detector and SVT system will be fetched from the run database and used in the simulation process. These three runs (142110, 151477, and 153661) represent three different periods during which the SVT system had three typical configurations.

To understand the details of the overall efficiency, ϵ_{tot}, we break down the efficiency into three components:

- **Trigger efficiency** (ϵ_{Trig}) The trigger efficiency is the probability that a generated B hadron decay passes the Two Track trigger selection. It is defined as $N_{trig}/N_{generated}$, where $N_{generated}$ is the number of events generated in the Monte Carlo sample and N_{trig} is the number of the events that pass the trigger selection. In the trigger simulation, only the B_CHARM trigger path is simulated and used to reject events.

- **Offline reconstruction efficiency** (ϵ_{Reco}) The reconstruction efficiency is the efficiency with which our reconstruction tool selects the events that have passed the trigger selection. The selection criteria here is that the events should have four reconstructible tracks and those tracks should pass the track quality cuts. When a particle passes through a region that is covered by some bad SVX wedges or the particle has high η and only passes a few or even no silicon layers, this particle can not be reconstructed as a track. In the Λ_b^0 or $\bar{B}^0$ decay channel that interests us, there are four particles in the event. If one particle does not leave a reconstructible track, the event could still pass the trigger selection,

but we can not reconstruct our signal out of it since one track is missing. The efficiency is defined as N_{reco}/N_{trig}, where N_{reco} is the number of events that pass the preselection of our reconstruction tool.

- **Analysis cut efficiency** (ϵ_{Ana}) This is the efficiency of events passing all the analysis cuts. It is defined as N_{ana}/N_{reco}, where N_{ana} is the number of events that have survived after all analysis cuts.

The total efficiency is then defined as:

$$\epsilon_{tot} = \epsilon_{Trig} \times \epsilon_{Reco} \times \epsilon_{Ana}. \tag{5.3}$$

The three efficiencies are obtained from the Monte Carlo sample and shown in the following tables: 5.4, 5.5 and 5.6. The trigger configuration is important for the first two efficiencies, and, thus, the breakdown into three typical runs needs to be done. From Table 5.4 we can see that the trigger efficiency for each decay (Λ_b^0 or $\bar{B}^0$) changes a lot for different runs. However, the efficiency ratio $\epsilon_{\bar{B}^0}/\epsilon_{\Lambda_b^0}$ from different runs agree with each other very well. Therefore, we just simply average those efficiencies. The summary of the ratios of the three efficiencies for the two decay channels and the total efficiency ratio is shown in Table 5.7. The final result of $\epsilon_{\bar{B}^0}/\epsilon_{\Lambda_b^0}$, which will be used in the Eq. (5.2), is 1.20 ± 0.02.

run	$\bar{B}^0(\%)$	$\Lambda_b(\%)$	$\bar{B}^0/\Lambda_b$
142110	0.953 ± 0.008	0.734 ± 0.007	1.30 ± 0.02
151477	1.245 ± 0.009	0.959 ± 0.008	1.30 ± 0.01
153661	1.406 ± 0.009	1.074 ± 0.008	1.31 ± 0.01
Average ϵ_{Trig}			1.30 ± 0.01

Table 5.4: Table of the 'trigger efficiency' –the probability that a $\Lambda_b^0 \to \Lambda_c^+\pi^-$ or $\bar{B}^0 \to D^+\pi^-$ candidate passes the Two Track Trigger selection criteria.

run	$\bar{B}^0(\%)$	$\Lambda_b(\%)$	$\bar{B}^0/\Lambda_b$
142110	49.2 ± 0.4	51.1 ± 0.5	0.96 ± 0.01
151477	51.5 ± 0.4	53.2 ± 0.5	0.97 ± 0.01
153661	50.1 ± 0.3	52.2 ± 0.5	0.96 ± 0.01
Average ϵ_{Reco}			0.96 ± 0.01

Table 5.5: Table of the 'offline reconstruction efficiency' – the probability that all four tracks from the $\Lambda_b^0 \to \Lambda_c^+\pi^-$ or $\bar{B}^0 \to D^+\pi^-$ candidate decay are reconstructed, given that this event has already satisfied the Two Track Trigger.

	$\bar{B}^0(\%)$	$\Lambda_b(\%)$	$\bar{B}^0/\Lambda_b$
ϵ_{ana}	42.2 ± 0.3	43.9 ± 0.3	0.96 ± 0.01

Table 5.6: Table of 'analysis efficiency' – the probability that the $\Lambda_b^0 \to \Lambda_c^+\pi^-$ or $\bar{B}^0 \to D^+\pi^-$ candidate passes all analysis cuts, given that it passed both the Two Track Trigger cut and that all four ultimate daughters are reconstructed as offline tracks.

	$\bar{B}^0(\%)/\Lambda_b(\%)$
$\epsilon_{Trigger}$	1.30 ± 0.01
ϵ_{Reco}	0.96 ± 0.01
ϵ_{Ana}	0.96 ± 0.01
ϵ_{tot}	1.20 ± 0.02

Table 5.7: Summary of efficiency ratios.

Chapter 6

Systematic Uncertainty

At this point we have all the needed parameters to calculate the relative branching ratio. Before doing that, we will estimate the systematic uncertainty introduced in this measurement. From Eq. (5.2), three terms are used to calculate the final result. The efficiency ratio $\epsilon_{\bar{B}^0}/\epsilon_{\Lambda_b}$ is from the "realistic" Monte Carlo sample. There will be systematic uncertainties when the real data and Monte Carlo simulation are not exactly the same. The event number ratio $N_{\Lambda_b}/N_{\bar{B}^0}$ is determined from fitting the data, the systematic uncertainty arises from the fit models. The ratio of branching ratios, $BR(D^+ \to K\pi\pi)/BR(\Lambda_c^+ \to pK\pi)$, is obtained from PDG and comes from the results of other experiments. There is some uncertainty associated with those results. The following sections will discuss all the known possible sources of systematic uncertainties.

6.1 Uncertainties From Monte Carlo

The measurement of the ratio of efficiencies avoids many systematic errors from absolute tracking and trigger efficiencies which affect $\epsilon_{\bar{B}^0}$ and ϵ_{Λ_b} the same way. However, any errors that affect the two efficiencies differently will introduce some systematic uncertainties.

6.1.1 Uncertainties due to Λ_b and $\bar{B}^0$ lifetimes

When the Monte Carlo simulation sample is made, some parameters like lifetime have to be fed into the simulation program. The world average values are usually used as input. There are uncertainties associated with those values. For instance, the $\bar{B}^0$'s lifetime from 2002 PDG is $c\tau = 462 \pm 5\ \mu m$, the Λ_b^0 's lifetime is $c\tau = 369 \pm 5\ \mu m$. Because we have made selection cuts on the lifetime, the uncertainties of the input lifetime could introduce systematic errors. To estimate this effect, the input lifetime values are modified by one sigma up and down from the central values. The Monte Carlo sample is regenerated using these new values and the percent changes of the efficiency ratio is taken as the systematic errors.

- $\bar{B}^0$ lifetime. The central value is $c\tau = 462\mu$m. We move it up to 467μm and down to 457μm, which causes negligible ($< 0.2\%$) change on the efficiency ratio.

- Λ_b lifetime. The central value used is $c\tau = 369\mu$m. We move it up to 393μm and down to 345μm. These shifts result in changes to the efficiency ratio of -4% and $+5\%$, respectively.

6.1.2 Dalitz structure of Λ_c

The 'Dalitz structure' here refers to the resonant substructure in the $\Lambda_c^+ \to p^+K^-\pi^+$ decay. The three resonance decays are listed in the following as well as a nonresonance decay.

$$\begin{aligned}
\Lambda_c^+ &\to p\ \ \overline{K^*}^0, \\
&\qquad \overline{K^*}^0 \to K^-\pi^+ \\
\Lambda_c^+ &\to \Lambda(1520)\ \ \pi^+, \\
&\qquad \Lambda(1520) \to p\ \ K^- \\
\Lambda_c^+ &\to \Delta^{++}\ K^-, \\
&\qquad \Delta^{++} \to p\,\pi^+ \\
\Lambda_c^+ &\to p\ \ K^-\ \ \pi^+
\end{aligned}$$

The presence of a resonant state decaying into two of the three Λ_c^+'s daughters does not help in the Λ_c^+'s reconstruction. However, the resonances may significantly alter some parameter distributions of the three final daughters, e.g. the p_T distribution and the angular orientation can be especially altered because of the spin of some of the resonances. Therefore, the trigger efficiency may be different for different resonance states. The QQ package used to simulate the Λ_c^+ decay does not properly take these resonance decays into account. Therefore, three independent Monte Carlo samples are generated with the Λ_c^+ in each sample forced to decay into one specific resonance. The corresponding efficiency ϵ_{Λ_b} is measured for each state. The changes in ϵ_{Λ_b} between the three resonant decay modes and our nonresonant decay mode are listed in Table 6.1. The branching fraction of each resonance decay measured by the E791 experiment [68] is also shown in Table 6.1.

Decay mode	BR	Change on ϵ_{Λ_b}
$pK^*(890)$	0.195	$+5\%$
$\Delta(1232)K$	0.180	-7%
$\Lambda(1520)\pi$	0.077	~ 0
Nonresonant	0.548	0 (QQ default)

Table 6.1: The main resonance states among decay modes of Λ_c^+ .

The changes of ϵ_{Λ_b} on each resonance mode represent the most extreme case where all Λ_c^+s decay into that mode. We weight the changes by the branching fractions given above, then smear the result by 20% to allow for the possible interference between different modes. This procedure gives a 1% change in the efficiency ratio.

As a cross-check, the Dalitz plot from $\Lambda_b^0 \to \Lambda_c^+\pi^-$ candidates in the data is shown in Fig. 6.1. The plot is not sideband subtracted. Although the number of Λ_b^0 events is very limited, we can still see that the distribution is not flat which indicates the existence of resonances.

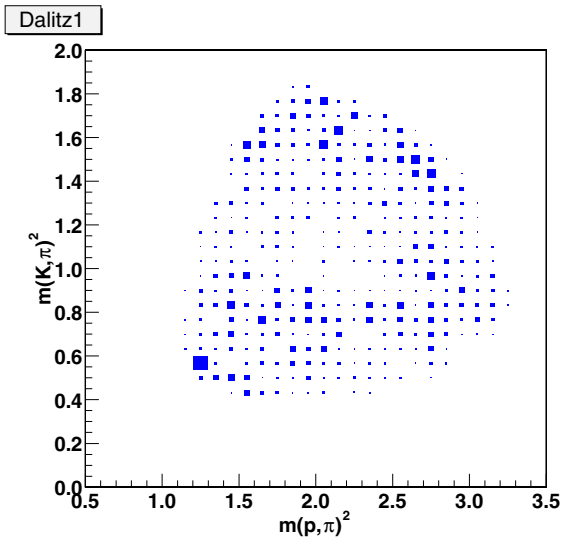

Figure 6.1: Dalitz plot from data without sideband subtraction.

6.1.3 Polarization of Λ_b^0, Λ_c^+

The Bgenerator and QQ programs do not include any provision for the polarization of Λ_b^0 and Λ_c^+ . Therefore, the non-null true value of polarization needs to be taken into account, and a systematic error needs to be calculated.

In hadron-hadron interactions the Λ_b^0 polarization in the Λ_b^0 rest frame can only be along "n", the normal to the "production plane", shown in Fig 6.2. This plane is defined by the momenta of the b quark before fragmentation and the hadron afterward [69], [70]. The angular distribution of the Λ_b^0 decay is weighted as:

$$I(\Theta) \propto 1 + P_{\Lambda_b}\alpha_{\Lambda_b}\cos(\Theta),$$

where α is a decay parameter, and Θ is the angle between the Λ_c^+ and the Λ_b^0 's production plane. The distribution of the emission angle of the proton can be written like

$$I(\theta) \propto 1 + \alpha_{\Lambda_b}\alpha_{\Lambda_c}\cos(\theta).$$

Here, both α_{Λ_b} and α_{Λ_c} are decay parameters. The θ is defined as in Fig 6.3 in the Λ_c^+ 's center of mass frame. Fig 6.4 combines the two previous figures to show both polarization angles (Θ, θ) and the Λ_b^0 production plane.

To establish the systematic error related to the Λ_b^0 and Λ_c^+ polarization the Monte Carlo events are reweighted by the angular distribution when $P_{\Lambda_b}\alpha_{\Lambda_b}$ and $\alpha_{\Lambda_b}\alpha_{\Lambda_c}$ are set to 1, -1 and 0. All possible combinations of the parameters are tried and yield no more than a 7% change in the efficiency ratio.

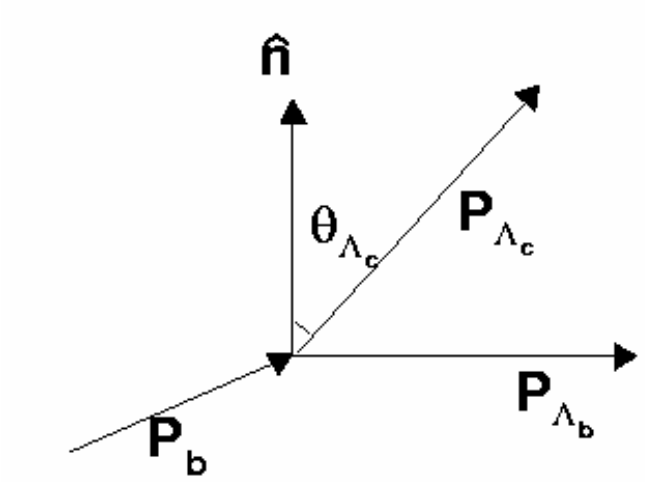

Figure 6.2: Λ_b decay angle definition for production polarization

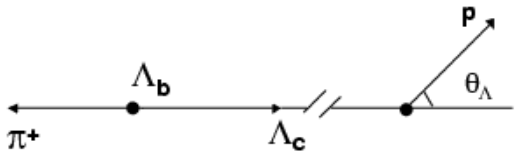

Figure 6.3: Λ_c polarization in term of emission angle of proton

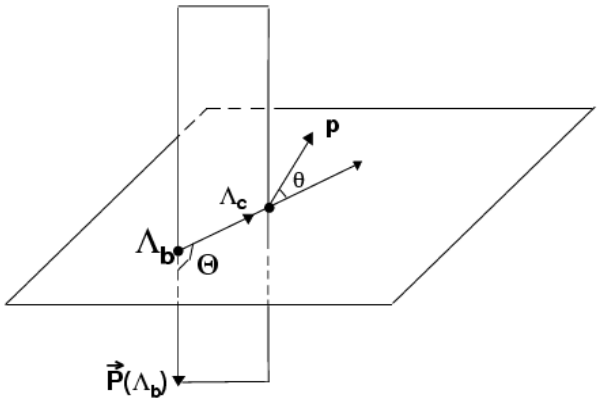

Figure 6.4: The system for testing Λ_b polarization

6.1.4 XFT configuration

XFT tracks are used in both the Level-1 and Level-2 trigger systems. XFT uses the hits from the COT axial (r-ϕ) superlayers to build XFT tracks. For each superlayer a certain number of found hits is required to build a track segment. Before run 152636, the number of required hits was 10 (out of total 12). After that, it was changed to 11. These two different XFT configurations are conventionally referred to as "XFT 2-miss" and "XFT 1-miss", respectively. The efficiency ratio $\epsilon_{\bar{B}^0}/\epsilon_{\Lambda_b}$ may vary under these two configurations. The central value of the efficiency ratio is determined from the Monte Carlo sample which only used the "XFT 2-miss" configuration. Another sample using the "XFT 1-miss" configuration is generated and the efficiency ratio is calculated. A +3% change in efficiency is observed and quoted as the systematic error from the XFT configuration.

6.1.5 ϕ efficiency

The Monte Carlo sample used in this analysis is produced by a version of the simulation package which contains a small error in the silicon geometry. Namely, the volumes of two of the Silicon Layer 0 ladders mistakenly overlap with passive material and are for this reason not simulated by GEANT. The result is a lack of silicon hits in these volumes of the two ladders. This affects both the SVT and the offline tracking efficiency. The effect is shown in Fig 6.5 where the ϕ_0 distribution of one pion candidate track (the one from Λ_b^0) is plotted. The distribution is not flat due to the two affected ladders. The problem was not fixed until some time after this analysis was done. A systematic error is thus introduced in this analysis to address the possible bias. We calculate the efficiency ratio by excluding the low efficiency phi region and find a +3% change of the efficiency ratio.

6.1.6 p_T spectrum of $\bar{B}^0$

A specific b-quark p_T spectrum is used to generate B hadrons in Bgenerator. The output $\bar{B}^0$ mesons' p_T spectrum in the Monte Carlo is compared with data. The

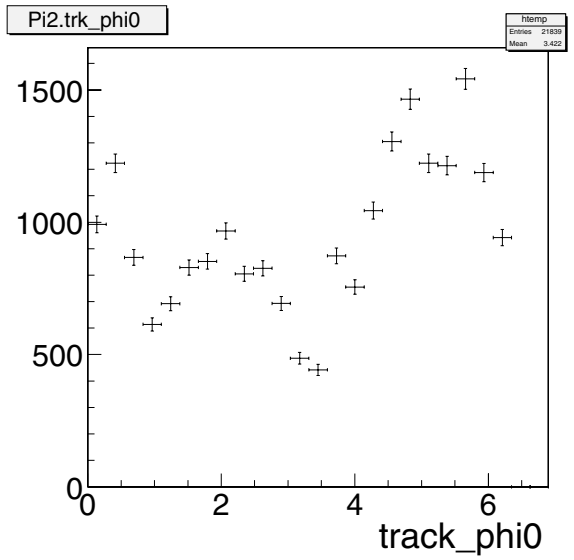

Figure 6.5: The ϕ_0 distribution of one pion candidate track. The pion here is the one from Λ_b^0 .

comparison is shown in Fig. 6.6. There are some discrepancies between the Monte Carlo results and the data in the lower p_T region. In order to calculate the effect of this discrepancy the Monte Carlo sample is reweighted to make its p_T distribution agree with the data. The efficiency ratio $\epsilon_{\bar{B}^0}/\epsilon_{\Lambda_b}$ is recalculated using the reweighted sample. The dependence of the efficiency ratio on $p_T(\bar{B}^0)$ before and after the reweighting is given in Fig. 6.7. The figure shows that the systematic uncertainty caused by the p_T spectrum of $\bar{B}^0$ is small, i.e., the efficiency ratio changes by only $+1\%$ after this reweighting.

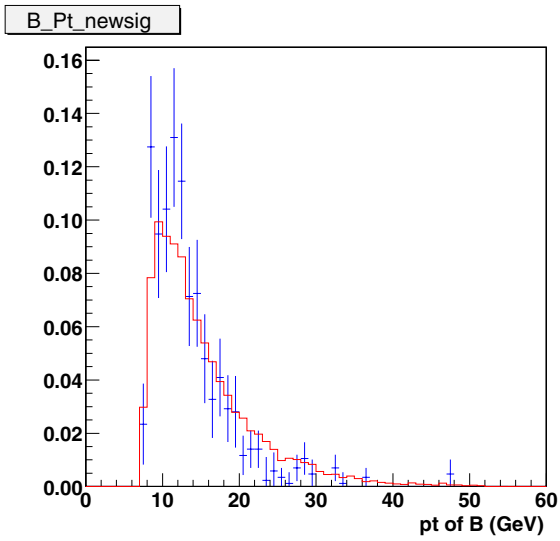

Figure 6.6: A comparison of p_T of the $\bar{B}^0$ candidates in the data and the realistic Monte Carlo. The red solid histogram is MC and green points are data.

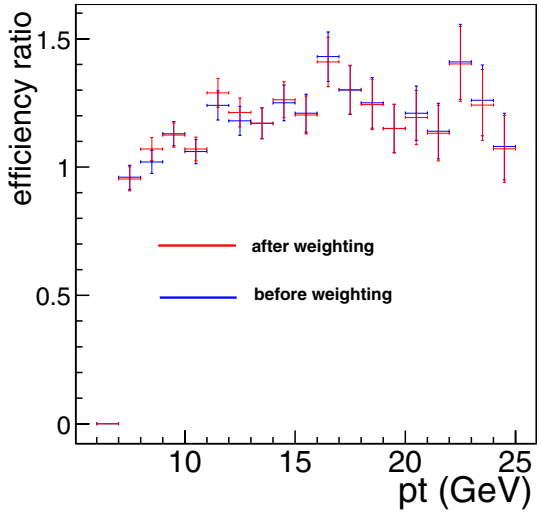

Figure 6.7: Efficiency ratio *vs.* p_T of B^0.

6.2 Uncertainties From Fit Models

Further systematic uncertainties arise from both the $\bar{B}^0$ and Λ_b^0 fitting due to the limitations of the fit models. For $\bar{B}^0$, two different shapes are used to model the background as shown in Section 5.2.2, Table 5.1. A 6% difference (20 events) is found for the yield of $\bar{B}^0$ due to the uncertainty of the fit model. In Section 5.4.5 different parameters in the Λ_b^0 fitter are used to refit the data. The effects of varying the parameters are shown in Table 5.3. The total change of 13% (8 events) in the Λ_b^0 yield is quoted as systematic uncertainty.

6.3 Uncertainties From Errors in Branching Ratios $D^+ \to K^-\pi^+\pi^+$ and $\Lambda_c^+ \to p^-K^+\pi^-$

When calculating the relative branching ratio using Eq. 5.2, we quoted two branching ratios from the 2002 PDG.

$$BR(D^+ \to K^-\pi^+\pi^+) \;=\; 9.1 \;\pm\; 0.6\ \%$$

$$BR(\Lambda_c^+ \to p^+K\pi^+) \;=\; 5.0 \;\pm 1.3\ \%$$

The ratio of the two branching ratio is 1.82 ± 0.49. We can see that the measurement of the Λ_c^+ branching ratio has a large error with it, which gives a large systematic error (27%) in our final result. Since this error is not controlled by this analysis we will put it in a separate term.

6.4 Summary

A summary of the systematic errors is shown below in the Table 6.2. The total uncertainty caused by using a Monte Carlo to determine $\epsilon_{\bar{B}^0}/\epsilon_{\Lambda_b}$ is about 9%. The uncertainty from the fit model is 6% for $\bar{B}^0$ and 13% for Λ_b^0 , respectively. The largest uncertainty, 27%, is from the branching ratios we quote from PDG.

	central value	variation range	(%) change
$\bar{B}^0$ lifetime (μm)	462	457-467	$\pm$ 0
Λ_b lifetime (μm)	369	345-393	+4-5
Λ_c Dalitz structure	Nonresonant		+1
Pt spectrum			+1
Λ_b polarization	0	$\pm$1	$\pm$7
XFT	2-miss	1-miss	+3
ϕ efficiency			+3
subtotal			$\pm$9
Fit model($\bar{B}^0$)			$\pm$6
Fit model(Λ_b)			$\pm$13
$BR(\Lambda_c \to pk\pi)/BR(D^+ \to K\pi\pi)$	0	$\pm$27%	$\pm$ 27

Table 6.2: A summary of the sources of the systematic uncertainty.

Chapter 7

Results and Conclusions

7.1 Experimental Result

Once again, the formula we use to measure the Λ_b^0 branching ratio is Eq. (5.2):

$$\frac{f_{\Lambda_b}}{f_d}\frac{BR(\Lambda_b \to \Lambda_c^+\pi^-)}{BR(\bar{B}^0 \to D^+\pi^-)} = \frac{BR(D^+ \to K\pi\pi)}{BR(\Lambda_c^+ \to pK\pi)}\frac{N_{\Lambda_b}}{N_{\bar{B}^0}}\frac{\epsilon_{\bar{B}^0}}{\epsilon_{\Lambda_b}}.$$

We have obtained the number of $\bar{B}^0$ and Λ_b^0 events with their statistic and systematic uncertainties from fitting the invariant mass distributions in the data. Those values are:

$$N_{\Lambda_b} = 96 \pm 13(stat.) \pm 8(syst.) \tag{7.1}$$

$$N_{\bar{B}^0} = 321 \pm 22(stat.) \pm 20(syst.) \tag{7.2}$$

$$\frac{N_{\Lambda_b}}{N_{\bar{B}^0}} = 0.30 \pm 0.05(stat.) \pm 0.03(syst.). \tag{7.3}$$

We have determined the efficiency ratio of two decay modes and its systematic uncertainty from the Monte Carlo sample:

$$\frac{\epsilon_{\bar{B}^0}}{\epsilon_{\Lambda_b}} = 1.20 \pm 0.02(stat.) \pm 0.11(syst.). \tag{7.4}$$

We use the 2002 Particle Data Group world average for the following ratio of two branching fractions:

$$\frac{BR(D^+ \to K\pi\pi)}{BR(\Lambda_c^+ \to pK\pi)} = 1.82 \pm 0.49. \tag{7.5}$$

Putting together Eqs. (7.3), (7.4) and (7.5), we obtain

$$\frac{f_{\Lambda_b}}{f_d}\frac{BR(\Lambda_b \to \Lambda_c^+\pi^-)}{BR(\bar{B}^0 \to D^+\pi^-)} = 0.66 \pm 0.11\ (\text{stat.}) \pm 0.09\ (\text{syst.}) \pm 0.18\ (\text{BR}). \quad (7.6)$$

The last term is the uncertainty from Eq. (7.5). To extract the relative branching ratio, the 2002 Particle Data Group fragmentation ratio

$$\frac{f_{baryon}}{f_d} = 0.304 \pm 0.053 \quad (7.7)$$

is used. Because other b-baryons are produced much less frequently than Λ_b^0 , here we assume f_{baryon} is equal to f_{Λ_b}. So we get:

$$\frac{BR(\Lambda_b \to \Lambda_c^+\pi^-)}{BR(\bar{B}^0 \to D^+\pi^-)} = 2.2 \pm 0.4\ (\text{stat.}) \pm 0.3\ (\text{syst.}) \pm 0.7\ (\text{BR+FR}). \quad (7.8)$$

The last term is the uncertainty from Eqs. 7.5 and 7.7. Finally, the 2002 Particle Data Group branching ratio of $\bar{B}^0 \to D^+\pi^-$

$$BR(\bar{B}^0 \to D^+\pi^-) = (3.0 \pm 0.4) \times 10^{-3} \quad (7.9)$$

is used and we get a branching ratio of $\Lambda_b^0 \to \Lambda_c^+\pi^-$:

$$BR(\Lambda_b^0 \to \Lambda_c^+\pi^-) = \{6.6 \pm 1.2\ (\text{stat.}) \pm 0.9\ (\text{syst.}) \pm 2.3\ (\text{BR+FR})\} \times 10^{-3}. \quad (7.10)$$

7.2 Discussion and Conclusion

In this thesis, we have searched for the decay $\Lambda_b^0 \to \Lambda_c^+\pi^-$ in ~ 65 pb^{-1} of CDF's Two-Track Hadronic Trigger data sample. We have reconstructed 96 ± 13 Λ_b^0 events, making this the largest sample of fully reconstructed Λ_b's in existence, and the first such signature observed in CDF. We furthermore use this signal to measure $BR(\Lambda_b^0 \to \Lambda_c^+\pi^-)$. The result is shown in Eq. 7.10. This is the world's first branching ratio measurement of this decay mode.

Our result is consistent with the theoretical predictions in Section 2.4 within experimental errors. The dominant uncertainty in this measurement comes from the $\Lambda_c^+ \to p^+K\pi^+$ branching ratio. With a more precise measurement of $\Lambda_c^+ \to p^+K\pi^+$

branching ratio in the future, our result could be used to put more constraints on theoretical models.

With more CDF Run II data coming out, the fully reconstructed $\Lambda_b^0 \to \Lambda_c^+ \pi^-$ sample can be used to measure the Λ_b^0 's lifetime and polarization. The reconstruction methods used in this analysis could also be used to search for other rarely produced bottom baryons. This analysis just opens a door to the exciting bottom baryon world.

Appendix A

The cut optimization

The cut optimization is to find the best cut values to select our signal and reject the background. We use the Monte Carlo sample to simulate the behavior of the signal decay, $\Lambda_b^0 \to \Lambda_c^+ \pi^-$. The data sidebands, the events that reside in the region away from the Λ_b^0 peak, are used to describe the behavior of the background. The signal significance is calculated using the formula defined as

$$Significance = \frac{S}{\sqrt{S+B}}. \tag{A.1}$$

Here, S is the number of signal events after certain cuts, B is the number of the background events under the signal peak after the same cuts. A "multi-dimensional" scan on different selection cut values is performed. In this scan process, each cut variable changes its cut value by a fixed step every time. The significances of all combinations of the cut values are calculated. The cut values that make the significance maximum are obtained. The "N-1"[1] scans of significance are provided in the following plots together with the reconstruction efficiency.

[1] "N-1" scan means all cut values are fixed using the best ones obtained from the multi-dimensional scan except the one that is going to be scanned and plotted.

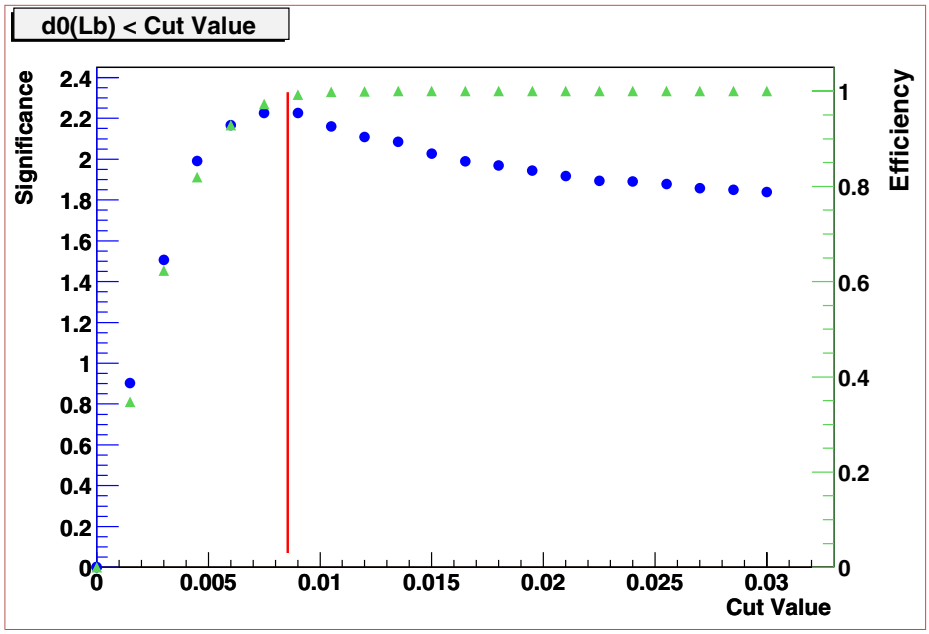

Figure A.1: Significance as a function of d_0 of Λ_b. Blue dots mark the significance and green triangles the reconstruction efficiency.

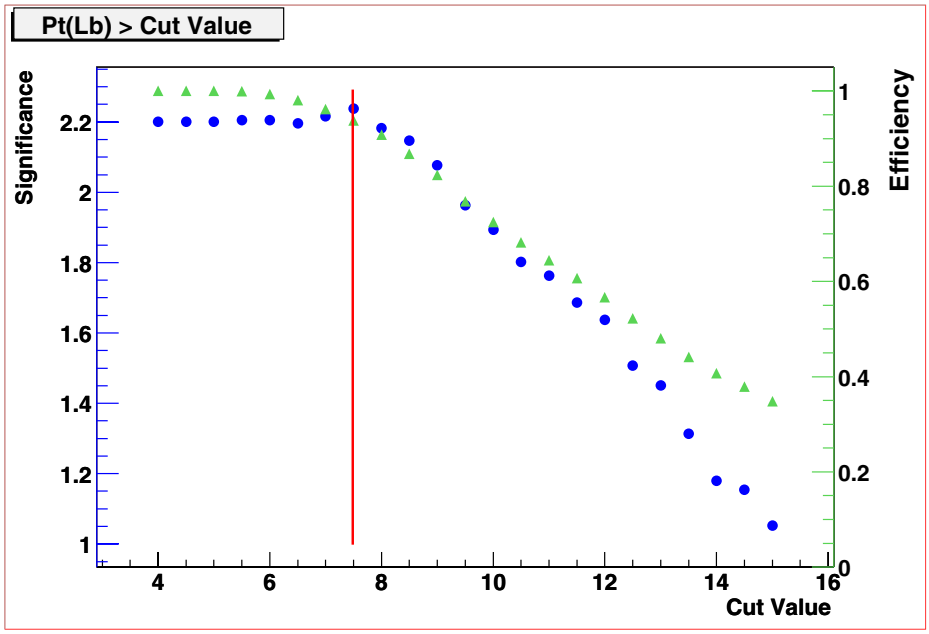

Figure A.2: Significance as a function of p_T of Λ_b. Blue dots mark the significance and green triangles the reconstruction efficiency.

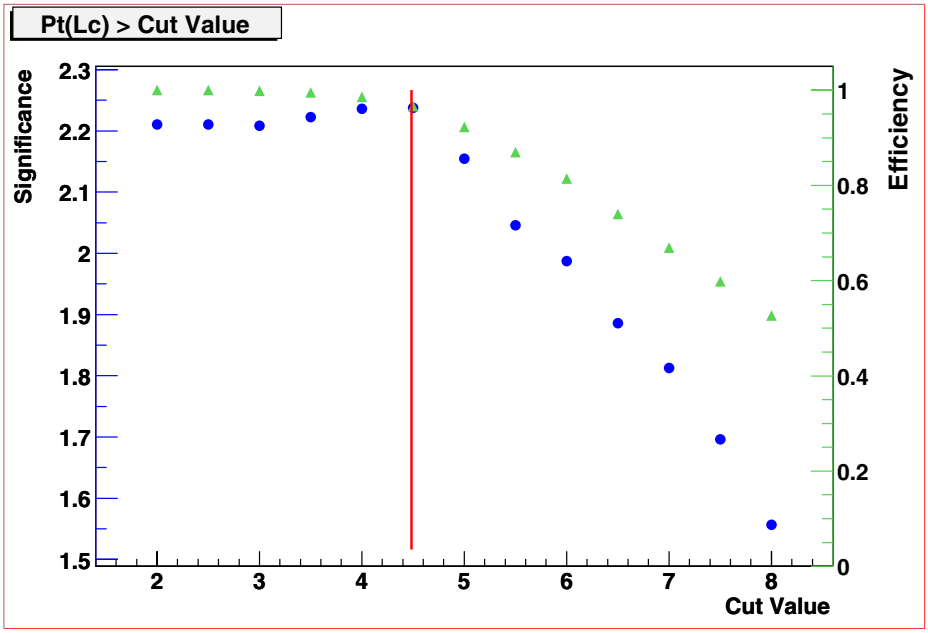

Figure A.3: Significance as a function of p_T of Λ_c. Blue dots mark the significance and green triangles the reconstruction efficiency.

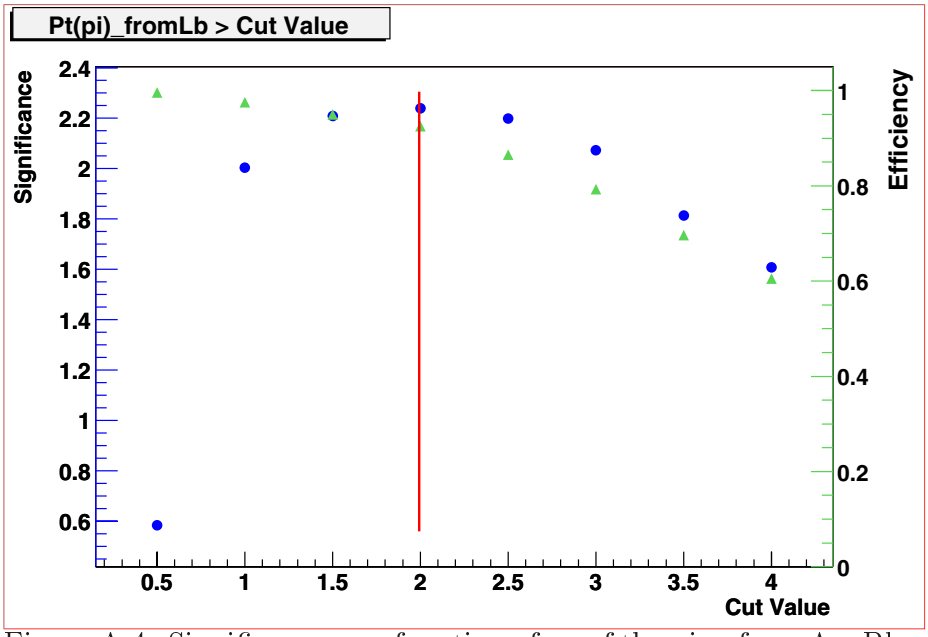

Figure A.4: Significance as a function of p_T of the pion from Λ_b. Blue dots mark the significance and green triangles the reconstruction efficiency.

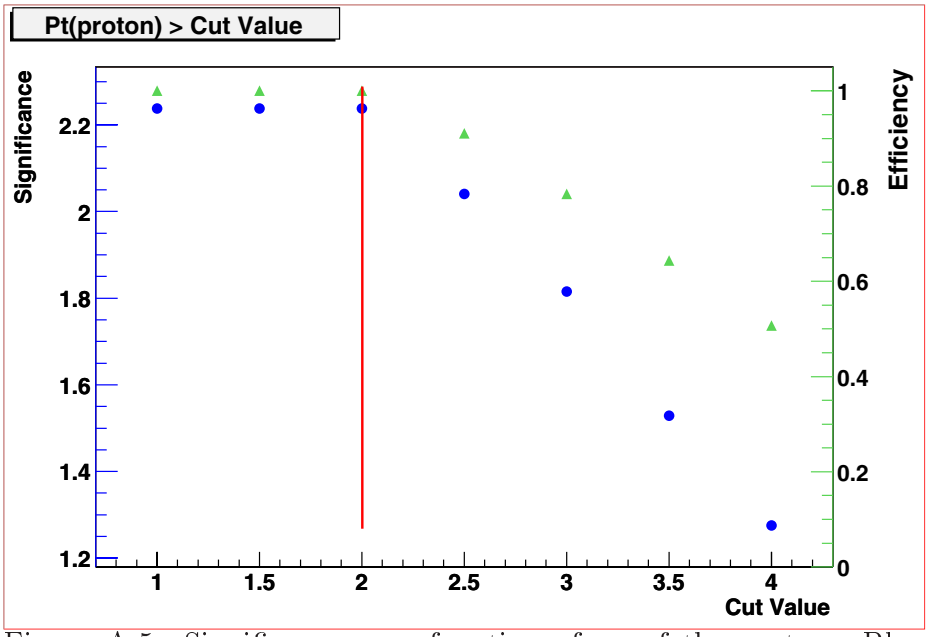

Figure A.5: Significance as a function of p_T of the proton. Blue dots mark the significance and green triangles the reconstruction efficiency.

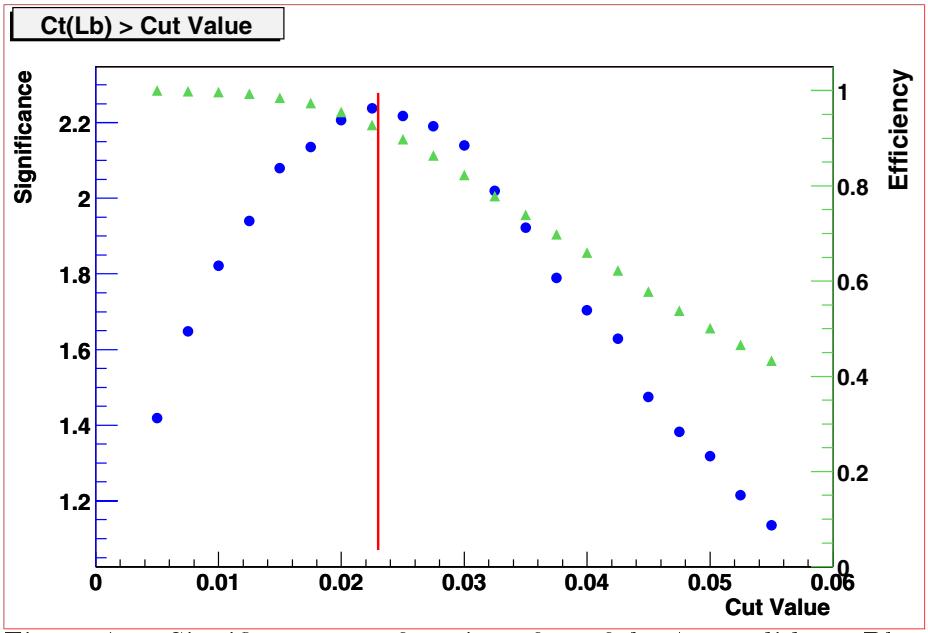

Figure A.6: Significance as a function of $c\tau$ of the Λ_b candidate. Blue dots mark the significance and green triangles the reconstruction efficiency.

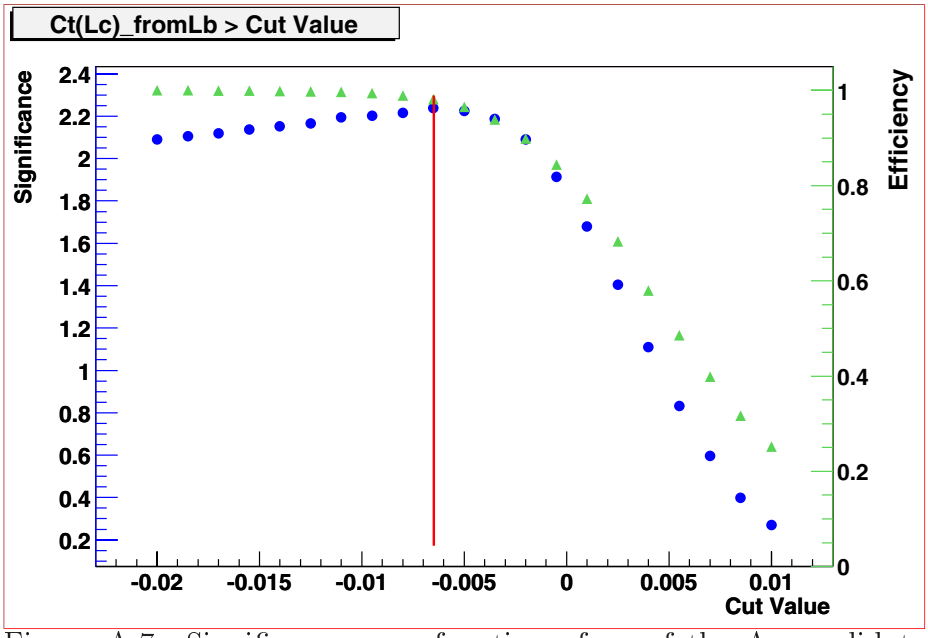

Figure A.7: Significance as a function of $c\tau$ of the Λ_c candidate measured from the Λ_b vertex. Blue dots mark the significance and green triangles the reconstruction efficiency.

Appendix B

The effect of the Λ_b^0 selection cuts

In the following plots we show the distributions of the quantities that we used to make Λ_b^0 selection cuts. Those distributions are from the "realistic" Monte Carlo simulation. The cut values determined from the optimization procedure in Appendix A are also shown in the plots.

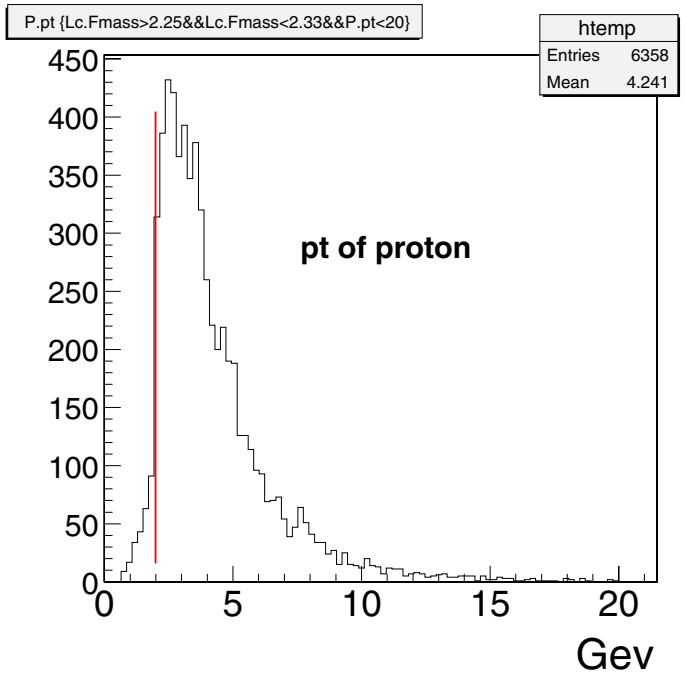

Figure B.1: p_T of the proton in the realistic Monte Carlo simulation. The cut is at $p_T = 2.0$ GeV/c

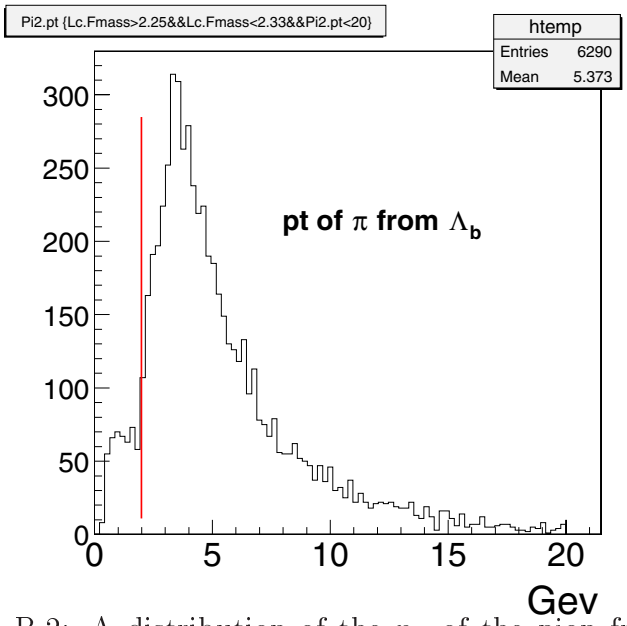

Figure B.2: A distribution of the p_T of the pion from Λ_b decay in the realistic Monte Carlo simulation. The cut is at $p_T = 2.0$ GeV/c.

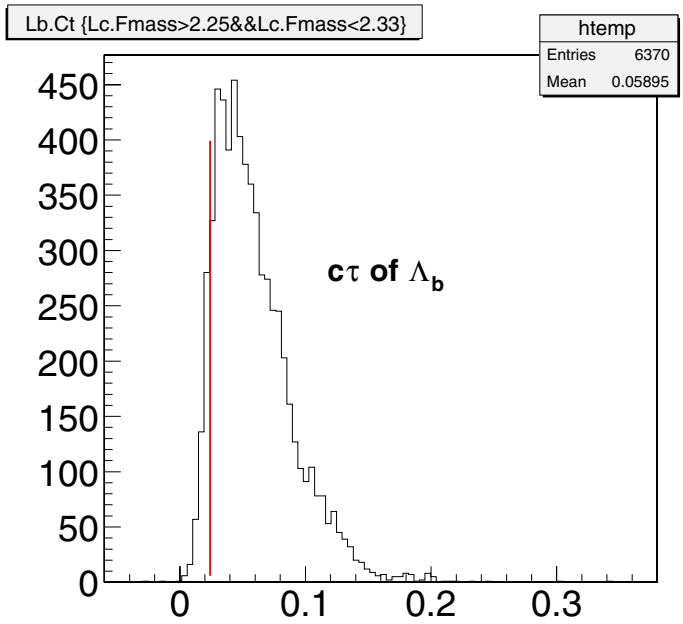

Figure B.3: Distribution of $c\tau$ for the Λ_b^0 in the realistic Monte Carlo simulation. The cut is at $c\tau = 0.0225$ cm.

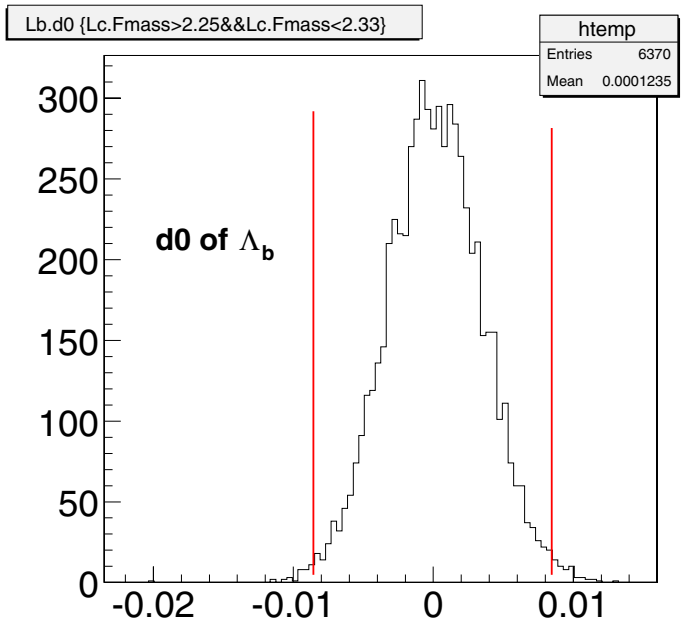

Figure B.4: The impact parameter d_0 for the Λ_b^0. The cut is at $|d_0| = 0.0085$ cm.

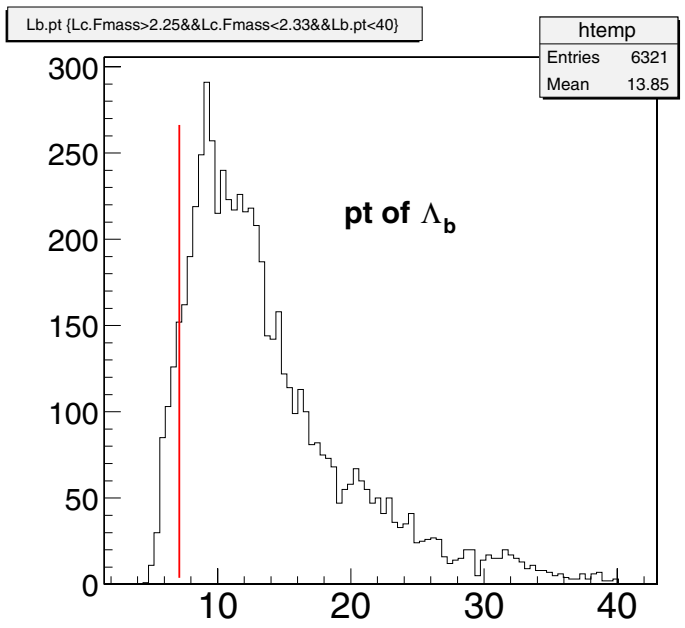

Figure B.5: The p_T of Λ_b^0. The cut is at $p_T = 7.5$ GeV/c.

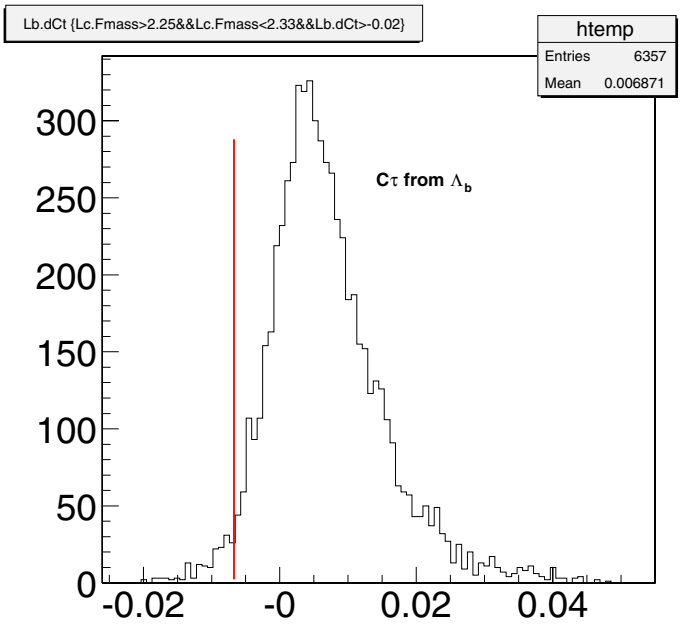

Figure B.6: The $c\tau$ of the Λ_c^+ measured from the Λ_b^0 vertex. The cut is at $c\tau$ = -0.0065 cm.

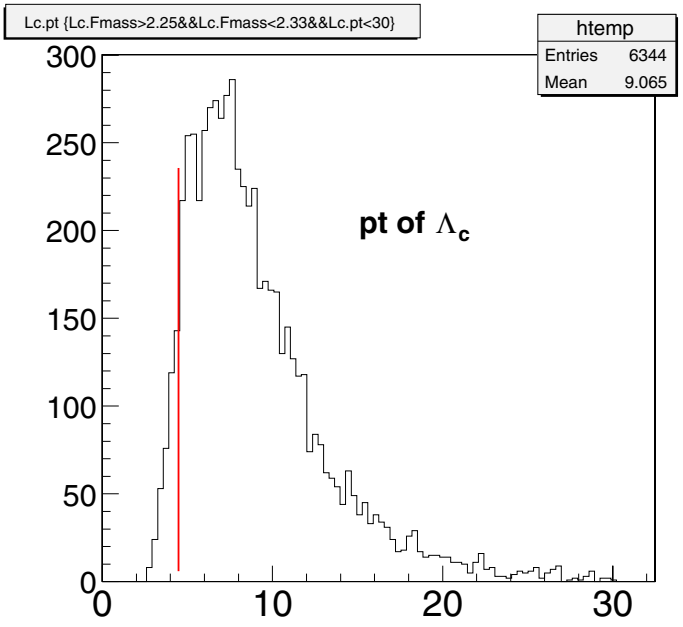

Figure B.7: The p_T of Λ_c^+. The cut is at p_T = 4.5 GeV/c.

Appendix C

The constraints in the Λ_b fit

C.1 Constraint on the number of the four-prong reflections

We want to put a constraint on the number of the four-prong reflections, $N_{\rm ref}$. We know the main contribution to $N_{\rm ref}$ is from decay $\bar{B}^0 \to D^+\pi^-$. We did an explicit search for $\bar{B}^0 \to D^+\pi^-$ in the $\Lambda_b \to \Lambda_c^+\pi^-$ invariant mass window [5.2 GeV/c^2, 5.8 GeV/c^2] and reconstructed 40 ± 12 B^0 candidates. The outcome of this search, along with the fit to the signal Gaussian on top of a linear background, is shown in Fig. C.1. On the other hand from the parametric Monte Carlo sample we obtained this decay mode represents 49% of the total four prong decays. Thus, we divide 40 ± 12 by 0.49 and obtain the constraint

$$N_{\rm ref} = 81.6 \pm 24.5 \tag{C.1}$$

C.2 Constraint on $N_{\rm ref}/N_{\rm otherB}$

The relative contribution of the four-prong reflections, $N_{\rm ref}$, *vs.* reflections from all other B meson decays, $N_{\rm otherB}$, needs to be preserved. The main decay channels in the four-prong decays, most notably $\bar{B}^0 \to D^+\pi^-$, have relatively well-known branching

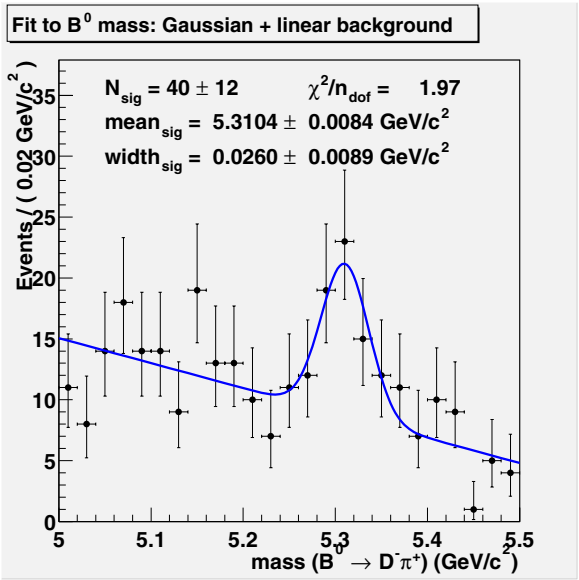

Figure C.1: $\bar{B}^0$ reflections explicitly reconstructed in Λ_b^0 's mass window. The result of this fit (40 ± 12 events) provides a normalization for the shape for all the four-prong reflections obtained from the Monte Carlo simulation (shown in Fig. 5.8).

ratios as reported by the BaBar and BELLE experiments. This constraint relies on determining the sum of the branching ratios of all the decay channels contributing to the four-prong component. Here we are guided by $BR(\bar{B}^0 \to D^+\pi^-) = (3.0 \pm 0.4) \times 10^{-3}$ as quoted in PDF 2002. Using the parametric Monte Carlo with the default QQ table, for $m(\Lambda_b) > 4.6$ GeV/c^2, as used in Chapter 5, we obtain

$$N_{\rm ref}/N_{\rm otherB} = 0.0558. \tag{C.1}$$

What remains to be determined is the error on this number. The above measurement of $BR(\bar{B}^0 \to D^+\pi^-)$ has a 13% relative error. Given that $B^0 \to D^+\pi^-$ comprises half of the four-prong reflections, and that the other half is less well-known, we double the error on the ratio (C.1) to 26%, and obtain the second constraint:

$$\frac{N_{\rm ref}}{N_{\rm otherB}} = 5.6 \pm 1.5\%. \tag{C.2}$$

C.3 Constraint on $N_{\mathrm{other}\Lambda_b}/N_{\mathrm{Bmesons}}$

The "other Λ_b" component in our fit is directly proportional to f_{baryon}. Since that quantity is known with a relative error of about 20%, we cannot leave the "other Λ_b" completely unconstrained. Here we develop the constraints on the normalization for the "other Λ_b" component, $N_{\mathrm{other}\Lambda_b}$, relative to the normalization of all other B meson states, $N_{\mathrm{ref}} + N_{\mathrm{otherB}}$.

If we used the perfect fragmentation fractions in our parametric Monte Carlo simulation, we could merely constrain $N_{\mathrm{other}\Lambda_b}/(N_{\mathrm{ref}} + N_{\mathrm{otherB}})$ to the ratio of events in the mass region of interest, $m_{\Lambda_b} > 4.6$ GeV/c^2. Each yield would include the total acceptance for each of the decay modes. The overall normalization of the total number of Monte Carlo events would cancel in the ratio. In the Monte Carlo simulation we have $N_{\mathrm{other}\Lambda_b} = 2174$ and $N_{\mathrm{ref}} + N_{\mathrm{otherB}} = 4751$. So in our parametric Monte Carlo, the ratio of observed baryons to observed mesons is 45.8%.

However, the fragmentation fractions are not known perfectly, and, moreover, our parametric simulation used the following obsolete values

$$B_u : B_d : B_s : \Lambda_b = 40.63 : 40.63 : 11.17 : 7.57\ \%$$

giving $f_{\mathrm{baryon}}/f_{\mathrm{meson}} = 8.2\%$. The fragmentation fractions in 2002 PDG are

$$B_u : B_d : B_s : \Lambda_b = 38.8 \pm 1.3 : 38.8 \pm 1.3 : 10.6 \pm 1.3 : 11.8 \pm 2.0\ \%$$

which yields $f_{\mathrm{baryon}}/f_{\mathrm{meson}} = 13.4 \pm 2.0\%$. Therefore, we need to scale the "other Λ_b" component up by $13.4/8.2 = 1.63$, as compared to the other two B meson components. We need to multiply 45.8% by 1.63 and obtain 74.7%.

In order to assign an error to this constraint, we note that its uncertainty is dominated by $f_{\mathrm{baryon}} = 11.8 \pm 2.0\%$. So it is reasonable to assume a relative error of $2.0/11.8 = 16.9\%$ on the constraint of 74.7%, *i.e.*, 12.6%.

However, the measurement of f_{baryon} is based on comparing the semileptonic decays of Λ_b to the semileptonic decays of the other three B meson species. The fact that the lifetime of Λ_b is shorter to the lifetimes of B mesons already offers evidence that the spectator model is not completely valid. We must allow for the fact that the

semileptonic width of baryons may be different from that of the mesons. In fact, we need to be conservative and inflate the error on f_{baryon}.

Accordingly, we increase this error by 100%, thereby weakening the third constraint to:

$$N_{\mathrm{other}\Lambda_{\mathrm{b}}}/(N_{\mathrm{ref}} + N_{\mathrm{otherB}}) = 74.7 \pm 25.2\%.$$

While we admit that the practice of inflating the error on f_{baryon} in this way is dubious at best, we hasten to add that the Λ_b yield is completely insensitive to this error, as shown in Section 5.4.5.

Bibliography

[1] For Reviews, see E. S. Abers and B. W. Lee, *Phys. Rev.* **9**:1, 1973; M. A. B. Beg and A.Sirlin, *Phys. Rep.* **88**:1, 1982.

[2] For Introduction, see '*Quarks and Leptons: An introduction course in Modern Particle Physics*', F. Halzen and A. D. Martin , Ed. John Wiley: New York 1984.

[3] H. Weyl, *Z. Phys.* **56**:330, 1929.

[4] C. N. Yang and R. Mills, *Phys. Rev.* **96**:191, 1954.

[5] D. Karlen, Talk at *ICHEP 98* , Vancouver, July 1998.

[6] W. Hollik, Talk at *International Workshop on Quantum Effects in the MSSM*, Barcelona, Sept 1997, hep-ph/9711492.

[7] S. W. Herb*et al.*, *Phys. Rev. Lett.* **39**:252,1977.

[8] G. Flugge, Proceedings of the 19th International Conference on High Energy Physics, Tokyo, 1978.

[9] CDF collaboration, F. Abe *et al.*, *Phys. Rev. Lett.* **69**:3704,1992.

[10] CDF collaboration, F. Abe *et al.*, *Phys. Rev. Lett.* **71**:500,1992.

[11] CDF collaboration, F. Abe *et al.*, *Phys. Rev. Lett.* **71**:2537,1993.

[12] P. Nason, S. Dawson and R. K. Ellis, *Nucl. Phys.* **B327**:49,1989 **B335**:260,1990.

[13] A. D. Martin, W. J. Stirling and R. G. Roberts, *Phys. Rev.* **D47**:867,1993.

[14] T. Sjostrand, *Int. J. Mod. Phys* **A3**:751,1988.

[15] B. R. Webber, *Int. J. Mod. Phys* **A15**:577,2000.

[16] C. Peterson, D. Schlatter, I. Schmittand, P. M. Aerwas, *Phys. Rev.* **D27**:105,1983.

[17] J. Chrin *Z. Phys.*. **C36**:163,1987.

[18] ALEPH, CDF, DELPHI, L3, OPAL, SLD collab. *CERN-EP/2001-050*, 2001

[19] J. Gasser and H. Leutwyler, *Phys. Rep.* **87**:77, 1982.

[20] M. Neubert, *Phys. Rep.* **245**:259, 194.

[21] T. Appelquist and H. D. Politzer, *Phys. Rev. Lett.* **34**:43, 1975.

[22] E. Eichten and B. Hill, *Phys. Letter.* **B234**:511,1990.

[23] H. Georgi, *Phys. Letter.* **B240**:447,1990.

[24] UA1 collaboration, C. Albarjar *et al.*, *Phys. Lett.* **B273**:540,1991.

[25] CDF collaboration, F. Abe *et al.*, *Phys. Rev.* **D47**:2639,1993.

[26] S. E. Tzmarias, *Proceedings of the 27th International Conference on High Energy Physics*, Glasgow, Scotland, 1994.

[27] CDF collaboration, F. Abe *et al.*, *Phys. Rev.* **D55**:1142,1997.

[28] CDF collaboration, F. Abe *et al.*, *Phys. Rev. Lett.* **77**:1439,1996.

[29] ALEPH collaboration, D. Buskulic *et al.*, *Phys. Lett.* **B357**:685,1995.

[30] DELPHI collaboration, P. Abreu *et al.*, *Z. Phys.* **C68**:375,1995.

[31] OPAL collaboration, R. Akers *et al.*, *Z. Phys.* **C69**:195,1996.

[32] ALEPH collaboration, D. Buskulic *et al.*, *Phys. Lett.* **B380**:437,1996.

[33] DELPHI collaboration, P. Abreu *et al.*, *Phys. Lett.* **B374**:351,1996.

[34] X.-H. Guo, *Mod. Phys. Lett.* **A13**:2265,1998.

[35] Jong-Phil Lee, Chun Liu and H. S. Song, *Phys. Rev.* **D58**:014013,1998.

[36] M. A. Ivanov, J. G. Korner, V. E. Lyubovitskij and A. G. Rusetsky, *Phys. Rev.* **D57**:5632,1998.

[37] J. Marriner, *Presented at International Workshop on Beam Cooling and Related Topics (COOL03)* May,2003.

[38] M. A. Martens, *presentation to the Accelerator Advisory Committee* Feb 04,2003.

[39] CDF collaboration, *The CDF II Detector Technical Design Report* Nov,1996.

[40] T.Afforlder *et al. CDF Central Outer Tracker* CDF Note 6267, 2003

[41] B. Ashmanskas *et al.*, *Proceedings 9th Pisa Meeting on Advanced Detectors*, La Biodola , Italy, 2003.

[42] B. Ashmanskas *et al.*, *Proceedings of the ICALEPCS 2001 Conference*, San Jose, CA, 2001.

[43] J. Antos, M. Babik*et al. The CDF Run 2 Offline Computer Farms* CDF Note 5702, 2001.

[44] J. Lewis, D. Saltzberg and M. Shochet *et al. CDF Run-II Trigger Table and Datasets Plan* CDF Note 4718, 1998.

[45] M. Paulini and B. Wicklund *et al. Summary of Proposals for B Physics Triggers in Run II* CDF Note 5483, 2000.

[46] A. Belloni, I. K. Furic and Ch. Paus *Multbody Trigger Paths in the Two Track Trigger Data* CDF Note 6526, 2003.

[47] http://cdfkits.fnal.gov/CdfCode/source/Level3Mods/

[48] http://www-cdf.fnal.gov/internal/physics/bottom/validation/

[49] W. Badgett *The CDF Run II Run Database and Online Java API* CDF Note 5672, 2001.

[50] P. Sphicas *A $b\bar{b}$ Monte Carlo Generator* CDF Note 2655, 1994.

[51] K. Anikeev, C. Paus and P. Murat *Description of Bgenerator II* CDF Note 5092, 1999.

[52] P. Nason, S. Dawson and R. K. Ellis *Nucl. Phys.* **B303**:607,1988; *Nucl. Phys.* **B327**:49,1988.

[53] W. Bell, F. Wurthkein *et al. User Guide for EvtGen at CDF* CDF Note 5618, 2003.

[54] http://cdfkits.fnal.gov/CdfCode/source/EvtGen/doc/guide.ps

[55] J. Lewis, P. Avery *CLEOMC: CDF interface to the CLEO Monte Carlo: QQ* CDF Note 2724, 1994.

[56] Application Software Group *GEANT Detector Description and Simulation Tool*, CERN Program Library Long Write-up W5013.

[57] R. Lachman and Ch. Paus *A Quick Simulation of Tracking using GEANT* CDF Note 6091, 2002.

[58] I. Furic and Ch. Paus *Track Trigger Simulation at the Generator Level in Run II* CDF Note 5348, 2000.

[59] J. Boudreau and R. Snider *A User's Guide to CdfTrack and Related Classes* CDF Note 5089, 2000.

[60] A. Mukherjee *CTC and VTX Tracking* CDF Note 5490, 2000.

[61] P. Azzi, G. Busetto *et al. Histogram Tracking in the COT* CDF Note 5562, 2001.

[62] W.-M. Yao and K. Bloom *"Outside-In Silicon Tracking at CDF"* CDF Note 5991, 2002.

[63] G. Bauer and A. Korn *et al. Update on Calibration of Energy Loss and Magnetic Field using J/ψ Events in Run II* CDF Note 6355, 2003.

[64] M. Feindt, S. Menzemer *et al. TrackingKal A Tracking and Alignment Software Package for CDF II Tacking Advantage of a Fast Kalman Track-Fitter* CDF Note 5387, 2000.

[65] http://cdfkits.fnal.gov/CdfCode/source/svtsim/

[66] D. Lucchesi, S. D. Ronco *et al Study of B_s yields in the hadronic trigger* CDF Note 6345, 2003.

[67] C. H. Wang BELLE Collaboration, hep-ex/0105022

[68] E. M. Aitala *Phys. Lett.* **B471**:449, 2000.

[69] P.Bialas *et al. Z.Phys.* **C57**:115, 1993.

[70] A.Fridman *et al.* **CERN-PPE-93-61** 1993.

[redacted]

He attended public elementary school and high school in the same city and graduated in 1992. He subsequently enrolled at University of Science and Technology of China (USTC) in Hefei, Anhui Province. He studied at Department of Modern Physics in the next six years and earned his Bachelor of Science degree in 1996 and Master of Science degree in 1998. During the years at USTC, he participated several R&D projects on various particle detectors. His Master thesis is about studying the properties of a new kind GaAs radiation detector. He was also a teaching assistant for undergraduate courses. In the fall of 1998, he went to the United States and began his Ph.D. program at the Johns Hopkins University in Baltimore, Maryland, studying under Prof. Bruce Barnett. He finished his required course studies in the first two years and also served as a teaching assistant for the introductory physics courses and labs at the same time. He moved to FermiLab, Illinois in June 2000 to conduct his thesis research as a member of the CDF collaboration. He was there since then until he got his Ph.D. degree.